

Magnetic Resonance Sounding with separated transmitter and receiver loops for the investigation of 2D water content distributions

vorgelegt von
Diplom-Geowissenschaftler (Angewandte Geophysik)
Marian Hertrich
aus Dernbach/WW

von der Fakultät VI Bauingenieurwesen und Angewandte Geowissenschaften
der Technischen Universität Berlin
zur Erlangung des akademischen Grades
Doktor der Naturwissenschaften
-Dr. rer. nat.-
genehmigte Dissertation

Promotionsausschuss:

Vorsitzender: Prof. U. Tröger

Berichter: Prof. U. Yaramanci

Berichter: Dr. Anatoly Legtchenko

Tag der wissenschaftlichen Aussprache: 6. April 2005

Berlin 2005
D83

Abstract

An extended mathematical formulation for the response signal of Magnetic Resonance Soundings (MRS) allows the treatment of individual transmitter and receiver loop. The present work extensively evaluates and assesses the potential and limitation of this new technique. Based on a reformulation of the basic equation physical properties of MRS soundings in that configuration are pointed out and interpreted. The influence of loop separation on MRS sounding curves in terms of offset and direction is also assessed as the corresponding sensitivity to depth and lateral Spin variation. Interpretation of real field data measured with separated loops fit excellently the predicted response pattern and confirm the correctness of the analytic formulation and its numerical realization.

Based on the promising results of MRS soundings in separated loop configuration and their outstanding spatial resolution to shallow structures the total resolution of a set of separated loop soundings on a profile to a two dimensional Spin distribution is investigated and compared to conventional coincident soundings. The introduction of a two dimensional kernel function allows a fast forward modeling of MRS sounding curves from a two dimensional water distribution and provides the basis for a draft 2D inversion scheme. Assessment of synthetic MRS surveys on three exemplary aquifer types and the model of an ice-ridge on arctic ice cover demonstrates the high resolution of separated loop surveys and its superior rendering of complex 2D water content distributions. Two field survey with this new technique have been performed in Nauen / Germany and StCyr en Val / France. In the first case a well defined model of the 2D water distribution could be found, in the latter case the model shows a poor resolution what could be assigned to 3D influences.

Zusammenfassung

Eine erweiterte mathematische Formulierung des Antwortsignals von Magnetischen Resonanz Sondierungen (MRS) ermöglicht die Behandlung von Messungen mit getrennten Sende- und Empfangsspulen. Die vorliegende Arbeit untersucht und bewertet die Möglichkeiten und Einschränkungen dieser neuartigen Messanordnung. Basierend auf einer geeigneten Umformulierung der Basisgleichung werden die verschiedenen physikalischen Effekte der MRS-Messungen in getrennter Spulenkonfiguration aufgezeigt und interpretiert. Der Einfluß der Spulenseparation in Bezug auf Abstand und Richtung wird ausführlich behandelt, wie auch die damit verbundene Variation der Empfindlichkeit mit der Tiefe aber auch in lateraler Richtung. Die Auswertung realer Daten mit getrennten Spulen in einem Gelände mit annähernd eindimensionalen Bedingungen zeigt eine hervorragende Übereinstimmung mit den vorhergesagten Eigenschaften der Sondierungskurven. Die Richtigkeit der analytischen Formulierung sowie der numerischen Umsetzung können somit bestätigt werden.

Aufgrund der vielversprechenden Ergebnisse der MRS Sondierungen mit getrennten Spulen in Bezug auf ihr ausgezeichnetes räumliches Auflösungsvermögen gegenüber flachen Strukturen wird die Gesamtempfindlichkeit mehrerer Sondierungen mit getrennten Spulen auf einem Profil untersucht und mit konventionellen Sondierungen mit gleicher Sende- und Empfangsspule verglichen. Die Einführung der zweidimensionalen Kernfunktion erlaubt eine einfache und schnelle Berechnung synthetischer Sondierungskurven aufgrund einer zweidimensionalen Wasserverteilung und bildet die Grundlage eines einfachen 2D Inversionsschemas. Die Bewertung von synthetischen MRS Messungen an drei exemplarischen Aquifer-Typen sowie dem Modell eines Presseisrückens wie er im arktischen Meereis vorkommt zeigt das hohe Auflösungsvermögen von Messungen mit getrennten Spulen und die deutlich verbesserte Wiedergabe von komplexen zweidimensionalen Wassergehaltsverteilungen. Zwei Feldkampagnen mit mehreren Kombinationen der getrennten Spulenordnung wurden in Nauen / Deutschland und StCyr en Val / Frankreich durchgeführt. Im ersten Fall konnte ein sehr detailliertes Modell der zweidimensionalen Wasserverteilung bestimmt werden. Im zweiten Fall zeigt das bestimmte Modell nur eine schwache räumliche Auflösung, was durch den dreidimensionalen Einfluß der Wasserverteilung erklärt werden kann.

Contents

1. Introduction	1
2. Properties of electromagnetic fields	5
2.1. Electromagnetic field propagation in conductive media	5
2.2. Attenuation and ellipticity	6
2.3. Decomposition	6
3. The Earth's magnetic field	13
4. The nuclear Spin in magnetic fields	17
4.1. Nuclear Magnetism	18
4.2. Nuclear Magnetic Resonance	21
4.3. The Bloch equations	22
4.4. Parameters of the Bloch equation in MRS applications	26
4.4.1. Spatial distribution of the loop field	26
4.4.2. Temporal variation of the Earth's field	31
4.4.3. Relaxation constants	33
4.5. Interpretation	33
5. The MRS response signal	35
5.1. Basic MRS formulation	35
5.2. Synthetic data	40
5.2.1. Spatial variation of the magnetic field components	43
5.2.2. Calibration soundings	43
5.2.3. The 1D Kernel	47
5.2.4. The 2D Kernel	49
5.3. Field data	58
6. Application of MRS to 2D water distributions	63
6.1. MRS modeling	63
6.2. 2D sensitivity	64
6.2.1. Pulse & sounding sensitivity	65
6.2.2. Section sensitivity	66
6.3. Synthetic data	68
6.3.1. Aquifer models	68

Contents

6.3.2. Ice-ridge	76
6.4. Real data	78
6.4.1. Nauen, Germany	81
6.4.2. StCyr en Val, France	83
7. Conclusion	89
8. Acknowledgements	93
Bibliography	95
A. Appendix to Chapter 1	101
A.1. Spatial propagation of electromagnetic fields in layered conductive media .	101
A.1.1. TE- and TM-modes	101
A.1.2. The scalar potential	101
A.1.3. Partial waves	103
A.1.4. Layer and strata impedances	104
A.1.5. Downward continuation	106
A.1.6. Coupling of the source fields to a conductive ground	106
A.2. Expressions for different source types	107
A.2.1. Vertical magnetic dipole (vmd)	107
A.2.2. Horizontal magnetic dipole (hmd)	109
A.2.3. Large horizontal loop	110
B. Appendix to Chapter 5	111
B.1. 2D kernels in x-z sections	111
B.2. 2D kernels in x-y maps	116
B.3. Complex representation	120

1. Introduction

The technique of Magnetic Resonance Sounding (MRS) was developed in the early eighties by Russian scientists. Based on the patent of Varian (1962), Hydroscope, the first MRS device was developed at the Institute for Chemical Kinetics and Combustions of the Siberian Branch of the Russian Academy of Science. Field results of subsurface water content determination with this method were first time published by Semenov (1987). Since 1996 the first, and until now only, commercial device is available by Iris Instruments, France. In 2000 the second generation of this device, the NUMISplus, was launched, with increased pulse power, a second pulse for T_1 measurements and optionally an additional receiver connection for separated loop measurements. It is currently the state of the art in MRS measurements.

Currently the development of the technique is concentrated in the workgroup of IRIS Instruments and the geological survey of France (Bureau de recherches géologiques et minières, BRGM), a russian group in Novosibirsk and the working group in Berlin. Here, since 1997, the Department of Applied Geophysics of the Technical University of Berlin in co-operation with the geological survey of Germany (Bundesamt für Geowissenschaften und Rohstoffe, BGR) are doing profound research on the fundamentals of the technique and its application. In several projects innovative approaches in signal processing and inversion, conductivity influence, scalability of the technique to larger and smaller scales and application of the technique to exploration and environmental problems are studied, covered by several master and PhD theses.

The application of MRS has been assessed in numerous field surveys and published in several case histories and reports. The direct sensitivity of the MRS technique to subsurface water makes it an essential tool for reliable aquifer determination and characterization. In particular the combination with conventional resistivity methods has been found to improve and extend hydrogeophysical interpretations. In two international workshops on the method of MRS, 1999 in Berlin and 2003 in Orleans, a comprehensive collection of methodological developments, field surveys and hydrogeological interpretation has been presented. A special issue on MRS has been published in 2002 (Journal of Applied Geophysics, 50, no. 1-2), a second one (Journal of Near Surface Geophysics) is currently in preparation.

In its technical development Magnetic Resonance Soundings were designed to operate with a single loop on the Earth's surface. This loop acts, as in most other technical NMR applications, both as transmitter to excite the Spin system, and as receiver to record the signal response after pulse cutoff. In recent publications the state of the art formulation of the signal response for this configuration was extensively presented in several review

1. Introduction

articles (e.g. Legchenko and Valla (2002); Yaramanci (2000)). Basically, an MRS device is the composition of a pulse generator and a transient recorder and signal analyzer, both controlled by a common microcontroller (Iris Instruments, 2000). The possibility to record a signal in a loop different from the transmitter loop is therefore self-evident. Anyhow, no measurement in that configuration with reasonable interpretation has been published yet.

A more general formulation of the complex valued MRS signal response has been introduced by Weichman et al. (2000, 1999), using an extended form to earlier publications on the theoretical foundation of MRS (Trushkin et al., 1995; Legchenko and Shushakov, 1998). The innovation in the extended formulation is the consideration of elliptically polarized electromagnetic fields of surface loops and the vectorial nature of the NMR phenomenon. In their publication they discuss the influence of subsurface conductivity on the complex valued MRS signal in detail. An analytic solution of the MRS response signal with separated loops is derived but not discussed in the course of the paper. In a later publication the same authors show a representation of an MRS 1D-kernel for separated loop configuration for the first time (Weichman et al., 2002). However, the authors restrict the discussion on the asymmetric property of the kernel and give no further interpretation. A first assessment of the properties of separated loops concerning the spatial signal distribution and corresponding sounding curve pattern with same type of transmitter and receiver loops but at changing positions was presented by Hertrich and Yaramanci (2003b) and Hertrich et al. (2004). The detailed physical description and assessment of separated loop soundings and their contribution to high resolution two dimensional water distribution mapping is comprehensively studied in this thesis.

Chapters 2 and 3 recapitulate the properties of the magnetic fields of the Earth and the loops as they later on enter the formulation of the MRS signal response.

In Chapter 5 a comprehensive description of the physical foundation of the evolution of the MRS signal for arbitrary loop configurations is given. The notation follows basically that of Weichman et al. (2000). However, for the sake of completeness the derivation of the fundamental equation for the MRS signal is sketched in an adequate extend to comprehend the origin of the observed effects. Based on a sensible decomposition of the general expression according their physical meaning an interpretation of distinguished parts is given and their spatial distribution graphically represented in a suitable way. On synthetic soundings with an assumed homogeneous water content of 100% the pattern of MRS soundings in dependency of loop offset are demonstrated. Complex valued sounding curve properties in dependency of loop separation direction and distance as well as influence of subsurface conductivity are systematically studied. Predicted sounding curves are affirmed by a field survey on a site with 1D conditions.

The conventional interpretation of MRS soundings assumes a perfectly 1D stratified Earth with a change in water content with depth. Estimations of misfit in data inversion of a non-1D water distribution with a 1D inversion have been previously assessed (Eikam, 2000; Warsa et al., 2002). Due to the large volume of signal contribution confined water bodies can not be accurately rendered by 1D inversion of a set of soundings along a profile. In

several publications pseudo-2D images were presented by contouring the results of 1D inversions (e.g. Abraham et al. 2003; Baltassat et al. 2003, among others). As studied by Warsa et al. (2002), this presentation leads to improper rendering of the true water content distribution, at least in case of small sounding point increment and small scale variations in lateral water content. First inversion results of MRS response signals to a real 2D water content distribution have been presented by Hertrich et al. (2004).

In chapter 6 the extension of the common 1D MRS kernel function to the 2D kernel function is introduced which finally allows a fast forward modeling of a synthetic MRS curve due to a 2D water content distribution and provides the basis for an inversion of a set of MRS soundings to a 2D water content distribution. Based on a basic inversion scheme the effort of full 2D inversion compared to 1D inversion of nearby soundings and their pseudo-2D representation in contour plots is demonstrated. A detailed study on selected synthetic aquifer models shows the improvement in spatial resolution by the use of separated loops compared to conventional coincident loops. The improved spatial resolution is confirmed by two exemplary field surveys with separated loops.

1. Introduction

2. Properties of electromagnetic fields

2.1. Electromagnetic field propagation in conductive media

The comprehension of the properties of induced magnetic fields by sources, i.e. current loops, over a conductive half-space is of major importance to validate effects as they occur in separated loop MRS measurements. The propagation of electromagnetic fields in conductive media generally causes elliptically polarized field vectors. This elliptical polarization can be physically and mathematically decomposed into two circular polarized field components which are co- and counter-rotating, respectively, in regard to the spinning sense of the hydrogen nuclei under investigation. The effect of elliptical decomposition in computations of MRS response signals has previously been assessed and compared to the linear approximation (Weichman et al., 2002; Valla and Legchenko, 2002; Braun et al., 2002; Braun and Yaramanci, 2003). It was found that the approximate generalization of the insulating kernel from Legchenko and Shushakov (1998) provides a suitable approach for coincident loop soundings at a wide range of common Earth's resistivities. In these cases the major part of the signal evolves from regions close to the loops so that the ellipticity of the magnetic fields plays a minor role and leads to small imaginary parts of the recorded signal. In case of separated loops, that are studied in this thesis, significant parts of the signal are induced in a distance from the source where the ellipticity of the loops reaches significant ranges and the complex MRS signal shows noticeable quadrature components determined by the asymmetry of co- and counter-rotating parts of the magnetic fields of transmitter and receiver, as will be shown in section 5.2.2.

Modeling of electromagnetic fields considering conductivity effects within this thesis is performed with a numerical approach based on an algorithm of Weidelt (1984). The analytical derivation of the induced fields in conductive layered media is given in Appendix A.1. For more complicated structures, i.e. a two or three dimensional conductivity distribution, no such analytical solution can be easily found. For this purpose the forward calculation of electromagnetic fields requires an extended numerical approach, which is beyond the scope of this thesis.

2. Properties of electromagnetic fields

2.2. Attenuation and ellipticity

The inhomogeneous field close to the source undergoes two damping effects. The major impact has the geometrical spreading of the fields close to the source. For a wire loop this effect accounts several orders of magnitude within one diameter of distance. The second attenuation effect is the electromagnetic attenuation due to induction. For plane waves, i.e. zero wavenumber, this effect is described by the skin depth (Ward and Hohmann, 1988). An according expression for the vertical attenuation can be analogously derived for any arbitrary wavenumber. The full vector field, however, is the superposition of the full wavenumber spectrum as it is formulated in equations A.11 and A.12. Therefore, no equivalent expression to the plane wave skin depth can be given in case of inhomogeneous fields.

Equations A.38 and A.39 in Appendix A.1 show that horizontal and vertical components of the magnetic fields are differently influenced by electromagnetic attenuation. Consequently, they are non-collinear and the effective electromagnetic field at any point in the subsurface, the vector sum of both components, is consequently elliptically polarized (see e.g., Jackson, 1983, p 321). Let the ellipticity of the field be defined as the ratio of minor and major semi-axes of the ellipse. Then, an ellipticity equal to zero describes a linear polarized field, an ellipticity equal to 1 a circular polarized one. The ellipticity provides an amplitude independent measure of magnetic field distortion due to induction. Figure 2.1 shows sections of the magnetic field distribution of a 100m circular loop on a homogeneous half-space with resistivities ranging from $5000\Omega m$ to $5\Omega m$. The magnitude of the total magnetic field (left column) as well as the vertical and horizontal components (center columns) show only a slight damping from $5000\Omega m$ to $50\Omega m$. For the same resistivity variation, the plane wave electromagnetic skin depth is decreased by a factor of ten. More significant damping effects are observed for resistivities down to $5\Omega m$ (bottom row). However, the damping of the fields mainly occurs far from the loop center. Within one diameter distance from the loop center the electromagnetic damping is still less prominent. As demonstrated, the magnitude of the electromagnetic field is only slightly influenced down to quite low Earth's resistivities. The distortion of the electromagnetic field, expressed by ellipticity, is evidently stronger influenced by subsurface resistivity. Comparing the ellipticity of $5000\Omega m$ to $50\Omega m$, for example, where only slight differences of magnitude are observed, the ellipticity of the field is significantly increased. The effect of induction to the distribution of electromagnetic fields for common resistivity ranges found in geophysical applications mainly affects its distortion, measured here as ellipticity, rather than in an effective damping of the field magnitude.

2.3. Decomposition

To determine the physically acting components of the elliptically polarized field on the Spin system under investigation in MRS applications I refer to the parameterization introduced

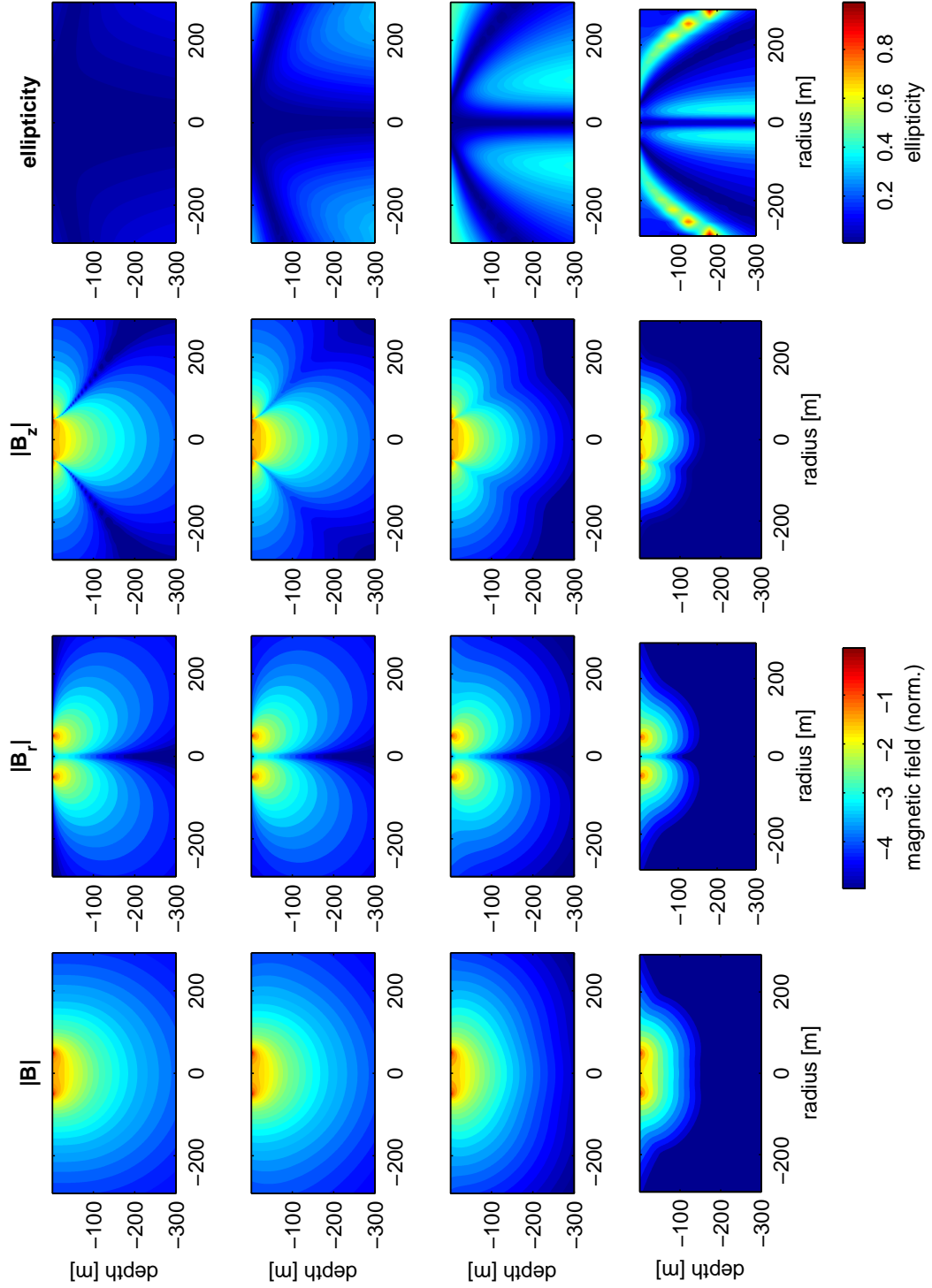


Figure 2.1.: Cross-sections of the electromagnetic field of a loop of 100m diameter for the total field (left column), its radial and vertical component (center left and center right column) and the ellipticity of the field (right column) for resistivities, from top to bottom, of $5000\Omega m$, $500\Omega m$, $50\Omega m$ and $5\Omega m$.

2. Properties of electromagnetic fields

by Weichman et al. (2000) (also in a quite descriptive derivation in Braun, 2002 and as a more general, brief summary in Becken and Burkhardt, 2004).

For any arbitrary point in the subsurface the magnetic field vector $\mathbf{B}_T(t)$ oscillating in the time domain can be represented by the frequency dependent expression

$$\mathbf{B}_T(t) = I_T^0 [\mathcal{B}_{T,1}(\omega_L) \cos(\omega_L t) + \mathcal{B}_{T,2}(\omega_L) \sin(\omega_L t)], \quad (2.1)$$

in which ω_L is the Larmor frequency of the Spin system and

$$\mathcal{B}_T(\pm\omega_L) = \mathcal{B}_{T,1}(\omega_L) \pm i\mathcal{B}_{T,2}(\omega_L) = \mathcal{B}_T^*(\mp\omega_L) \quad (2.2)$$

is the complex field amplitude. By this notation the complex representation of $\mathbf{B}_T(\mathbf{r}, t)$ is given by

$$\mathbf{B}_T(t) = \frac{1}{2} I_T^0 [\mathcal{B}_T(\omega_L) e^{-i(\omega_L t + \varphi)} + \mathcal{B}_T(-\omega_L) e^{i(\omega_L t + \varphi)}]. \quad (2.3)$$

or in a more condensed expression

$$\mathbf{B}_T(t) = \text{Re} (I_T^0 e^{-i(\omega_L t + \varphi)} \mathcal{B}_T(\omega_L)). \quad (2.4)$$

In NMR applications, only the component of the oscillating magnetic field perpendicular to the equilibrium orientation of the Spins, i.e. the static field, physically acts on the Spin excitation. In case of a Spin system being oriented along the Earth's magnetic field $\mathbf{B}_0 = B_0 \cdot \hat{\mathbf{b}}_0$, the effective component of the electromagnetic field of the loop is simply the projection of the loop field into the plane perpendicular to \mathbf{B}_0

$$\begin{aligned} \mathbf{B}_T^\perp &= \mathbf{B}_0 - (\hat{\mathbf{b}}_0 \cdot \mathbf{B}_T) \hat{\mathbf{b}}_0 \\ \mathbf{B}_T^\perp &= \hat{\mathbf{b}}_T B_T^\perp, \end{aligned} \quad (2.5)$$

where $\hat{\mathbf{b}}_T$ is the unit direction vector of the perpendicular component. In case of an elliptically polarized loop field \mathbf{B}_T , its perpendicular component is also elliptically polarized, unless the Earth's field direction lies in the polarization plane of the loop field. For the perpendicular component the same complex representation of equation A.57 is valid and yields

$$\mathbf{B}_T^\perp(t) = \frac{1}{2} I_T^0 [\mathcal{B}_T^\perp(\omega) e^{-i(\omega_L t)} + \mathcal{B}_T^\perp(-\omega_L) e^{i(\omega_L t)}]. \quad (2.6)$$

Thus the complex magnetic field vector \mathbf{B}_T^\perp lies in the plane spanned by $\hat{\mathbf{b}}_T$ and $\hat{\mathbf{b}}_T \times \hat{\mathbf{b}}_0$. It can be decomposed in its elliptical components α_T , β_T and ζ_T .

$$\mathcal{B}_T^\perp(\omega_L) e^{-i\zeta_T(\omega_L)} = [\alpha_T(\omega_L) \hat{\mathbf{b}}_T(\omega_L) + i\beta_T(\omega_L) \hat{\mathbf{b}}_0 \times \hat{\mathbf{b}}_T(\omega_L)]. \quad (2.7)$$

2.3. Decomposition

Where the phase ζ_T is chosen in such a way that α_T and β_T are real and $\alpha_T \geq |\beta_T| \geq 0$. The parameters α_T and β_T are the major and minor semi-axes of the ellipse and the phase ζ_T determines the orientation of the vector at $t = 0$. The complex field amplitude of equation 2.7 can then be written as

$$\mathbf{B}_T^\perp(\omega_L) = e^{i\zeta_T(\mathbf{r}, \omega_L)} \left[\alpha_T(\omega_L) \hat{\mathbf{b}}_T(\omega_L) + i\beta_T(\omega_L) \hat{\mathbf{b}}_0 \times \hat{\mathbf{b}}_T(\omega_L) \right]. \quad (2.8)$$

From the equalities

$$\begin{aligned} \mathbf{B}_T^\perp \cdot \mathbf{B}_T^\perp &= (\alpha_T^2 - \beta_T^2) e^{2i\zeta} \\ \mathbf{B}_T^\perp \cdot \mathbf{B}_T^{\perp*} &= \alpha_T^2 + \beta_T^2 \\ \mathbf{B}_T^\perp \times \mathbf{B}_T^\perp &= -2i\alpha_T\beta_T \hat{\mathbf{b}}_0 \end{aligned} \quad (2.9)$$

one obtains after some algebra for the ellipse parameters

$$\begin{aligned} \alpha_T &= \frac{1}{\sqrt{2}} \sqrt{|\mathbf{B}_T|^2 + |(\mathbf{B}_T)^\perp|^2} \\ \beta_T &= \text{sign} \left[i\hat{\mathbf{b}}_0 \cdot \mathbf{B}_T^\perp \times \mathbf{B}_T^{\perp*} \right] \frac{1}{\sqrt{2}} \sqrt{|(\mathbf{B}_T^\perp)|^2 - |(\mathbf{B}_T)^\perp|^2} \\ e^{i\zeta_T} &= \sqrt{\frac{(\mathbf{B}_T^\perp)^2}{|(\mathbf{B}_T^\perp)|^2}}. \end{aligned} \quad (2.10)$$

Here, the complex field vectors entering the above equations are obtained by calculations from subsection A.1.5. Decomposing the elliptically polarized field vector into the sum of two oppositely rotating circular polarized fields yields

$$\mathbf{B}_T^\perp(t) = \mathbf{B}_T^+(t) + \mathbf{B}_T^-(t), \quad (2.11)$$

where the two parts are rotating clockwise and counterclockwise in respect to $\hat{\mathbf{b}}_0$, respectively. Their magnitudes are derived from the elliptical components as

$$\mathbf{B}_T^+(t) \equiv \frac{1}{2} I_T^0 (\alpha_T - \beta_T) \left[\cos(\omega_L t + \zeta_T) \hat{\mathbf{b}}_T - \sin(\omega_L t - \zeta_T) \hat{\mathbf{b}}_0 \times \hat{\mathbf{b}}_T \right] \quad (2.12)$$

$$\mathbf{B}_T^-(t) \equiv \frac{1}{2} I_T^0 (\alpha_T + \beta_T) \left[\cos(\omega_L t - \zeta_T) \hat{\mathbf{b}}_T + \sin(\omega_L t + \zeta_T) \hat{\mathbf{b}}_0 \times \hat{\mathbf{b}}_T \right] \quad (2.13)$$

and consequently their magnitudes, being the radii of the respective circular polarized fields, as they will enter the MRS equation in chapter 5.1

$$|\mathbf{B}_T^+| = \frac{1}{2} I_T^0 (\alpha_T - \beta_T) \quad (2.14)$$

$$|\mathbf{B}_T^-| = \frac{1}{2} I_T^0 (\alpha_T + \beta_T). \quad (2.15)$$

2. Properties of electromagnetic fields

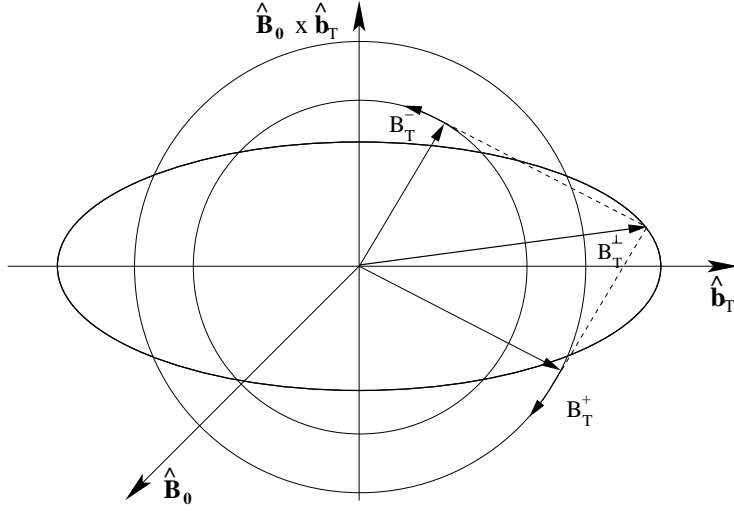


Figure 2.2.: Decomposition of an elliptically polarized field in the plane $[\hat{\mathbf{b}}_0 \times \hat{\mathbf{b}}_T; \hat{\mathbf{b}}_T]$ with semi-axes $\alpha_T; \beta_T$ and its decomposition into co- and counter-rotating parts $|\mathbf{B}_T^+|$ and $|\mathbf{B}_T^-|$.

The geometry of the elliptically polarized field and its decomposition into circular components is graphically shown in figure 2.2. The spatial distribution of the respective elliptical parameters and the corresponding co- and counter-rotating parts was extensively studied by Braun (2002) and is exemplarily presented for a circular loop of 100m diameter on a $10\Omega m$ half-space in figure 2.3.

In regard to the spinning sense of hydrogen nuclei clockwise around the static field both parts will be referred to as co- and counter-rotating parts in the further progress of this thesis.

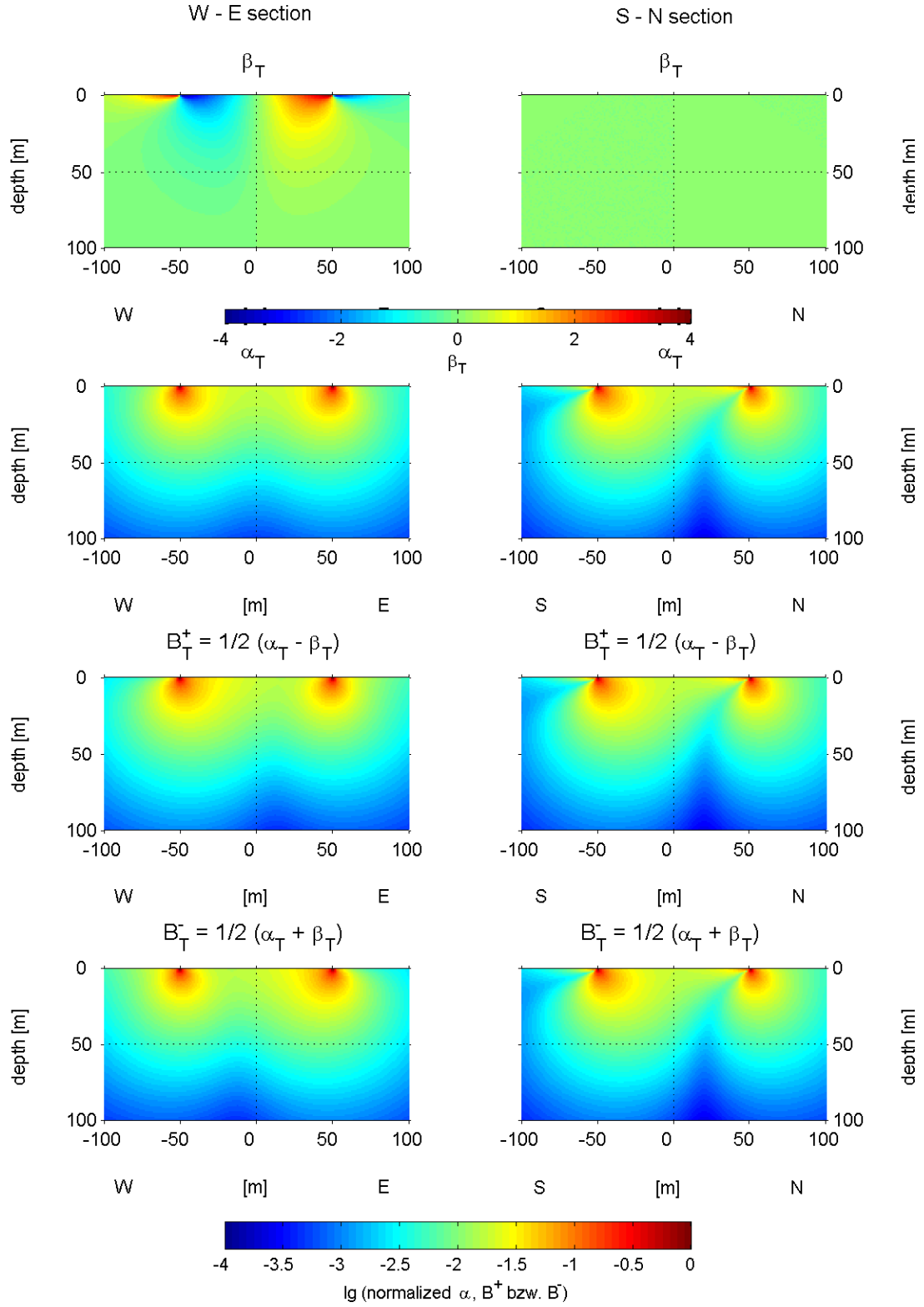


Figure 2.3.: West-East (left column) and South-North (right column) sections of the parameters α_T , β_T , B_T^+ and B_T^- for a circular loop of 100m, $10\Omega m$ half-space, Earth's magnetic field of 48986nT at 60° inclination (after Braun, 2002).

2. *Properties of electromagnetic fields*

3. The Earth's magnetic field

The static magnetic field for the NMR experiment in MRS applications is provided by the Earth's magnetic field. In the vicinity of the Earth's surface it is, as a first order approximation, a dipole field. Its magnitude varies from around 22000nT to more than 65000nT. In detail, the global distribution of the Earth's magnetic field amplitude deviates significantly from the dipole approximation. The maxima of the global field are not at the poles, but deflected to latitudes of some 60°. The global minimum is located in southern Brasil, South America. Figure 3.1 shows the distribution of the magnitude (a) and the inclination (b) of the Earth's magnetic field according to the National Geophysical Data Center (NGDC) World Magnetic Model (WMM)¹. The inclination distribution, however, correlates roughly to a dipole field.

The dependency of the MRS signal on amplitude and inclination is of opposite sense. With increasing Earth's field amplitude the Spin magnetization increases and leads to an increasing NMR signal. With decreasing inclination the induced excitation fields are in average at higher angles to the static field and lead to a higher signal response at lower latitudes. After all the effect of larger static field amplitudes dominates and larger MRS signal are usually recorded at higher latitudes. However, the non-uniform dependency of Earth's field amplitude and geographic latitude makes an individual assessment necessary for expected MRS signal response amplitude and penetration depth. The Internet sites of the NGDC are here quite helpful since they provide an Earth's field calculator to determine amplitude, inclination, and declination for arbitrary coordinates. Prior to a survey expected maximum response signals can so be estimated by appropriate modeling.

The magnetic field on the Earth's surface is additionally influenced by external magnetic sources. Significant influence has the electrical conductive Ionosphere of the Earth in around 300km altitude. Whenever this conductive Ionosphere is stimulated by tidal forces or diurnal warming, an electric current is induced (Berckhemer, 1990, pp. 143). This current in turn induces a magnetic field that superimposes the intrinsic Earth's magnetic field and is known as diurnal magnetic variation. This variation depends on latitude, time of the day, season, and lunar activity. It accounts some 10-40nT of magnitude, with a characteristic minimum at noon leading to a MRS Larmor frequency variation of some few Hertz. In addition to the periodic diurnal variation aperiodic variation frequently occur, known as "variations" ($t > 10\text{min}$), "Pulsations" ($0.2 < t < 600\text{s}$) and "Spherics". The latter are magnetic influences by natural sources like thunderstorms and other meteorological events. Considerably strong changes are caused by magnetic storms, correlated to lunar eruptions.

¹Magnetic field calculator and maps are available under www.ngdc.noaa.gov/seg/geomag/geomag.shtml

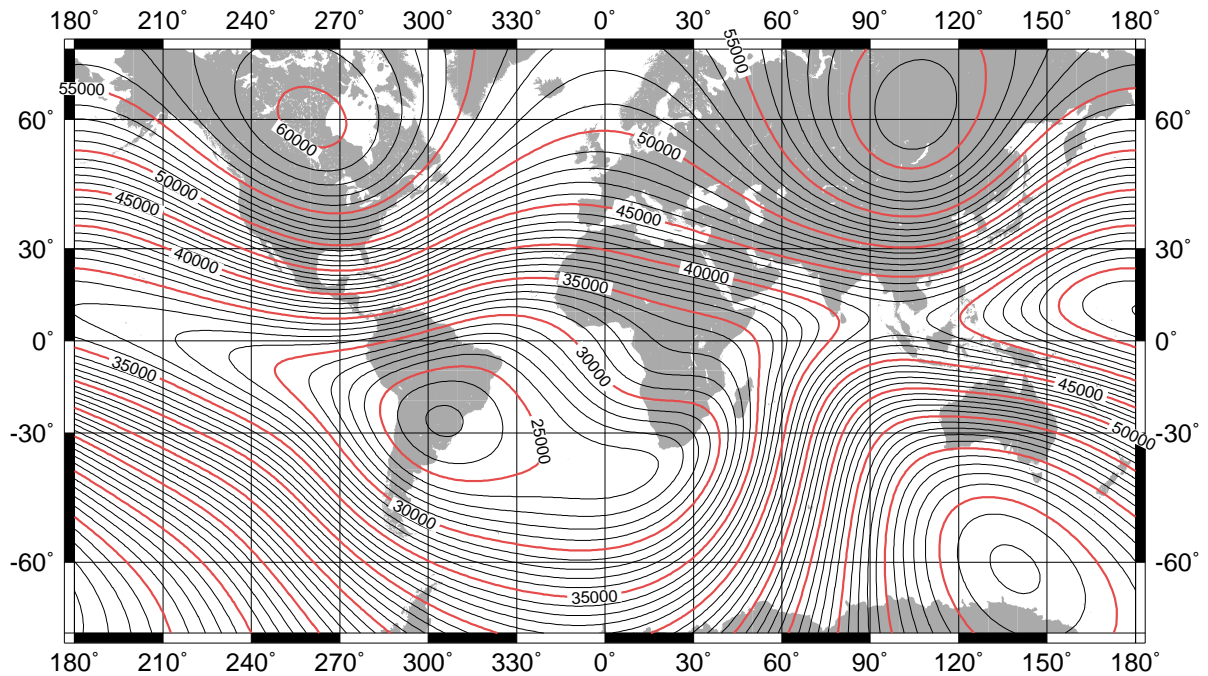
3. *The Earth's magnetic field*

These events occur simultaneously around the globe. Intensive ionic particle radiation affects the Earth's magnetic field around 24h after its emission on the sun by several hundred nT, even up to 3000nT have been recorded. After such an event, it can take up to several days until the Earth's magnetic field returns to its normal value. For a MRS survey the static magnetic field should have low variations. A variation of less than 1Hz during a sounding is recommended. Prior to a field survey the local magnetic field conditions should therefore be checked by actual data from the closest magnetic observatory. These data are available under www.intermagnet.org. There, a space weather forecast with oncoming magnetic storms provides additional information whether magnetic field conditions are favorable for a planned survey.

In addition to global and regional variations of the Earth's field local variations of the magnetic field can be caused by rock formations of high magnetic susceptibility. In these cases a vertical or horizontal gradient can cause a spatial variation of the Larmor frequency and therefore significantly disturbed sounding curves. In case of fine disseminated magnetic particles in the subsurface the large internal gradient provokes a de-phasing of the Spin magnetization and leads to very short T_2^* times what causes in some cases an unmeasurable MRS signal. A profound knowledge of the geological setting is therefore mandatory for a correct setup and interpretation of MRS measurements. Estimation of suitable Earth's magnetic properties is given in the NUMISplus operation manual by susceptibility values of the ground of less than 10^{-3} SI-units for good conditions and $10^{-3} - 10^{-2}$ SI-units for moderate conditions. According the manual no MRS signal is measurable if ground susceptibility of more than 10^{-2} SI-units are observed. A comprehensive survey should consequently be accompanied by susceptibility measurements of the ground and in outcrops in various places around the loop area.

US/UK World Magnetic Chart -- Epoch 2000

Total Intensity - Main Field (F)



US/UK World Magnetic Chart -- Epoch 2000

Inclination - Main Field (I)

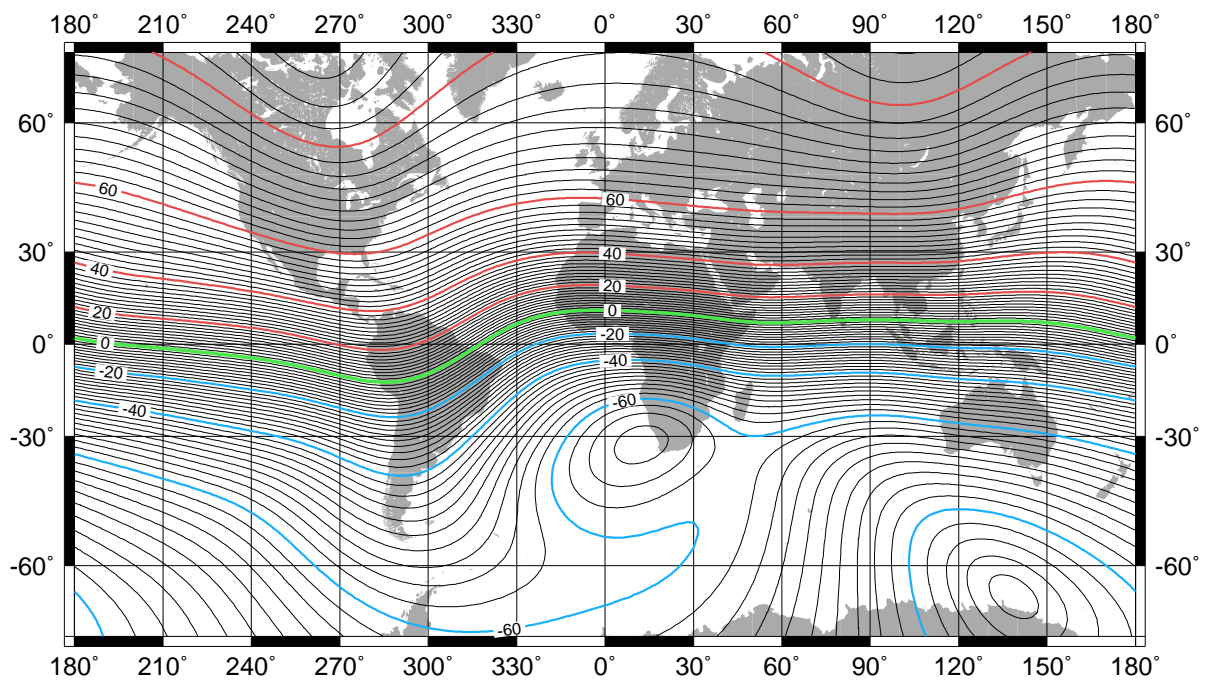


Figure 3.1.: Earth's magnetic field global distribution

3. The Earth's magnetic field

4. The nuclear Spin in magnetic fields

Atomic nuclei possess four intrinsic physical properties. These are an electric charge, a specific mass, a microscopic magnetization, and the Spin. The first three properties are easily tangible as they have a corresponding property in the macroscopic world. Matter is made of atoms, i.e. nuclei. And matter has a mass, frequently a charge and sometimes a magnetization. But there is no such thing as macroscopic Spin, the property to have an angular momentum without rotating. However, the physical property of nuclear Spin can be used for various experiments and allows one to spy into the internal structure of matter.

The nuclear magnetization itself is vanishingly small and hardly detectable by physical experiments. Only the combination of the nuclear magnetization and the intrinsic angular momentum allows one to exploit the physical properties experimentally. In absence of an electrical or magnetic field these are degenerated, but split into $[I(I+1)]$ discrete sub-levels if a field is applied. The Spin, i.e. the angular momentum of particles is basically quantized in values of $[I(I+1)]^{\frac{1}{2}}\hbar$, where I is the spin quantum number and \hbar is Planck's constant. For some particles this Spin quantum number is given by whole integers (bosons), for others by half integers (fermions). The Spin of elementary particles is intrinsic, they just have Spin. Molecules on the other hand acquire their rotational angular momentum by energetic collisions. The microscopic magnetization μ is coupled to the Spin angular momentum by $\mu = \gamma\hbar I$. In the absence of external fields the microscopic Spin magnetization is randomly distributed and consequently leads to mutual cancellation for an ensemble of Spins in a system. Only in the presence of an external field the unequal allocation of discrete energy levels leads to a macroscopic resulting magnetization called the net magnetization. The order of poles depends on the spin quantum number of the nuclei. For $I = \frac{1}{2}$ the nuclei generally possess magnetic dipole moments, whereas higher Spin quantum numbers also allow higher orders of poles, namely quadrupoles.

The method of Nuclear Magnetic Resonance (NMR) is based on the interaction of these magnetic dipole moments placed in a static field with an external monochromatic field exactly at the angular frequency of the Spin, the resonance condition. For the application of Magnetic Resonance Soundings (MRS) in subsurface investigations the pore water, i.e. the hydrogen nuclei of the pore water, is the target of investigation. Considerations in this work therefore only regard the magnetic properties of the hydrogen nucleus.

The property of Spin and its nuclear magnetism was found and proved by early classical experiments as the Zeemann effect or the Stern-Gerlach experiment at the end of the 19th century. In the 1940ies Bloch, Hansen and Packard as well as Purcell, Torrey and Pound

4. The nuclear Spin in magnetic fields

independently described the magnetic resonance phenomenon as it is used nowadays in physical applications.

4.1. Nuclear Magnetism

The orientation of the microscopic magnetic dipoles in a homogeneous static field is either parallel - most stable - or anti-parallel - least stable - to even this field. Each individual Spin can change its orientation spontaneously from one orientation to the other. However, this transition is quite improbable, but can be stimulated by the absorption of energy quanta from an applied electromagnetic field. The probability of absorption is highest if the energy quanta of the oscillating-field equals the energy difference between the two orientations (Zeemann-levels). Therefrom the resonance condition follows immediately. Quantitatively the resulting magnetization can be described as follows:

In their ground state, the nuclei under consideration possess a finite angular momentum \mathbf{I} , and consequently a coupled magnetic moment

$$\mu = \gamma \hbar I \quad (4.1)$$

with $h = \hbar * 2\pi$, the Planck's constant and *gamma*, the gyromagnetic ratio which correlates the angular frequency with to the static field magnitude. For the hydrogen nucleus we find in literature

$$I_p = +\frac{1}{2} \quad (4.2)$$

$$\begin{aligned} \gamma_p &= 2.675152581 * 10^8 \frac{1}{T * s} \\ &= 0.2675152581 \frac{Hz}{nT} \end{aligned} \quad (4.3)$$

$$\mu_p = 1.41119 * 10^{-26} \frac{J}{T}. \quad (4.4)$$

In the presence of a static magnetic field, the angular momentum and consequently the specific resulting magnetic moment μ_p can only take $2I + 1$ different states with the corresponding values of the z-component

$$\mu_z = j\gamma\hbar \quad j = I, I-1, \dots, -(I-1), -I. \quad (4.5)$$

where μ_z is the component of the magnetization in direction of the static field \mathbf{B}_0 . The energy state in this field is given by (see e.g. Michel, 1981, p. 30)

$$W_m = -\mu_z \mathbf{B}_0 = -j\gamma\hbar \mathbf{B}_0 \quad (4.6)$$

$$= \pm \frac{1}{2} \gamma \hbar \mathbf{B}_0. \quad (4.7)$$

4.1. Nuclear Magnetism

The state effectively splits in $2I + 1$ energetic states. So, for the hydrogen nucleus with $I = \frac{1}{2}$ a dipole moment with energetic states $-\mu_z$ and $+\mu_z$ is obtained. For the energy difference of both levels then follows

$$\Delta W = \gamma \hbar \mathbf{B}_0. \quad (4.8)$$

Applying Bohr's condition $\Delta W = h * f$ immediately yields the precondition for the resonance frequency, called Larmor frequency

$$2\pi f = -\gamma \mathbf{B}_0, \quad (4.9)$$

at which the energy quanta are absorbed to shift the Spins onto a higher level and that Spins emit when they skip to a lower one.

The property of Spin to polarize into two populations on different energy levels is used in various classical physical experiments (Zeemann-effect, Stern-Gerlach-experiment, Rabi-experiment). However, in resonance applications the macroscopic magnetization of an ensemble of Spins is exploited. The physical foundation for the development of a resulting magnetization evolves by introducing the Boltzmann equation. It describes the probability p_m for a single Spin to reside on a certain energy level E_m

$$p_m \propto e^{-\frac{E_m}{kT}} \quad (4.10)$$

where k is Boltzmann constant and T the absolute temperature. From a large number of Spins, the allocation of both states splits according to the respective probability into:

$$N_{\pm} \propto e^{-\frac{E_{\pm}}{kT}} \quad (4.11)$$

The ratio of both states in thermal equilibrium is then

$$\frac{N_+}{N_-} = e^{-\frac{\Delta E}{kT}} = e^{-\frac{hf}{kT}}. \quad (4.12)$$

The logarithm of this expression can be linearized for $hf \ll kT$ what is definitely the case for absolute temperatures above some few Kelvin. So we finally find for the difference of both populations

$$N_+ - N_- = \left(\frac{\gamma \hbar B_0}{kT} \right) N_+ \approx \left(\frac{\gamma \hbar B_0}{2kT} \right) N. \quad (4.13)$$

An alternative formulation of the resulting magnetization can be derived by the statistical accumulation of Spins on both energy levels. The expectation of the resulting magnetiza-

4. The nuclear Spin in magnetic fields

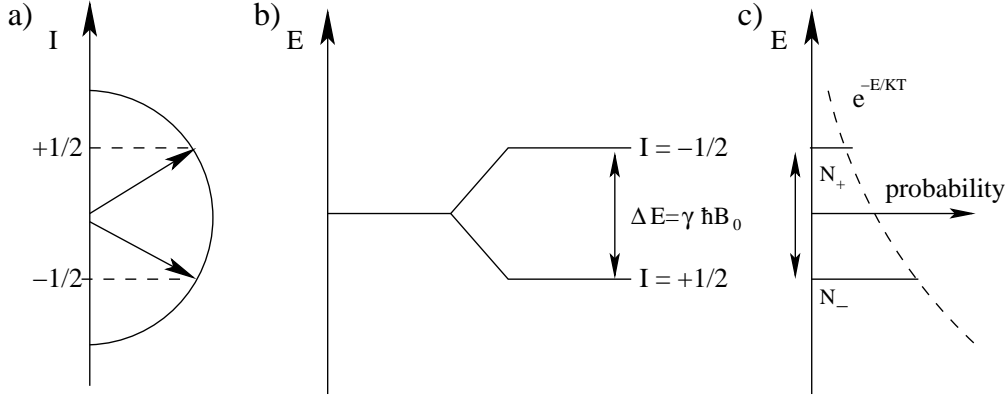


Figure 4.1.: Possible orientations of a nuclear Spin with an angular momentum $I=1/2$, exposed to a static field (left). Splitting of the energy levels in the presence of a static field (middle). For a transition between the two possible states an energy quantum of $\Delta E = \gamma \hbar B_0$ is necessary (right). The probability of both states follows the Boltzmann distribution, the exponentially decaying curve.

tion is identical to the sum of the number of Spins and their Boltzmann factors:

$$\langle \mu_z \rangle = \sum_{m=-I}^{+I} (\mu_z)_m * p_m \quad (4.14)$$

$$= (\mu_z)_- * p_- + (\mu_z)_+ * p_+ \quad (4.15)$$

$$= (e^{-\frac{E_+}{kT}} - e^{-\frac{E_-}{kT}}). \quad (4.16)$$

Both solutions indicate that the difference of the number of Spins on the two energy levels is extremely small. So only a homeopathic overage of Spins on the higher energy state establish and finally leads to a resulting magnetization, called the net magnetization. The net magnetization is then given by

$$\mathbf{M}_0 = {}^1N * \langle \mu_z \rangle, \quad (4.17)$$

where 1N is the number of Spin participating the experiment. Using 4.13, the magnitude of the net magnetization is given by

$$M_0 = \frac{\gamma^2 \hbar^2 B_0 \rho_0}{3kT} I(I+1) = \frac{\gamma^2 \hbar^2 B_0 \rho_0}{4kT}, \quad (4.18)$$

which is known as Curie's law. Here, $\rho_0 = N/V$, is the number of Spins per volume. The magnetization is obviously induced by an external field, so according to magnetic media the a magnetic susceptibility κ can be defined. The net magnetization can then be rewritten

as

$$\mathbf{M}_0 = \mu_0 V \kappa \mathbf{B}_0, \quad (4.19)$$

where V is the volume under investigation. The susceptibility of water, for example, is $\kappa_w = -90 \times 10^{-6}$. The development of a macroscopic Spin magnetization is generally caused by an external field. The direction of the magnetization vector is consequently the same then the external field direction, so

$$\frac{\mathbf{M}_0}{|\mathbf{M}_0|} = \frac{\mathbf{B}_0}{|\mathbf{B}_0|} \quad (4.20)$$

From the above formulation result two important properties for NMR in the Earth's field range

- The Larmor frequency of Spin is proportional to the static field strength. For the Earth's field strength of $50\mu T$ we achieve Larmor frequencies around $2kHz$, which is in the audio frequency range.
- The more important feature is that the net magnetization, which finally determines the amplitude of the NMR response, is also proportional to the static field strength. At around $50\mu T$ in the Earth's field, the net magnetization for a fixed volume compared to NMR applications on Earth's materials in laboratory at $0.5T$ and a corresponding Larmor frequency of $2GHz$ or borehole tools at $0.05T$ and $200MHz$, is according equation (4.19) of a factor of 10^6 , respectively 10^5 , smaller. This explains the small response amplitudes of the MRS signal compared to laboratory and borehole measurements, even though a huge volume is sensed.

4.2. Nuclear Magnetic Resonance

The methods of Nuclear Magnetic Resonance are based on the generation and the measurement of an interaction between the magnetic moments of the nuclear magnetization in a static field and an externally applied monochromatic field. The resulting magnetization of a Spin ensemble is subject of a permanent competition of two opposite forces: on one hand the exciting oscillating field aims to demagnetize the Spin system by disturbing the thermal equilibrium of Spins on the different Zeemann levels of energy. On the other hand the demagnetized system re-equilibrates by loosing energy in Spin-Spin interactions and thermal movements. Both phenomena are time dependent and from this property one can directly derive the two basic NMR methods: Pulse-NMR and steady-state-NMR.

In pulse methods the Spin system is stimulated exactly at resonance frequency (or at least as exact as possible) with a pulse duration significantly weaker than the relaxation time constant and with a secondary field significantly smaller than the primary. The influence of

4. *The nuclear Spin in magnetic fields*

the relaxation forces is then ought to be negligible during the excitation and the transient relaxation of the transverse component of the net magnetization after pulse cutoff is the object of observation.

In steady state methods the pulse is long enough that both excitation and relaxation forces are in equilibrium. Here, the resulting magnetization in equilibrium is the aim of the measurement. Amplitude and phase of the resulting magnetization are a function of frequency deviation between exciting field and Larmor frequency. So the measurement is performed as a sweep of a frequency range to obtain information about the Spin system. The characteristic frequency dependency is a Lorentz curve where the maximum indicates the resonance frequency and the width correlates to the relaxation constant.

In steady-state NMR signal amplitudes are significantly smaller than in pulse methods. Additionally, pulse methods are significantly faster to perform and allow a large number of experimental variations to access different Spin properties. Even though steady state methods had historically the more significant impact in the exploration of the Nuclear Magnetic Resonance phenomenon, they are nowadays practically endangered.

In surface applications as they are discussed in this thesis, none of the preceeding assumptions is correctly met. To generate pulses with sufficient energy to sense a suitable volume of investigation, pulse durations are necessary that are not generally small compared to the expected relaxation constants in the investigated subsurface. The emitted magnetic fields are in the range and sometimes even stronger than the static field given by the Earth's field. And finally the Earth's field is spatially very homogeneous but is not constant during a measurement period due to daily variations and occasionally magnetic storms. So the resonance condition is not always perfectly met and the variation of contributing parameters is out of the researcher's influence. In all common investigations of the NMR phenomenon it is possible to control the respective parameters accurate enough to apply the common approximations. So, in established literature both pulse and steady state NMR are extensively discussed and explained (Abragam, 1983; Levitt, 2002), but the general solution of the intermediate case is rarely discussed and mostly neglected (Abragam, 1983). A comprehensive discussion of the general case is found in Torrey (1949). In later publications on selective pulses the case of resonance deviations is also found (Mansfield et al., 1979), but with limitations to appropriate magnetic field ratios and negligible pulse lengths. Based on the solution of Torrey, the influence of the experiment parameters on a model unit magnetization is discussed and the effect on MRS measurements demonstrated in the following.

4.3. The Bloch equations

In equilibrium a Spin magnetization in a static magnetic field is orientatied along the direction of the static field \mathbf{H}_0 , the z-direction of a laboratory coordinate system (Fig. 4.2a). It is then perturbed by a pulse acting perpendicular to its orientation, forcing it

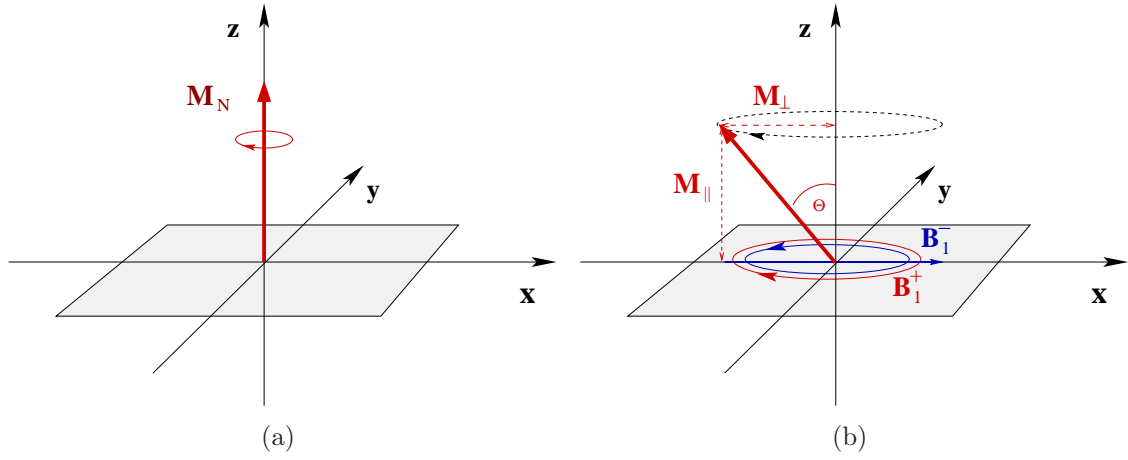


Figure 4.2.: (a) orientation of a nuclear magnetization and (b) its interaction with a oscillating field perpendicular to it.

onto a precessional motion around its axis in the x-y-plane (Fig. 4.2b). The time dependent magnetization evolution is given by the semi-quantitative classical Bloch Equation:

$$\frac{dM_y}{d\tau} + \beta M_y + \delta M_x = 0 \quad (4.21)$$

$$\frac{dM_x}{d\tau} + \beta M_x - \delta M_y + M_z = 0 \quad (4.22)$$

$$\frac{dM_z}{d\tau} + \alpha M_z - M_x = M_0 \quad (4.23)$$

where the following substitutions are valid:

$$\begin{aligned} \tau &= \gamma H_1 t & \delta &= \frac{(\omega_0 - \omega)}{\gamma H} \\ \alpha &= \frac{1}{\gamma H_1 T_1} & \omega_0 &= \gamma H_0 \\ \beta &= \frac{1}{\gamma H_1 T_2} & M_0 &= \kappa H_0 \end{aligned} \quad (4.24)$$

with time t , the gyromagnetic ratio γ and the static susceptibility κ_0 . These equations provide a set of differential equations that describe the temporal development of amplitude and orientation of the resulting magnetization vector. The evolution depends on the parameters pulse duration t , relaxation constants T_1 and T_2 , deviation between excitation and precession frequencies $(\omega_0 - \omega)$ and the magnitudes of the static and exciting magnetic fields H_0 and H_1 . In the Laplace domain this set of equations can be arranged such that the back transformation yields the solution

$$w = Ae^{-a\tau} + Be^{-b\tau} \cos(s\tau) + \frac{C}{s} e^{-b\tau} \sin(s\tau) + D \quad (4.25)$$

4. The nuclear Spin in magnetic fields

In this expression w represents one of the three normalized Cartesian components M_x/M_0 , M_y/M_0 oder M_z/M_0 . The first three terms of the solution represent transient processes in the magnetization evolution, the third term represents the steady state solution. No analytical solution can be found for the general case of all arbitrary parameters. However for certain assumptions a solution is possible. These are:

1. The frequency of excitation is exactly the resonance frequency of the Spins, i.e. $\delta = 0$.
2. The longitudinal relaxation equals the transversal, i.e. $T_1 = T_2$.
3. The exciting field is large enough to satisfy $\alpha, \beta \ll 1$.

As discussed before, the first and third conditions are not valid in MRS applications. However for weak static fields as found in geophysical applications, the second condition is assumed to hold (Bene, 1979).

Assuming the precondition $T_1 = T_2$ we find the following solution:

$$T_1 = T_2 \quad (4.26)$$

$$\alpha = \beta. \quad (4.27)$$

and following Torrey (1949), with $\alpha = \beta$, for a, b and s

$$a = b = \beta \quad (4.28)$$

$$s^2 = 1 + \delta^2 \quad (4.29)$$

particular solutions for coefficients of equations 4.21-4.23 are found and consequently yields for the respective parts of the resulting magnetization in dependency of the pulse duration

- $w = M_x/M_0$

$$\begin{aligned} A &= 0 \\ B &= \frac{\beta}{1 + \beta^2 + \delta^2} \\ C &= -m_0 + \frac{\beta^2}{1 + \beta^2 + \delta^2} \\ D &= -\frac{\beta}{1 + \beta^2 + \delta^2} \end{aligned} \quad (4.30)$$

- $w = M_y/M_0$

$$\begin{aligned}
A &= -\frac{\delta(1-m_0)}{1+\delta^2} \\
B &= \frac{\delta}{1+\delta^2} \left(\frac{\beta^2}{1+\beta^2+\delta^2} - m_0 \right) \\
C &= -\frac{\delta\beta}{1+\beta^2+\delta^2} \\
D &= \frac{\delta}{1+\beta^2+\delta^2}
\end{aligned} \tag{4.31}$$

- $w = M_z/M_0$

$$\begin{aligned}
A &= \frac{\beta^2 + \delta^2}{1 + \beta^2 + \delta^2} \\
B &= \frac{m_0 - \frac{\beta^2}{1+\beta^2+\delta^2}}{1 + \delta^2} \\
C &= \frac{\beta}{1 + \beta^2 + \delta^2} \\
D &= \frac{\beta^2 + \delta^2}{1 + \beta^2 + \delta^2}.
\end{aligned} \tag{4.32}$$

All components therefore show an individual evolution in time. From the above equations directly evolves that the in-phase component M_x is only slightly influenced by the frequency offset, whereas it has much more significant impact on the out-of-phase component M_y . In fact, for perfect resonance M_y vanishes and the precession in the laboratory frame becomes perfectly real valued. The temporal evolution for all components is a damped harmonic oscillation that does not vanish for long pulse times but approaches a constant value. It converges towards the steady state solution of the Bloch equations. The damping of these oscillations depends on the exponential factors of the terms of A , B and C . For values of $a, b > 0$ the oscillation approaches the aperiodic case where the oscillation is damped within one period. For relaxation constants of $T = 0.1s$ and a static magnetic field strength of $H_0 = 45000nT$ this case appears at secondary field values of $H_1 \frac{1}{1000}H_0$. For the loop magnetic fields in MRS that quickly decay from the source, strongly damped oscillations are expected and have to be considered in the forward modeling.

The effect of the variation of the respective parameters is quite complex. To give an overview of the impact of the parameters frequency offset, damping during the pulse and magnetic field ratio, I demonstrate the effect on a unit magnetization and change one parameter a time in the range that could appear in MRS applications. In figure 4.3 the transient evolution is shown for a 1.5 second pulse to demonstrate the effective damping for long times. For the assessment of the influence in MRS in figures 4.4, 4.5, 4.6, the

4. The nuclear Spin in magnetic fields

pulse length is set to 0.1 s. Standard pulse length in field measurements is 0.04s, currently maximum pulse length is 0.08s.

Figure (4.4) shows the influence of the magnitude of the exciting field on the transient magnetization evolution. The function generally shows a decay in magnitude in this time interval, but the amount of attenuation decreases at equal relaxation constants, the weaker the exciting field is. The effect of frequency deviation, as visible from figure (4.5), leads to a shortening of oscillation wavelength with increasing frequency offset. Additionally the out-of-phase component reaches significant magnitudes. The out-of-phase component has also a larger steady-state component, it doesn't converge to zero, but to a value of approximately -0.5. Consequently the phase lag of the induced magnetization increases with increasing excitation time. On the other hand, increasing relaxation constants effects the in-phase component more than the out-of-phase component as visible for the relaxation constant range in figure (4.6). The effect of the relaxation constant, however gains important influence for the studied range of 500 to 50ms and the given parameters in figure (4.6). The magnitude of the induced magnetization can be attenuated during the excitation by up to 50% at a pulse duration 40ms and a relaxation constant of 50ms. The given exemplary study on the influence of the magnitude and phase lag of the induced magnetization clearly demonstrates its importance in MRS applications. In the range of parameters as they occur in a common sounding, the complex transient evolution have an important impact on the measured signal. Especially the development of a M_y component of the magnetization that appears as soon as the resonance frequency is not perfectly met is of interest. The components M_x , M_y and M_z are in respect to the coordinates of the rotating frame, i.e. rotating with the Spin around its precession axis. Transformation back into the laboratory frame, the M_x component represents the real-part of the magnetization, M_y the imaginary part. This clearly demonstrates the evolution of a complex valued nuclear magnetization in case of frequency deflections between resonance frequency and frequency of the pulse. Consequently the recorded MRS signal accounts a phase lag that originates from the Nuclear Magnetic Resonance phenomenon itself.

4.4. Parameters of the Bloch equation in MRS applications

The contributing parameters, assessed above, vary in space and time of a sounding. These variations are quantified in the following to estimate their influence on the complex MRS response signal.

4.4.1. Spatial distribution of the loop field

The electromagnetic field for MRS applications is generated by an antenna loop sitting on the surface. Figure 4.7 shows the magnetic field distribution of a 100m loop at a pulse

4.4. Parameters of the Bloch equation in MRS applications

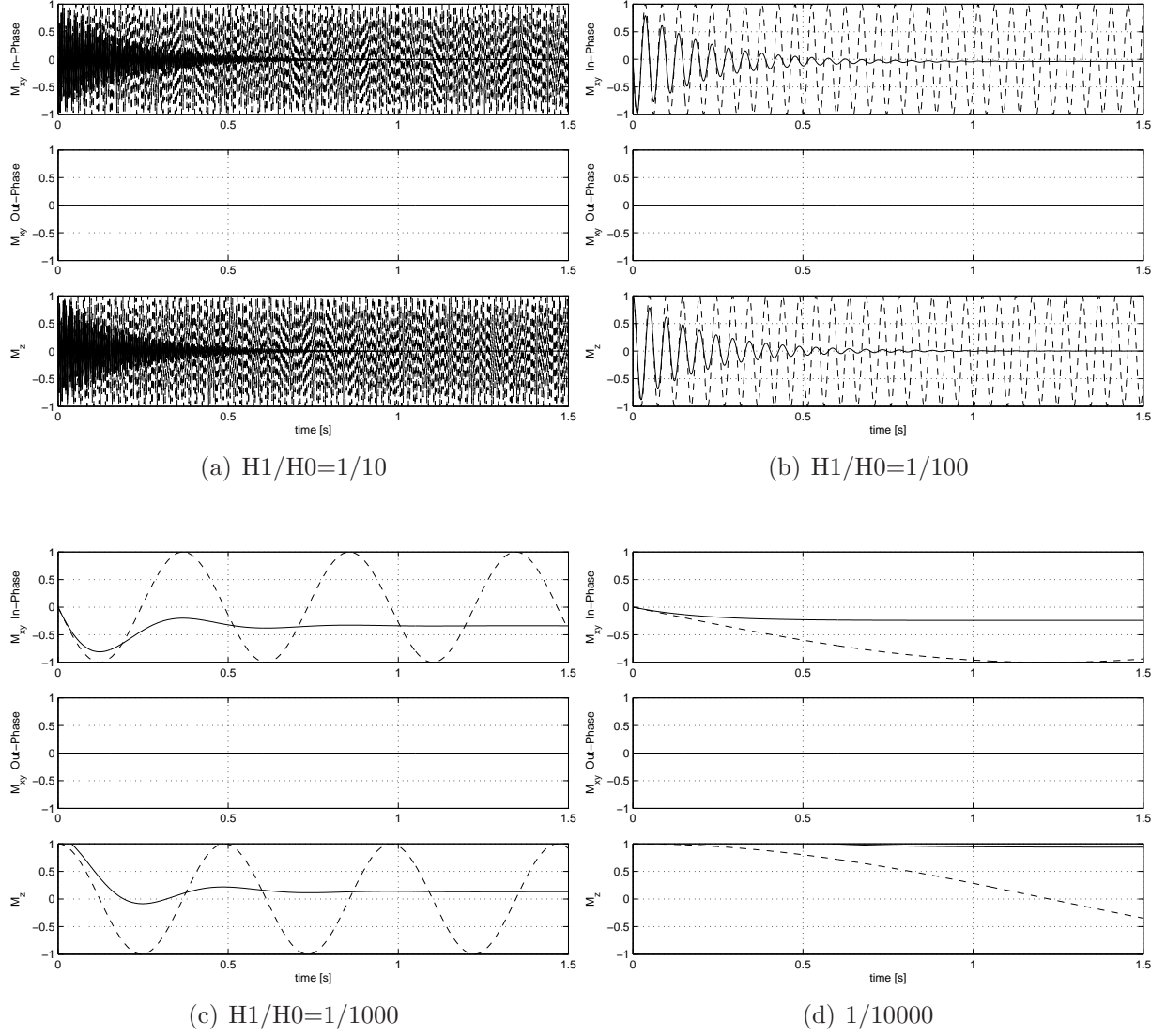


Figure 4.3.: Transient nutation of the components of the nuclear magnetization in dependency of the magnitude of the secondary field (solid) and the undamped oscillation (dashed). $\tau_p = 1.5s$, $\Delta\omega = 0$, $T_R = 0.2s$, $H_1 = \frac{1}{10}, \frac{1}{100}, \frac{1}{1000}, \frac{1}{10000}H_0$

4. The nuclear Spin in magnetic fields

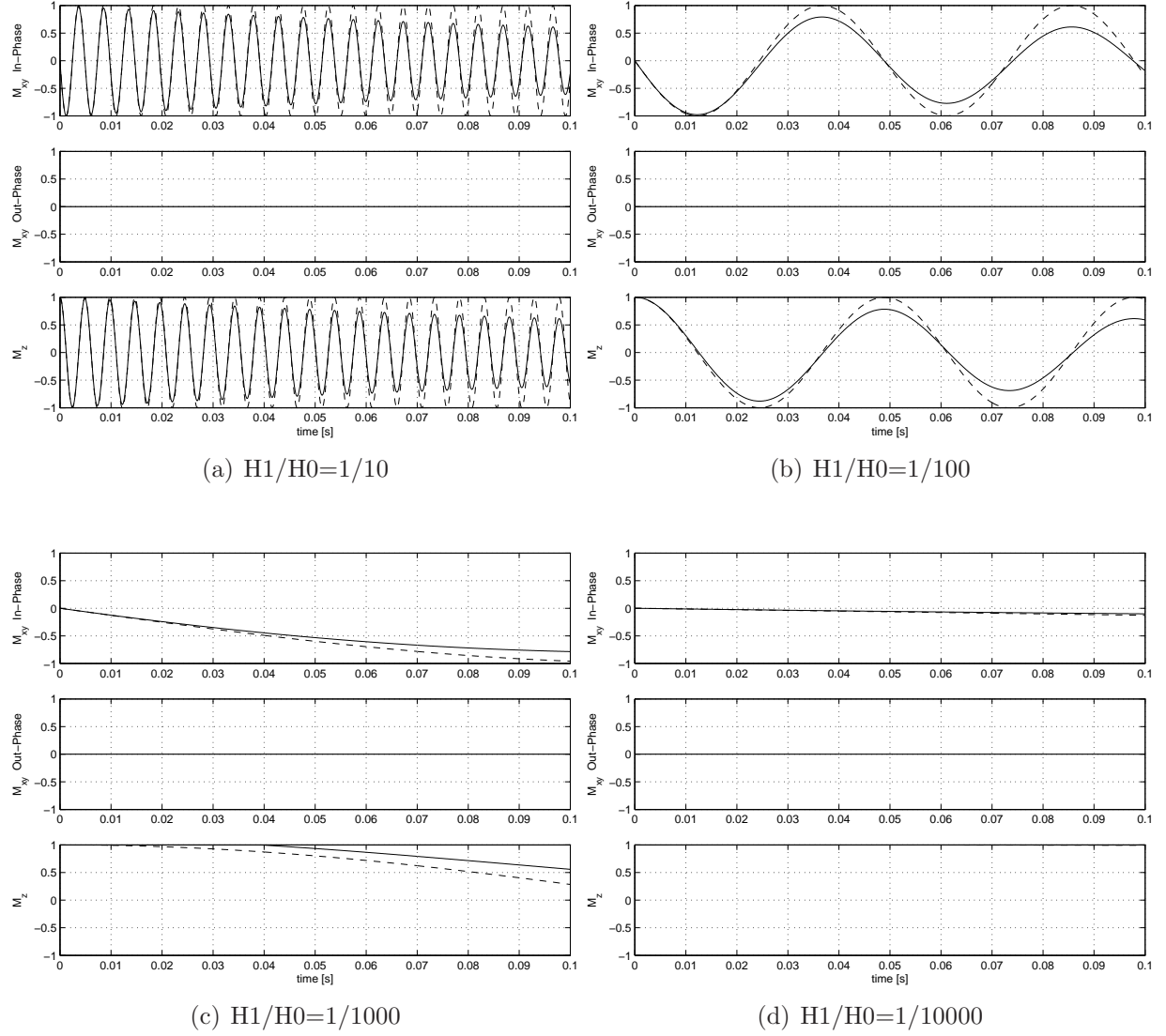


Figure 4.4.: Transient nutation of the components of the nuclear magnetization with the same parameters than figure (4.3) but displayed for the section up to 0.1s.

4.4. Parameters of the Bloch equation in MRS applications

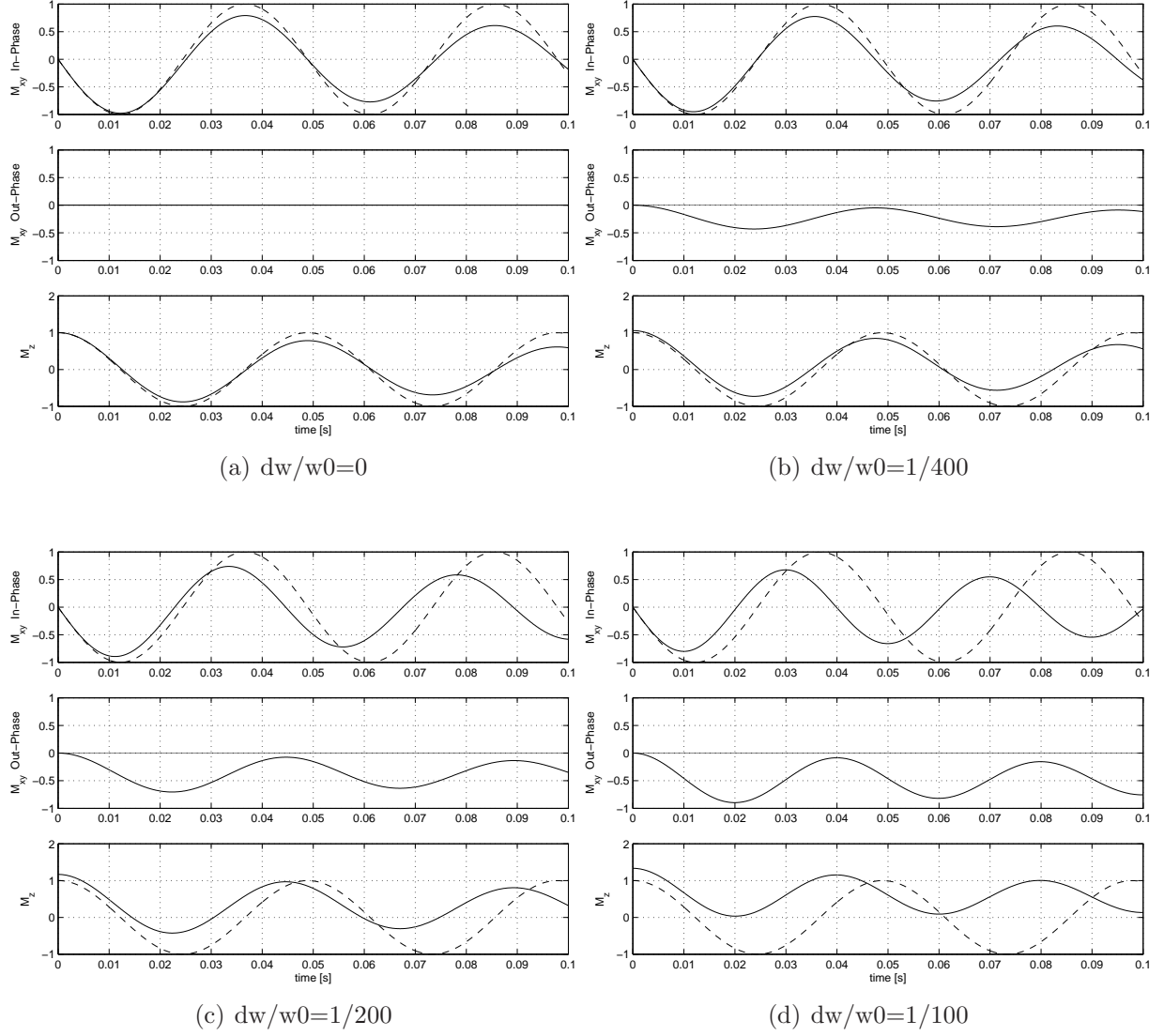


Figure 4.5.: Transient nutation of the components of the nuclear magnetization in dependency of the magnitude of the frequency offset (solid) and the undamped oscillation (dashed). $\tau_p = 0.1s$, $\Delta\omega = 0$, $\frac{1}{400}$, $\frac{1}{200}$, $\frac{1}{100}\omega_0$, $T_R = 0.2s$, $H_1 = \frac{1}{100}H_0$

4. The nuclear Spin in magnetic fields

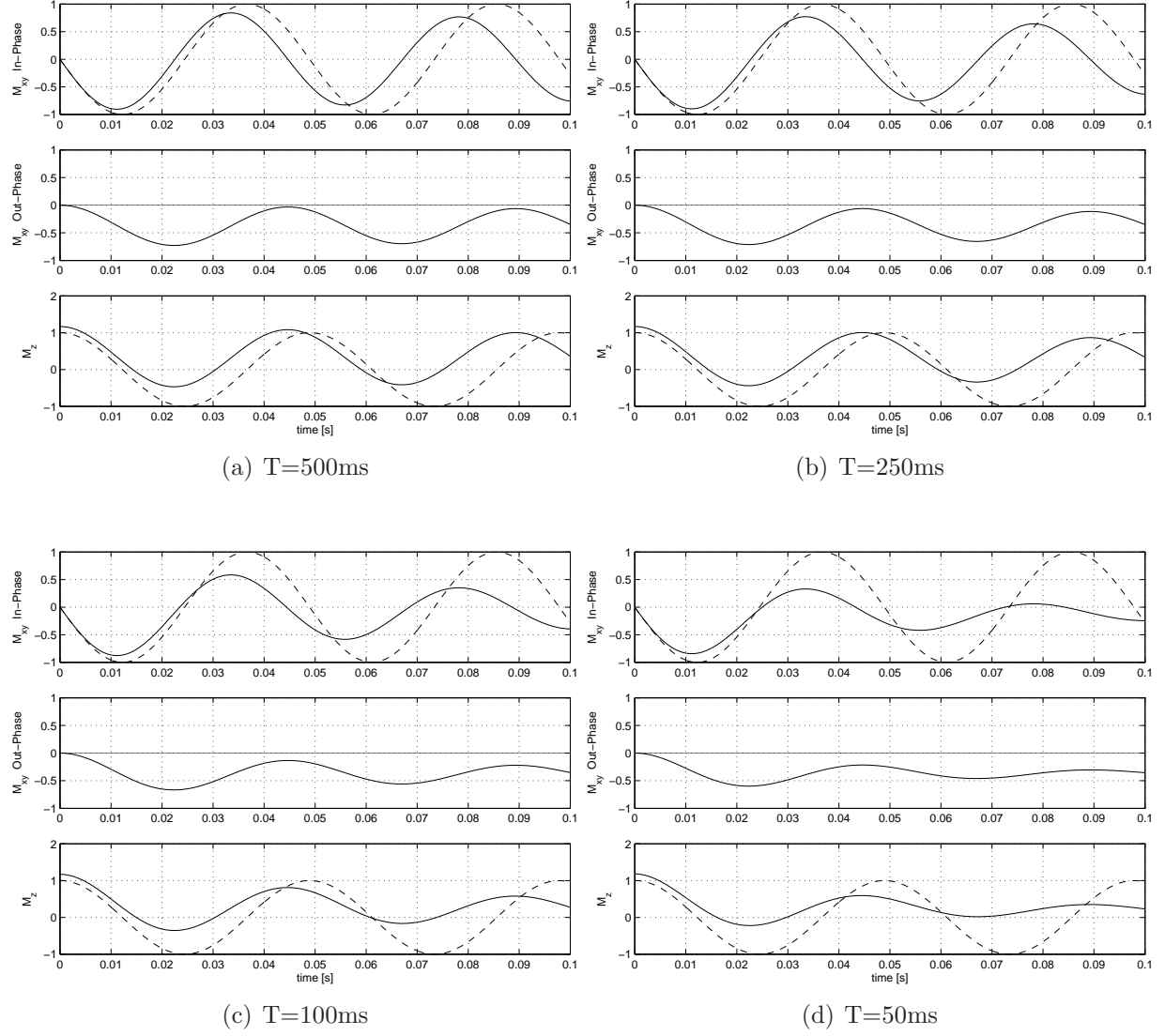


Figure 4.6.: Transient nutation of the components of the nuclear magnetization in dependency of the magnitude of the secondary field (solid) and the undamped oscillation (dashed). $T\tau_p = 0.1s$, $\Delta\omega = \frac{1}{200}\omega_0$, $T_R = 0.5s, 0.25s, 0.1s, 0.05s$, $H_1 = \frac{1}{100}H_0$

4.4. Parameters of the Bloch equation in MRS applications

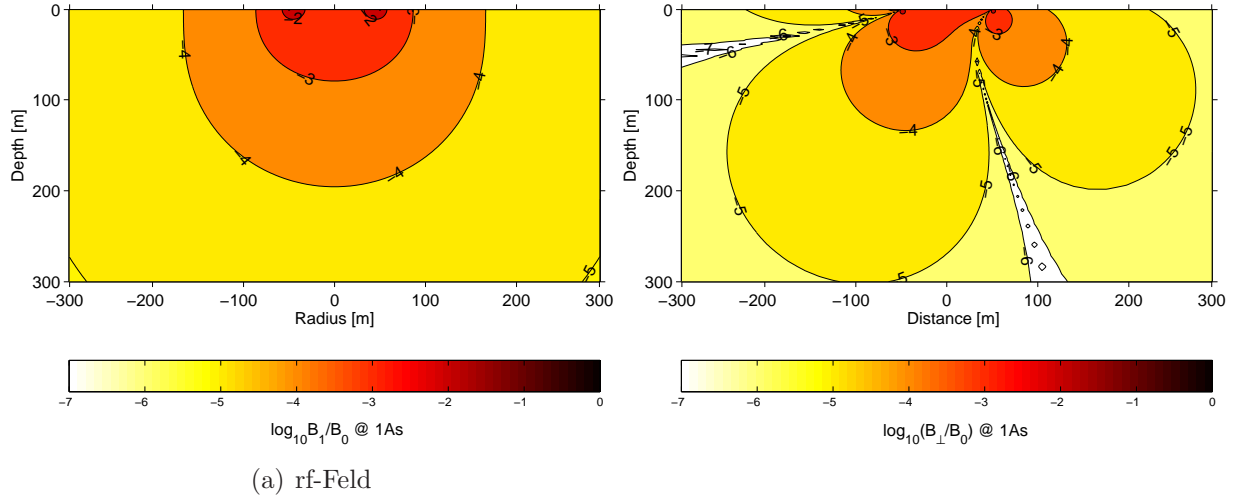


Figure 4.7.: Spatial distribution of (a) the magnitude of a wire loop of 100m diameter, 1 turn normalized to the Earth's field of $48000nT$. (b) the effectively acting component perpendicular to the Earth's field direction as a south-north section.

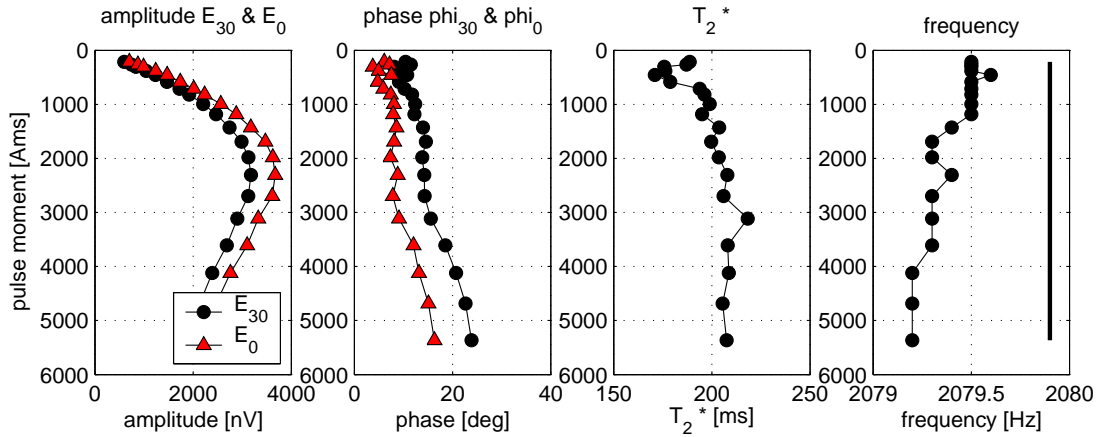
moment of $1As$, corresponding to a current of $25A$, as a depth section through the loop center. Its magnitude decays approximately semi-spherical. This decay is mainly due to geometrical spreading and less due to electromagnetic attenuation (see section 2.2). The magnitude of the loop field in the subsurface is in a range of about $10^{-2} - 10^{-3}$ of the Earth field (Fig. 4.7). The component perpendicular to the Earth's field direction that effectively acts on the Spin is even one order smaller (see Fig. 4.7 b)). The Spin remote from the loop are therefore even at strong pulses with currents up to $300A$ only slowly deflected and relaxation influence in the magnitude range of the exciting field has to be taken into account for the magnetization evolution during the pulse.

4.4.2. Temporal variation of the Earth's field

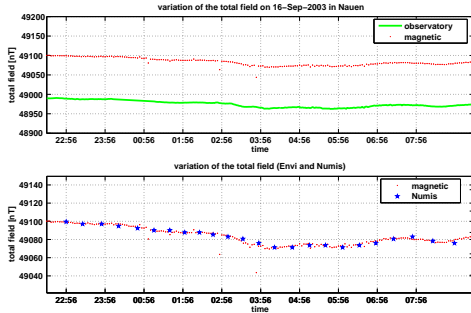
The deviation of the loop field frequency compared to the resonance frequency of the Spins has significant influence on the MRS signal imaginary part but only slight impact on the real part. Since the imaginary part is usually much smaller than the real part, the amplitude is only slightly influenced, whereas significant phase variation appear. Most MRS measurements show a mirror symmetric phase and frequency curvature, i.e figure 4.8 a). From the total recorded signal the derived parameters of phase and frequency are often affected by large errors in case of poor data quality. For a correct consideration of the phase deflection it is useful to incorporate external magnetic data from a nearby magnetometer and compare the data to the nearest magnetic observatory (www.intermagnet.org). The absolute phase deflection for each sub-volume depends on the settings of the other influencing parameters magnetic field ratio and relaxation constant. Since the MRS signal is

4. The nuclear Spin in magnetic fields

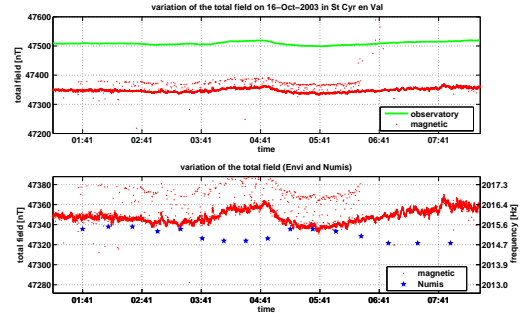
the integral over a volume where the parameters vary significantly, full spin dynamics have to be taken into account for a known frequency deviation. A simple linear correction of the integral measured phase by the frequency deflection is not valid. Fig. 4.8b) and c) show examples of two MRS measurements with accompanying magnetic measurements and the respective recordings from the nearest magnetic observatory. The first example shows a good accordance between Larmor frequencies determined by MRS data processing and external magnetic field measurements, the second example shows significant deviations. Here a post-processing of the data with the magnetic field data as a priori information is recommended.



(a) exemplary MRS sounding



(b) proper Numis determined frequency



(c) improper Numis determined frequency

Figure 4.8.: (a) Typical curvature of a MRS measurement in amplitude, phase, decay constant and frequency (x-coordinate) in dependency of the pulse-moment q (y-coordinate). (b) Variation of the Earth's magnetic field during a MRS measurement determined by a magnetic observatory, a nearby magnetometer and the NUMIS device with a perfect correlation of NUMIS determined static magnetic field magnitudes, i.e. Larmor frequencies, c) another MRS measurement with significant deviations.

4.4.3. Relaxation constants

From the assessment in Chapter 4.2 we know that the relaxation constant determines the attenuation of the magnetic field components during the pulse. To correctly implement the relaxation constant distribution into the calculation of an appropriate forward modeling, it must be known prior to its consideration in an appropriate modeling. But the information about the relaxation constant distribution is the result of an inversion of the MRS measurement. For this inversion a forward modeling is necessary. There is no way to derive the relaxation constant distribution from other sources as it is possible for the magnetic field variations or electrical conductivity distribution which are implemented from complementary geophysical measurements. To work around one can use the apparent relaxation constant from the MRS signal. This value is in general the integral value over the entire half-space. However, we know that at a single pulse moment the major part of the signal appears to evolve from a confined depth. Assigning this value for the considered pulse moment to the entire half-space is obviously an approximation, but the variation of relaxation constant is usually moderate and, finally, this is the only available information. If a more accurate estimation of relaxation constant distribution from the soundings is necessary, an iterative solution with updated T -times should be implemented. Even more impact has the effect of attenuation during the pulse if we assume multi-exponential decay within one layer or structure. In this case the solution would become highly nonlinear.

4.5. Interpretation

I have shown that the mathematical solution of the Spin magnetization for large scale applications in the Earth's field range has to be treated in a more general way than for most other NMR applications. The variation of parameters as found in MRS investigations generally leads to a complex valued and attenuated evolution of the Spin magnetization during the pulse. So, the Spin magnetization itself has a phase lag in respect to the exciting field in dependency of the measurement conditions. The observed phase is thus of quantum mechanical origin and so referred to in the course of this thesis. Numerous modeling has been performed to adequately fit the measured complex MRS signal by considering quantum mechanical phase effects in addition to the electromagnetic phase. A qualitative correlation is observed, but the fit of modeled and observed phases is still insufficient (Hertrich and Yaramanci, 2003a). The influence of the pulse shape, causing a broadened frequency spectrum of the pulse, is considered by Legchenko (2004). Using this extended formulation, an enhancement in complex sounding data fitting is achieved in some cases, but a large number of soundings can still not be appropriately fitted. The quadrature component of the signal is in most cases quite small, and the amplitude of the signal is hardly effected. So inversion results of the signal amplitude can be assumed to be a suitable approximation.

4. *The nuclear Spin in magnetic fields*

5. The MRS response signal

5.1. Basic MRS formulation

In the description of the MRS signal as it is recorded in soundings with separated transmitter and receiver loops, the elliptical parameterization of the magnetic field as introduced by Weichman et al. (2000) is used. Starting the analysis with the time dependent voltage V_R , induced in the receiver loop due to a magnetic flux emitted from a perturbed Spin ensemble with magnetic moment M_N , yields after Weichman et al. (2000, eq. 2.22)

$$V_R(t) = \int d^3\mathbf{r} \int_0^\infty dt' \mathcal{B}_R(\mathbf{r}, t) \cdot \partial_t \mathbf{M}_N(\mathbf{r}, t - t'), \quad (5.1)$$

where \mathcal{B}_R denotes a virtual magnetic field arising from a unit current pulse in the receiver loop. To evaluate the interaction of the Spin magnetization and the exciting fields of the transmitter and the response from the Spin magnetic field to the receiver, a detailed description of the properties of the induced magnetic fields of surface loops in the subsurface is necessary.

The monochromatic electromagnetic field \mathbf{B} can be formally decomposed into two complex vector fields $\mathcal{B}_{1,2}$, oscillating with Larmor angular frequency $\omega_L = -\gamma_p |\mathbf{B}_0|$ with \mathbf{B}_0 the Earth's field vector and γ_p the gyromagnetic ratio of Hydrogen nuclei ($^1H^+$), linking the Spin precession frequency to the static field strength. Then,

$$\begin{aligned} \mathbf{B}(t) &= \frac{1}{2} I^0 [\mathcal{B}(\omega_L) e^{-i(\omega_L t)} + \mathcal{B}(-\omega_L) e^{i(\omega_L t)}] \\ &= I^0 [\mathcal{B}_1(\omega_L) \cos(\omega_L t) + \mathcal{B}_2(\omega_L) \sin(\omega_L t)], \end{aligned} \quad (5.2)$$

where \mathcal{B}_1 and \mathcal{B}_2 are in general non-collinear, corresponding to an elliptically polarized vector field and I^0 is the corresponding current in the loop inducing the magnetic field.

The orientation of an inhomogeneous magnetic field, e.g. the vector field of a dipole source, varies rapidly in space, whereas the direction of the magnetic moment of the nuclear Spin system, in equilibrium oriented along the Earth's magnetic field \mathbf{B}_0 , is assumed to be constant within the investigation volume. In its interaction with the nuclear Spin system, only the component of the excitation field perpendicular to it, \mathbf{B}^\perp , is physically acting. The projection of the magnetic field into the plane perpendicular to \mathbf{B}_0 is given by

$$\mathbf{B}^\perp(\mathbf{r}) = \mathbf{B}(\mathbf{r}) - (\hat{\mathbf{b}}_0 \cdot \mathbf{B}(\mathbf{r})) \hat{\mathbf{b}}_0, \quad (5.3)$$

5. The MRS response signal

where the following identities for the magnitudes and directions of the vector fields are used:

$$\begin{aligned}\mathbf{B} &= B\hat{\mathbf{b}} \\ \mathbf{B}_0 &= B_0\hat{\mathbf{b}}_0 \\ \mathbf{B}^\perp &= B^\perp\hat{\mathbf{b}}^\perp.\end{aligned}\tag{5.4}$$

In case of an elliptically polarized excitation field, generally valid in conductive media, its perpendicular projection \mathbf{B}^\perp is also elliptically polarized unless \mathbf{B}_0 lies in the ellipse plane of \mathbf{B} . For a radial symmetric vertical magnetic dipole source, this is the case in declination direction of the static field and direction independent for vertical inclination, i.e. at the poles. Using equation. 5.2 the projected elliptical field is decomposed into two circular rotating parts with spinning sense clockwise and counterclockwise, i.e.,

$$\begin{aligned}\mathbf{B}^\perp(t) &= \mathbf{B}^+(t) + \mathbf{B}^-(t) \\ &= I^0 \left[\alpha \cos(\omega_L t - \zeta) \hat{\mathbf{b}}^\perp + \beta \sin(\omega_L t - \zeta) \hat{\mathbf{b}}_0 \times \hat{\mathbf{b}}^\perp \right].\end{aligned}\tag{5.5}$$

Here α and β are the major and minor axes of the ellipse and ζ is chosen in such a way, that α and β are real. \mathbf{B}^+ and \mathbf{B}^- are the circular polarized components of the elliptically polarized vector \mathbf{B}^\perp . They are rotating clockwise and counterclockwise in respect to the Earth's field direction $\hat{\mathbf{b}}_0$. Concerning the spinning sense of hydrogen nuclei clockwise around the static field they are referred to as co- and counter-rotating parts in the course of the discussion, respectively. For the complex field amplitudes consequently follows

$$\mathcal{B}^\perp(\omega_L) = e^{i\zeta(\omega_L)} \left[\alpha(\omega_L) \hat{\mathbf{b}}^\perp(\omega_L) + i\beta(\omega_L) \hat{\mathbf{b}}_0 \times \hat{\mathbf{b}}^\perp(\omega_L) \right].\tag{5.6}$$

The circular rotating parts of the perpendicular component \mathbf{B}^\perp can then be rewritten as

$$\mathbf{B}^\pm(t) = \frac{1}{2}I^0(\alpha \mp \beta) \left[\cos(\omega t - \zeta) \hat{\mathbf{b}}^\perp \mp \sin(\omega_L t - \zeta) \hat{\mathbf{b}}_0 \times \hat{\mathbf{b}}^\perp \right]\tag{5.7}$$

$$= \frac{1}{2}I^0 \left[\mathcal{B}^\pm(\mathbf{r}, \omega_L) e^{-i(\omega_L t)} + \mathcal{B}^\pm(\mathbf{r}, -\omega_L) e^{i(\omega_L t)} \right]\tag{5.8}$$

$$= \frac{1}{2}I^0 \left[\mathcal{B}^\pm(\mathbf{r}, \omega_L) e^{-i(\omega_L t)} + c.c. \right],\tag{5.9}$$

where *c. c.* denotes the complex conjugate of the former expression. The co- and counter-rotating parts are described by their magnitudes

$$|\mathbf{B}^\pm| = \frac{1}{2}I^0(\alpha \mp \beta).\tag{5.10}$$

and their unit direction vectors

$$\begin{aligned}\widehat{\mathbf{b}}^\pm &= \frac{\mathbf{B}^\pm}{|\mathbf{B}^\pm|} \\ &= e^{-i(\omega_L t - \zeta)} \left[\widehat{\mathbf{b}}^\perp \mp i \widehat{\mathbf{b}}_0 \times \widehat{\mathbf{b}}^\perp \right] + c.c.\end{aligned}\quad (5.11)$$

respectively. Since the resulting magnetization of the Spin ensemble is oriented in equilibrium along the static field \mathbf{B}_0 , an exciting force of a monochromatic field in direction $\widehat{\mathbf{b}}_T^\perp(\mathbf{r})$ will force it on a precessional motion in the plane spanned by the $\widehat{\mathbf{b}}_T^\perp(\mathbf{r})$ and $\widehat{\mathbf{b}}_0 \times \widehat{\mathbf{b}}_T^\perp(\mathbf{r})$. Its oscillation can be described in its spatial components as

$$\begin{aligned}\mathbf{M}_N(t) &= M_N^{(0)} \left\{ \mathcal{M}_\parallel \widehat{\mathbf{B}}_0 + \right. \\ &\quad \left. \mathcal{M}_\perp \left[\widehat{\mathbf{b}}_0 \times \widehat{\mathbf{b}}_T^\perp \cos(\omega_L t - \zeta_T) + \widehat{\mathbf{b}}_T^\perp \sin(\omega_L t - \zeta_T) \right] \right\}.\end{aligned}\quad (5.12)$$

where \mathcal{M}_\parallel and \mathcal{M}_\perp are the components of the magnetic moment oriented in direction of the static field $\widehat{\mathbf{B}}_0$ and perpendicular to it, respectively. It is only the component \mathcal{M}_\perp normal to $\widehat{\mathbf{B}}_0$ that oscillates and consequently emits an electromagnetic signal. The temporal derivative of $\mathbf{M}_N(\mathbf{r}, t)$ as it enters equation (5.1) yields

$$\begin{aligned}\partial_t \mathbf{M}_N(\mathbf{r}, t) &= M_N^0(\mathbf{r}) \omega_L \mathcal{M}_\perp \\ &\quad \times \left[-\widehat{\mathbf{b}}_0 \times \widehat{\mathbf{b}}_T^\perp(\mathbf{r}) \sin(\omega_L t - \zeta_T) + \widehat{\mathbf{b}}_T^\perp(\mathbf{r}) \cos(\omega_L t - \zeta_T) \right],\end{aligned}\quad (5.13)$$

where only the oscillating part contributes. Equation (5.13) can be easily identified as the unit co-rotating part of the transmitter in equation (5.11). So we can simplify equation (5.13) to

$$\partial_t \mathbf{M}_N(\mathbf{r}, t) = M_N^0(\mathbf{r}) \omega_L \mathcal{M}_\perp \widehat{\mathbf{b}}_T^+(\mathbf{r}, t). \quad (5.14)$$

This explicitly demonstrates that the Spin magnetization \mathbf{M}_N , achieved by the co-rotating part of the tipping pulse, oscillates in a fixed direction and phase relation with the source field. Substituting equation (5.1) and equation (5.14) into the equation for the voltage response in the receiver loop (5.1) yields

$$V_R(t) = \int d^3r M_N^{(0)} \int_0^\infty dt' \mathcal{B}_R(\mathbf{r}, t) \omega_L \mathcal{M}_\perp \widehat{\mathbf{b}}_T^+(\mathbf{r}, t - t'), \quad (5.15)$$

5. The MRS response signal

or with the complex notation of the transmitter field component from equation (5.11)

$$V_R(t) = \omega_L \int d^3r M_N^0 \int_0^\infty dt' \mathcal{B}_R(\mathbf{r}, t') \mathcal{M}_\perp \times \left[e^{-i(\omega_L(t-t')-\zeta_T)} \left(\hat{\mathbf{b}}_T^\perp - i\hat{\mathbf{b}}_0 \times \hat{\mathbf{b}}_T^\perp \right) + c. c. \right] \quad (5.16)$$

$$= \omega_L \int d^3r M_N^0 \mathcal{M}_\perp e^{-i(\omega_L t - \zeta_T)} \left(\hat{\mathbf{b}}_T^\perp - i\hat{\mathbf{b}}_0 \times \hat{\mathbf{b}}_T^\perp \right) \times \left[\int_0^\infty dt' \mathcal{B}_R(\mathbf{r}, t') e^{i\omega_L t'} + c. c. \right]. \quad (5.17)$$

The integral in the second line simply represents a Fourier-integral, transforming the causal time dependent field amplitude $\mathcal{B}_R(r, t')$ into a frequency dependent one $\mathcal{B}_R(r, \omega_L)$, so that the expression changes into

$$V_R(t) = \omega_L \int d^3r M_N^0 \mathcal{M}_\perp \left(\hat{\mathbf{b}}_T^\perp - i\hat{\mathbf{b}}_0 \times \hat{\mathbf{b}}_T^\perp \right) e^{-i(\omega t + \varphi - \zeta_T)} \mathcal{B}_R(\mathbf{r}, \omega_L) + c. c. \quad (5.18)$$

The vector \mathcal{B}_R is here multiplied with the direction vectors of the plane normal to \mathbf{B}_0 , so that all components \mathcal{B}_R parallel to \mathbf{B}_0 vanish and only the perpendicular component of \mathcal{B}_R physically acts. \mathcal{B}_R can be conveniently replaced by \mathcal{B}_R^\perp , and with equation (5.6), equation (5.18) changes into

$$V_R(t) = \omega_L \int d^3r M_N^0 \mathcal{M}_\perp \times e^{i\zeta_T(\mathbf{r}, \omega_L)} \left[\hat{\mathbf{b}}_T^\perp(\mathbf{r}, \omega_L) - i\hat{\mathbf{b}}_0 \times \hat{\mathbf{b}}_T^\perp(\mathbf{r}, \omega_L) \right] e^{-i(\omega t + \varphi)} \times e^{i\zeta_R(\mathbf{r}, \omega_L)} \left[\alpha_R(\mathbf{r}, \omega_L) \hat{\mathbf{b}}_T^\perp(\mathbf{r}, \omega_L) + i\beta_R(\mathbf{r}, \omega_L) \hat{\mathbf{b}}_0 \times \hat{\mathbf{b}}_T^\perp(\mathbf{r}, \omega_L) \right] + c. c. \quad (5.19)$$

Commonly only the positive envelope of the signal is recorded by quadrature detection in respect to a reference frequency (Legchenko and Valla, 1998). Thereby the oscillations at Larmor frequency are removed and the signal simplifies to its real envelope without the complex conjugate part:

$$V_R(t) = \omega_L \int d^3r M_N^0 \mathcal{M}_\perp \times e^{i\zeta_T(\mathbf{r}, \omega_L)} \left[\hat{\mathbf{b}}_T^\perp(\mathbf{r}, \omega_L) - i\hat{\mathbf{b}}_0 \times \hat{\mathbf{b}}_T^\perp(\mathbf{r}, \omega_L) \right] \times e^{i\zeta_R(\mathbf{r}, \omega_L)} \left[\alpha_R(\mathbf{r}, \omega_L) \hat{\mathbf{b}}_R^\perp(\mathbf{r}, \omega_L) + i\beta_R(\mathbf{r}, \omega_L) \hat{\mathbf{b}}_0 \times \hat{\mathbf{b}}_R^\perp(\mathbf{r}, \omega_L) \right]. \quad (5.20)$$

By solving the multiplications and rearrangement of the terms, equation (5.20) can be

rewritten as

$$\begin{aligned}
 V_R(t) = & \omega_L \int d^3r M_N^0 \mathcal{M}_\perp \\
 & \times [\alpha_R(\mathbf{r}, \omega_L) + \beta_R(\mathbf{r}, \omega_L)] \cdot e^{i[\zeta_T(\mathbf{r}, \omega_L) + \zeta_R(\mathbf{r}, \omega_L)]} \\
 & \times \left[\hat{\mathbf{b}}_R(\mathbf{r}, \omega_L) \cdot \hat{\mathbf{b}}_T(\mathbf{r}, \omega_L) + i\hat{\mathbf{b}}_0 \cdot \hat{\mathbf{b}}_R(\mathbf{r}, \omega_L) \times \hat{\mathbf{b}}_T(\mathbf{r}, \omega_L) \right]. \quad (5.21)
 \end{aligned}$$

Here, the magnitude of the perpendicular magnetization \mathcal{M}_\perp is equal to excitation angle of the precessing Spin system. The perpendicular magnetization is in general complex valued and depends on the exciting pulse properties as discussed in chapter 4. For the following discussion the adiabatic approximation for the Spin perturbation will be used (Abragam, 1983). With the co-rotating part of the loop field as tipping field it is given by

$$\mathcal{M}_\perp = \mathbf{M}_N^{(0)} \sin(\Theta_T) = \mathbf{M}_N^{(0)} \sin\left(-\gamma \frac{q}{I_0} |\mathbf{B}_T^+(\mathbf{r})|\right), \quad (5.22)$$

where q is the product of the current amplitude through the transmitter loop I_0 and τ_p is the duration of the pulse. The expression in brackets in the second line of equation (5.21) can be identified as the absolute value of the counter-rotating part of the receiver field according equation (5.7). With these identities the formula for the induced voltage in the receiver loop is finally given by

$$\begin{aligned}
 V_R(t) = & \omega_L \int d^3r \mathbf{M}_N^{(0)} \sin\left(-\gamma \frac{q}{I_0} |\mathbf{B}_T^+(\mathbf{r})|\right) \\
 & \times \frac{2}{I_0} |\mathbf{B}_R^-(\mathbf{r})| \cdot e^{i[\zeta_T(\mathbf{r}, \omega_L) + \zeta_R(\mathbf{r}, \omega_L)]} \\
 & \times \left[\hat{\mathbf{b}}_R^\perp(\mathbf{r}, \omega_L) \cdot \hat{\mathbf{b}}_T^\perp(\mathbf{r}, \omega_L) + i\hat{\mathbf{b}}_0 \cdot \hat{\mathbf{b}}_R^\perp(\mathbf{r}, \omega_L) \times \hat{\mathbf{b}}_T^\perp(\mathbf{r}, \omega_L) \right]. \quad (5.23)
 \end{aligned}$$

The given derivation of the MRS formula describes how the magnetic field components of transmitter and receiver loop differently determine the basic MRS response signal. The fact that the counter-rotating part of the receiver field enters the equation evolves from the reciprocity of mutual induction between the loop and the Spin magnetization. The absolute value of the induction from a loop to a microscopic magnetization in the subsurface and vice versa is equal. But the induction reverse from the microscopic magnetization back to the loop can be regarded to be backwards in time and therefore causing the inverse components of the exciting fields to take effect. In the given notation the relative orientation of transmitter and receiver fields and their orientation in the Earth's field is taken into account. It scales the complex MRS response and gives rise to an additional geometric phase.

Equation (5.23) describes the induced voltage in the receiver loop as a volume integral of a functional depending on the different magnetic field components of loop and Spin magnetic fields in dependency of distance vector \mathbf{r} . In this form the accounting terms of the equation

5. The MRS response signal

can be physically interpreted as follows:

- The first line of the equation gives the signal amplitude of a Spin system, emitting the NMR response. It consists of the magnitude of the magnetization vector, i.e. the number of Hydrogen nuclei, and the excitation angle they have achieved by the energizing pulse. The excitation angles of the resulting magnetization is a harmonic function, determined by the normalized amplitude of the co-rotating part of the transmitter field and the pulse moment q .
- The second line describes the sensitivity of the receiver to a signal in the subsurface. This spatial sensitivity is independent from signal generation, i.e. the pulse moment. It is simply given by the magnetic field distribution associated to the receiver loop. Additionally the signal undergoes a phase lag from the transmitter to the sample and from the sample to the receiver due to electromagnetic attenuation.
- The most important part in the treatment of the mathematical foundation of separated loop configuration is shown in the third line. Whereas the first two lines only cover the scalar values of excited signals and their associated induced voltage in the loop, this part accounts the vectorial nature of the evolution of the MRS signal. The expression in the bracket describes the dependency of the evolving signal on the directions of transmitter and receiver field and their orientation in respect to the Earth's field. Note, that only the unit direction vectors of the magnetic fields enter this part of the function. The first part of the sum, the real part of the whole bracket, is simply a scalar vector multiplication, whereas the second, the vector product of both fields and their scalar product with the Earth's field, scales the imaginary part of the expression. In case of coincident loop soundings, the latter part vanishes whereas the former one approaches unity; the complete expression becomes a real unity value. For all other loop layouts the value of this last term, the geometric term, scales the NMR effect and the signal response by a value in the range $[-1, 1]$; $[-i, i]$. Consequently, the evolving signal for separated loops is in general complex valued. The resulting phase shift of the recorded signals is the geometrical phase of the MRS signal. It acts in addition to the quantum mechanical phase due to frequency deviations (Hertrich and Yaramanci, 2003a) and frequency spectra of the pulse (Legchenko, 2004) and the electromagnetic phase lag caused by signal propagation in conductive media.

5.2. Synthetic data

The derivation of the general formulation of the recorded response signal voltage in the previous chapter was done for general 3D conditions. Substituting the magnitude of the

5.2. Synthetic data

macroscopic magnetization at any point $\mathbf{M}_N^{(0)}(\mathbf{r})$ by the product of the specific magnetization of water $M_N^{(0)}$ and the amount of water $f(\mathbf{r})$ like

$$\mathbf{M}_N^{(0)}(\mathbf{r}) = M_N^{(0)} f(\mathbf{r})$$

allows to rewrite the basic equation as a function of the water content

$$\begin{aligned} V_R(t) = & \omega_L M_N^{(0)} \int d^3r f(\mathbf{r}) \sin\left(-\gamma \frac{q}{I_0} |\mathbf{B}_T^+(\mathbf{r})|\right) \\ & \times \frac{2}{I_0} |\mathbf{B}_R^-(\mathbf{r})| \cdot e^{i[\zeta_T(\mathbf{r}, \omega_L) + \zeta_R(\mathbf{r}, \omega_L)]} \\ & \times \left[\hat{\mathbf{b}}_R^\perp(\mathbf{r}, \omega_L) \cdot \hat{\mathbf{b}}_T^\perp(\mathbf{r}, \omega_L) + i \hat{\mathbf{b}}_0 \cdot \hat{\mathbf{b}}_R^\perp(\mathbf{r}, \omega_L) \times \hat{\mathbf{b}}_T^\perp(\mathbf{r}, \omega_L) \right]. \end{aligned} \quad (5.24)$$

The water content entering this equation is only part of the total water content in the pore space. Water that is bound to the internal surface or stored in very fine pores does not contribute to the MRS response signal since its relaxation constants are too small to be detected by the MRS technique. The water content contributing to the response signal is thus closely related to the mobile water content. The remaining parameters in the integral of equation 5.24 then describe the constant settings of the measurement as loop shape, Earth's electrical conductivity and choice of pulse moments and are commonly combined to the MRS kernel function

$$V_R(t) = \omega_L M_N^{(0)} \int d^3r f(\mathbf{r}) K(q, \mathbf{r}). \quad (5.25)$$

$$\begin{aligned} K(q, \mathbf{r}) = & \sin\left(-\gamma \frac{q}{I_0} |\mathbf{B}_T^+(\mathbf{r})|\right) \\ & \times \frac{2}{I_0} |\mathbf{B}_R^-(\mathbf{r})| \cdot e^{i[\zeta_T(\mathbf{r}, \omega_L) + \zeta_R(\mathbf{r}, \omega_L)]} \\ & \times \left[\hat{\mathbf{b}}_R^\perp(\mathbf{r}, \omega_L) \cdot \hat{\mathbf{b}}_T^\perp(\mathbf{r}, \omega_L) + i \hat{\mathbf{b}}_0 \cdot \hat{\mathbf{b}}_R^\perp(\mathbf{r}, \omega_L) \times \hat{\mathbf{b}}_T^\perp(\mathbf{r}, \omega_L) \right]. \end{aligned} \quad (5.26)$$

In case of 2D or 1D conditions, the formulation is commonly simplified by reducing the kernel function to the necessary dimension by integrating the general kernel in direction of the respective Cartesian dimension. The expression for 3D is then

$$V_R(t) = \int_0^\infty \int_{-\infty}^\infty \int_{-\infty}^\infty f(x, y, z) \cdot K_{3D}(q; x, y, z) dx dy dz, \quad (5.27)$$

5. The MRS response signal

and can be reduced to 2D as a section in depth and profile direction like

$$\begin{aligned}
 V_R(t) &= \int_0^\infty \int_{-\infty}^\infty f(x, z) \cdot K_{2D}(q; x, z) dx dz \\
 &\text{with} \\
 K_{2D}(q; x, z) &= \int_{-\infty}^\infty K_{3D}(q; x, y, z) dy \\
 \partial f(y) / \partial y &= 0
 \end{aligned} \tag{5.28}$$

or to a map like representation in both lateral directions

$$\begin{aligned}
 V_R(t) &= \int_0^\infty \int_{-\infty}^\infty f(x, y) \cdot K_{2D}(q; x, y) dx dy \\
 &\text{with} \\
 K_{2D}(q; x, y) &= \int_0^\infty K_{3D}(q; x, y, z) dz \\
 \partial f(z) / \partial z &= 0.
 \end{aligned} \tag{5.29}$$

Reducing the kernel to 1D allows only a water content variation in depth

$$\begin{aligned}
 V_R(t) &= \int_0^\infty f(z) \cdot K_{1D}(q; z) dz \\
 &\text{with} \\
 K_{1D}(q; z) &= \int_{-\infty}^\infty \int_{-\infty}^\infty K_{3D}(q; x, y, z) dx dy \\
 \partial f(x) / \partial x &= \partial f(y) / \partial y = 0
 \end{aligned} \tag{5.30}$$

A synthetic MRS sounding curve is obtained by the multiplication of the kernel with a water distribution of the respective dimension. Assumption of a homogeneous water content of 100% in the whole subsurface leads to a sounding that reflects the pattern of the sounding curve in respect to the loop configuration and gives a hint to the maximum possible signal amplitude. Such curves, referred to as calibration soundings, are used in the course of this work for the assessment of different loop configurations.

All modelings for the systematical assessment in the following are conducted for a circular loop with 48m diameter, 2 turns and an Earth magnetic field of 48000nT at an inclination of 60°. The direction of the Earth's field is oriented positive downwards. These settings are typical for mid Europe. Some properties of the modelings change significantly for different inclination angles and magnetic field orientations. Interpretations have therefore to be carefully adopted to local settings, especially for the reverse magnetic field orientation for measurements on the southern hemisphere.

Nomenclature of the variables for fields and vectors are all according to their derivation and explanation in the previous chapter.

5.2.1. Spatial variation of the magnetic field components

The different influence of co- and counter-rotating parts to the MRS response signal has been derived and discussed in the previous chapter. Figure 5.1 sketches the directional dependency of the elliptical decomposition of a loop magnetic field for oblique incidence of the Earth's field at around 60° on the northern hemisphere. In south-north direction (figure 5.1a), the perpendicular component is linear polarized, displayed as blue vector, because \mathbf{B}_0 lies in the ellipse plane of the loop field. Consequently, co- and counter-rotating parts have equal amplitudes. However, the oblique inclination leads in average to larger angles between \mathbf{B}_0 and \mathbf{B} south of the loop center, and consequently larger perpendicular components \mathbf{B}^\perp . In west-east direction (figure 5.1b), the perpendicular components of the excitation field are elliptically polarized, displayed as blue ellipses. For a radial symmetric source, the rotation sense of this ellipse has equal magnitudes but reverse rotation sense on both sides of the loop axis. The decomposition consequently leads to different amplitudes for co- and counter-rotating parts.

Figure 5.2 demonstrates the spatial distribution of the previously sketched co- and counter-rotating parts and the according phase lag in slices west-east (top) and south-north (bottom). In west-east direction, both components are mirror symmetric to each other. The induction induced ellipticity leads to a slight deflection to the west for the co-rotating part and to the east for the counter-rotating part. The phase is axis symmetric in respect to the loop center. The south-north slice has equal amplitudes for co- and counter rotating parts and no spatial phase symmetry at all. Here, the conductivity has no influence on the splitting into co- and counter-rotating parts.

5.2.2. Calibration soundings

The effect of successive loop displacement on MRS measurements is assessed on calibration soundings for different distances and directions of loop separation. The plots in figure 5.3 demonstrate the effect of one separation distance each in two opposite directions as blue and red lines, respectively. For comparison the conventional coincident sounding is additionally drawn as a black dashed line in each plot. The soundings are modeled for separations of 24m, 48m and 72m south-north (top) and west-east separation (bottom), respectively. For the given loop geometry with a diameter of 48m, this is equal to the configurations half overlapping, edge-to-edge and with half a diameter between the edges of the two loops.

In case of separation of the loops in south-north direction (Fig. 5.3), a significant difference occurs depending on the location of the transmitter. For separations in both directions, the curves for north or south displacement reach similar ranges of maximum amplitudes, but have basically different curve shapes. The sounding curves with transmitter in the north shows a monotonous increase of amplitude with increasing q . In case of a transmitter in the south, the sounding curve shows a small maximum at small pulse moments, and, after dropping off to zero, increases to about the same amplitude range than the sounding

5. The MRS response signal

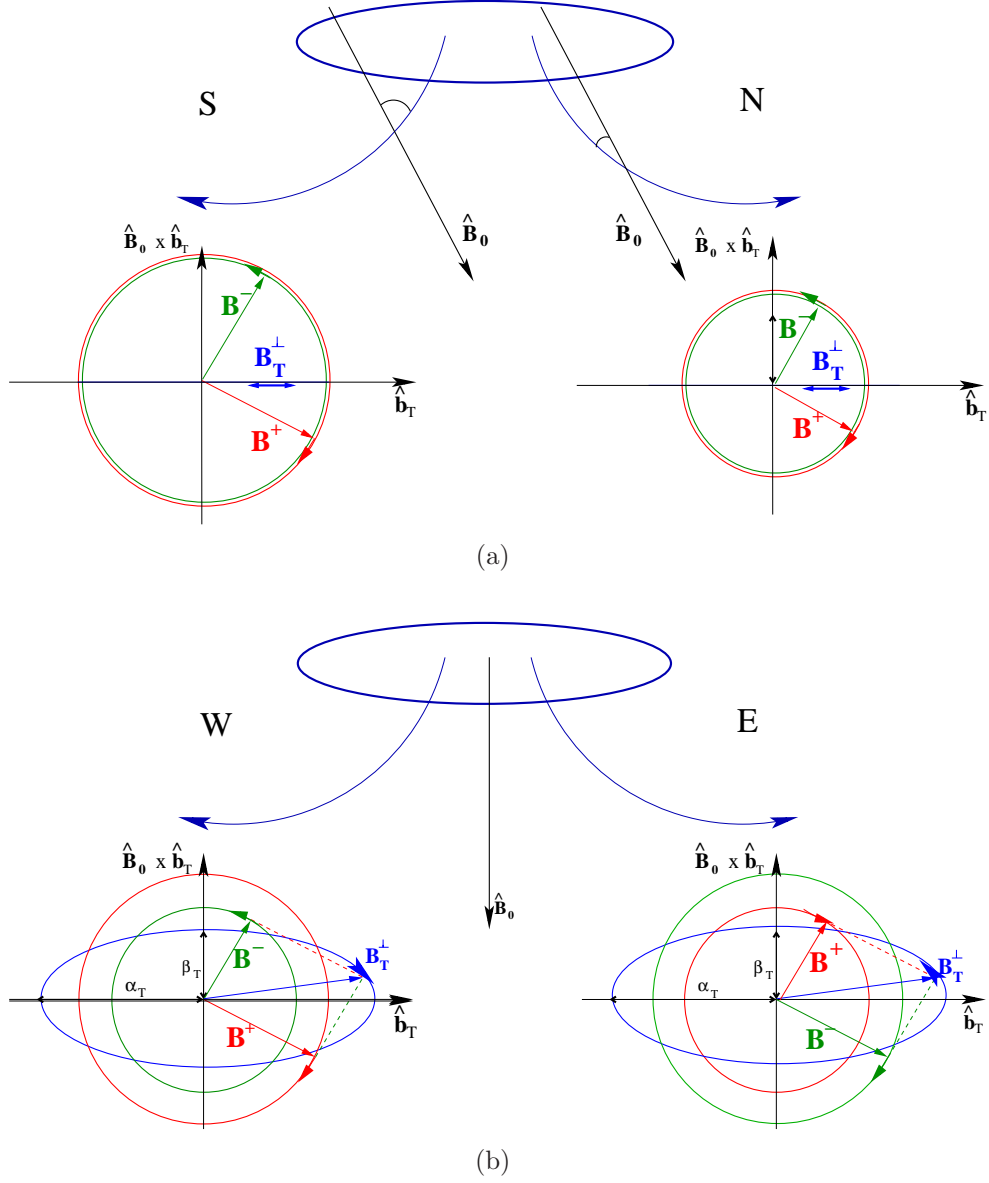


Figure 5.1.: Sketch of the perpendicular components and their decomposition of the magnetic field of a circular loop on a conductive subsurface in south-north (a) and west-east (b) direction. Blue vectors, respectively ellipses, represent the perpendicular field components. Red and green circles show their decomposition into co- and counter-rotating parts in respect to the Spin precession direction in the Earth's magnetic field.

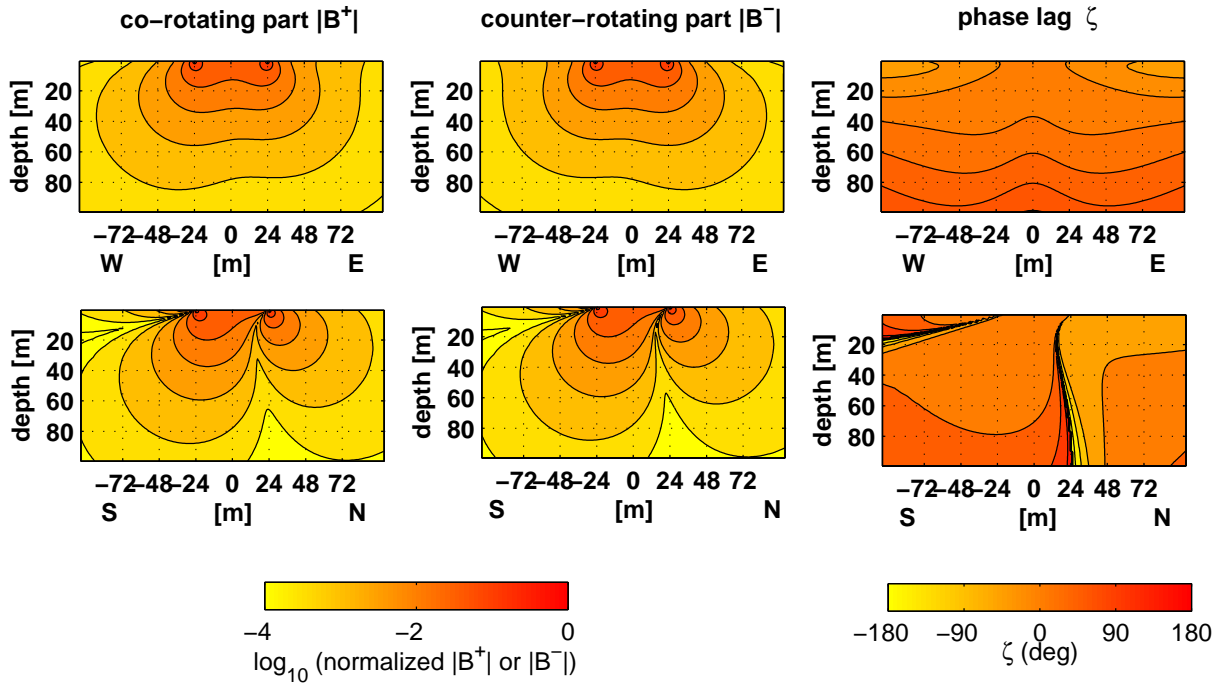


Figure 5.2.: West-east (top) and south-north (bottom) slices of the magnitude of the co-rotating (left), counter-rotating (center) components and the resulting phase lag (right). Modeling was realized for a circular loop with 48m diameter, $50\Omega m$ half-space and an Earth's magnetic field of 48000nT at 60° inclination.

5. The MRS response signal

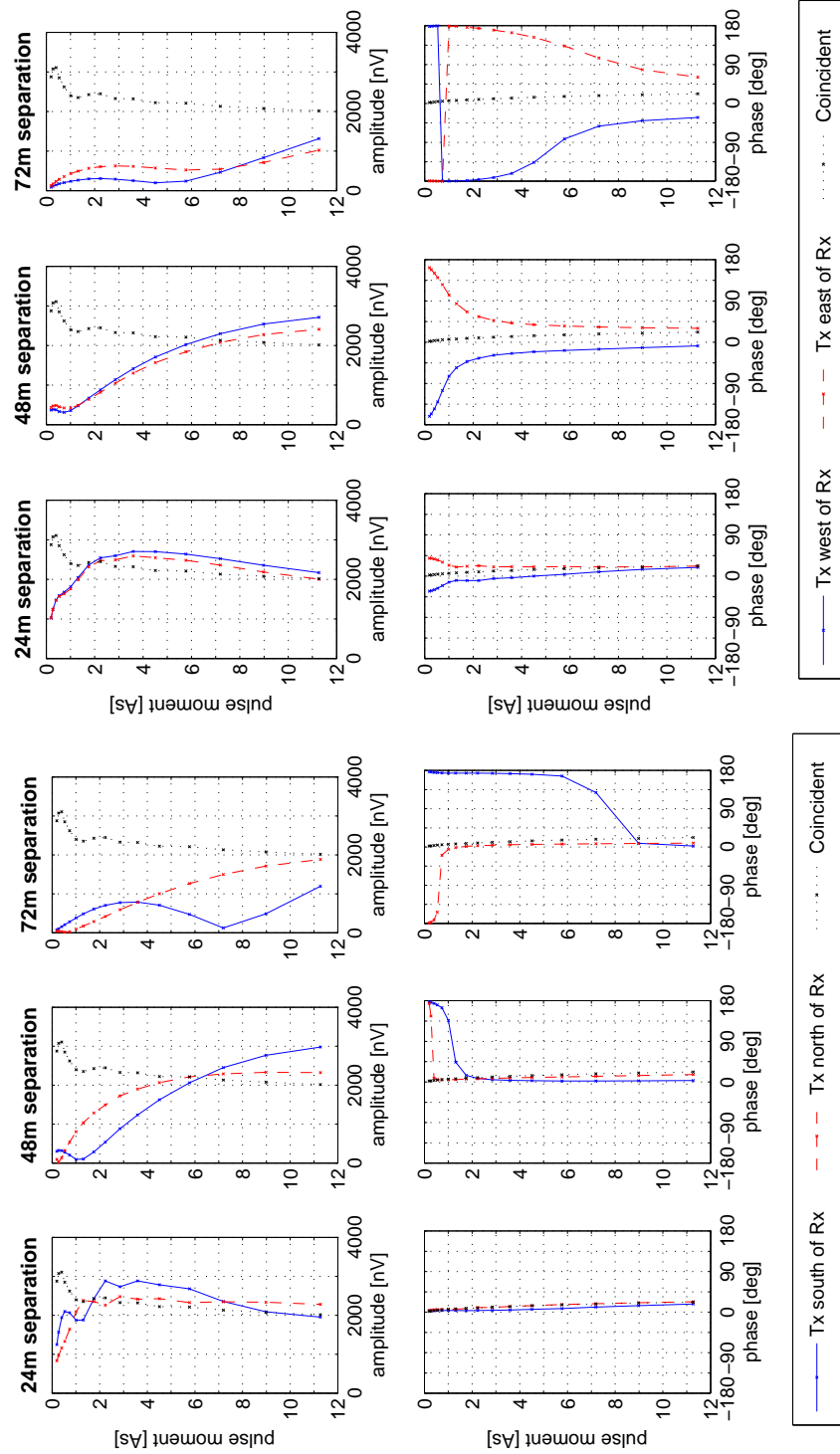


Figure 5.3.: Calibration soundings for loop separation in south-north (a) and west-east direction (b) of 24m, 48m and 72m each. Modeling is realized for a circular loop with 48m diameter, two turns, homogeneous half-space of $50\Omega m$ and 100% water content and an Earth's magnetic field of 48000nT at 60° inclination. Choice of pulse moments is according to a real sounding on similar conditions with a Numis-Plus device.

curve with transmitter in the north. This characteristic minimum appears at successively larger pulse moments for larger loop offset. Typical for these soundings is the phase shift of around 180° at pulse moments, where the amplitude curve reaches its minimum. This is caused by a sign change of the real part of the signal. The occurrence of a second maximum with an accompanying phase shift is specific to transmitter locations south of the receiver.

Pattern of the soundings with transmitter west or east slightly different. The amplitude curves show for all loop displacements quite the same progression with a slight splitting at larger q values. With increasing loop separation the maximum of the sounding curve decreases and shifts towards higher q values. The phase curves are nearly mirror symmetric and possess a smooth curvature decreasing from high absolute values to zero with increasing pulse moment. The symmetry is slightly distorted by the influence of a conductivity determined phase towards positive values. Since both configurations spread perpendicular to the inclination of the Earth's field, the observed difference of the sounding amplitudes is mainly determined by the asymmetric distribution of co- and counter rotating parts in east-west direction (see figure 5.2). The mirror symmetric orientation of the loop field vector of transmitter and receiver west and east of the loop axis, as it enters the general MRS formula in section 5.1, causes the converse phase shifts.

The dependency of the calibration curves on subsurface conductivity is assessed in figure 5.4 for a fixed loop separation of 48m west-east. The accompanying dashed lines for the corresponding coincident loop sounding demonstrate the pure electromagnetic effects of distortion and damping of the amplitude curve and the appearance of an electromagnetic phase delay at small resistivities. For separated loops, both, the sounding curves with south-north and west-east separation change their curvature significantly for decreasing conductivity. Due to the electromagnetic attenuation, amplitudes are smaller and the pattern of the amplitude curve is shifted to smaller pulse moments. The conductivity related phase shift, superimposing the geometrical phase, gains stronger influence. Decreasing conductivity decreases the influence of the electromagnetic attenuation accordingly. The difference between calibration sounding amplitudes in west-east separation consequently disappears and the phase shift becomes solely geometrically determined and therefore perfectly mirror symmetric. At $500\Omega m$ a conductivity influence is hardly recognizable. For south-north separation reverse orientations of transmitter and receiver show a significant difference in amplitude and phase curves due to the major effect of induction independent asymmetric distribution of co- and counter-rotating parts in this direction. With decreasing resistivity both curves are evenly attenuated but no correlation of both curves can be observed.

5.2.3. The 1D Kernel

The Kernel function for 1D conditions as derived in equation 5.30, is the integration of the full 3D kernel function over the horizontal directions. The result represents the specific signal contribution with depth for each single pulse moment. As demonstrated in figure

5. The MRS response signal

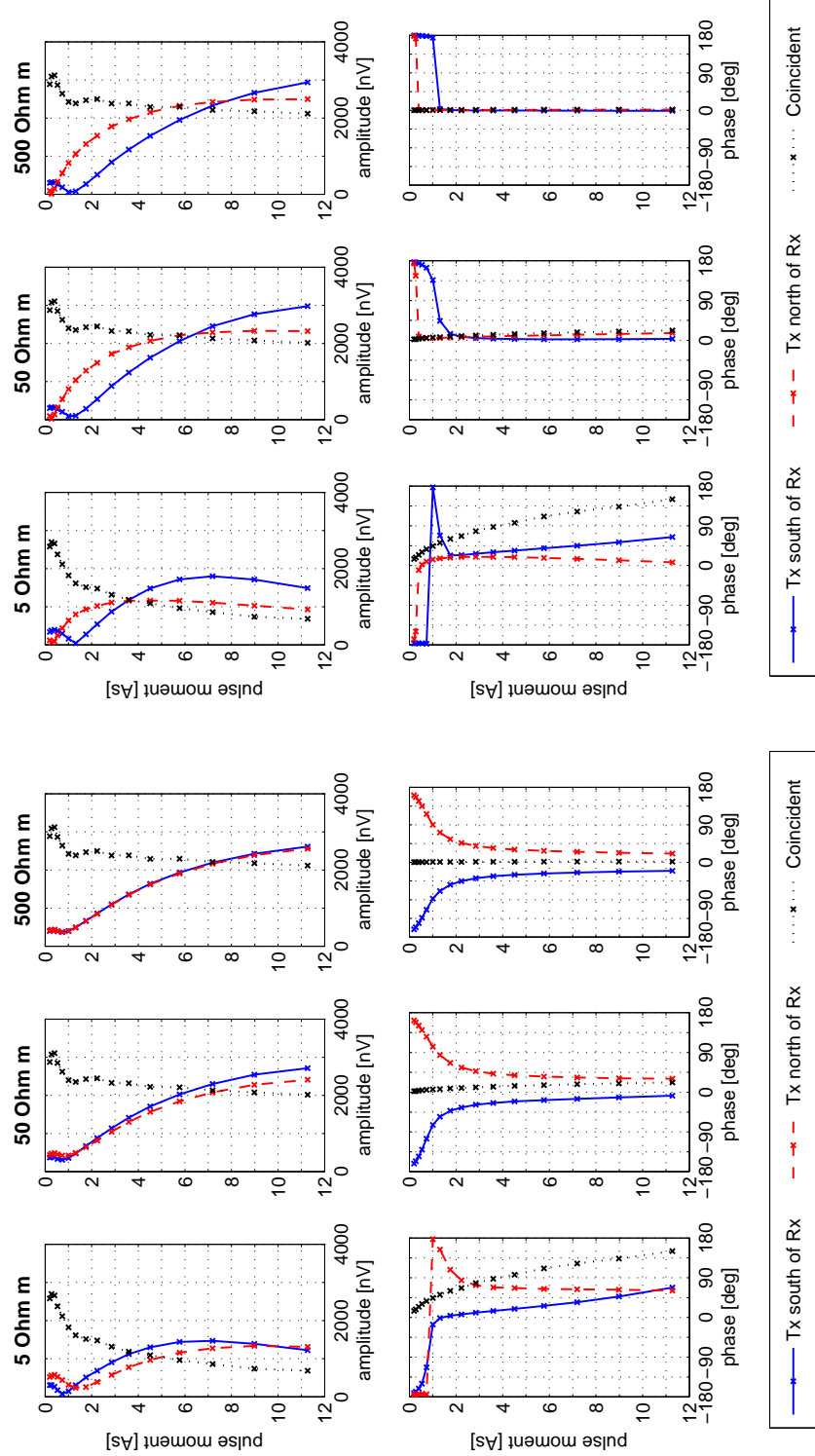


Figure 5.4.: Calibration soundings as in figure 5.3, but with constant loop separation of 48m and variable resistivity of 5 Ω m, 50 Ω m and 500 Ω m, respectively.

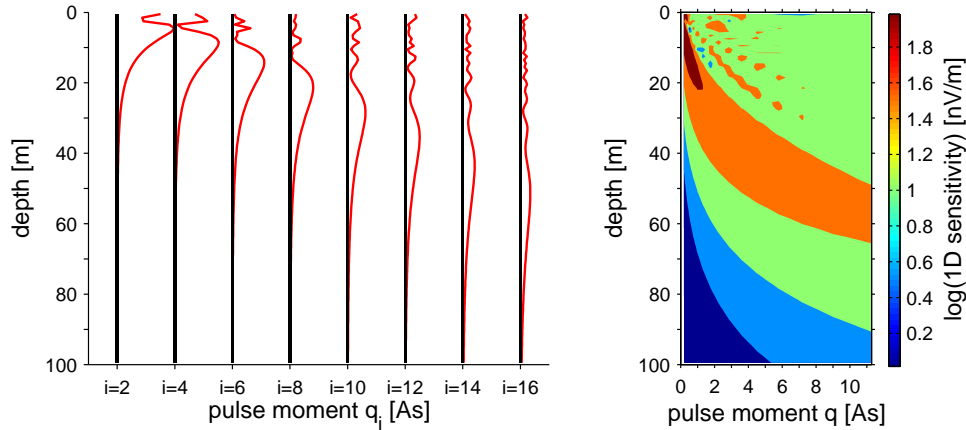


Figure 5.5.: Schematic presentation of the depth sensitivity of a 1D kernel. Left as line plots for each pulse moment, right as contour plot versus the pulse moment value.

5.5a) for coincident loops, this function shows a region of maximum signal contribution for each pulse moment, successively broadening and appearing deeper with increasing q . For a more convenient interpretation of vertical signal contribution versus pulse moment, the contour representation as shown in figure 5.5 b) is commonly used.

Figures 5.6 and 5.7 assess the properties of the kernel functions for separated loop soundings in both south-north and west-east orientations, respectively. For coincident loops (center column), the kernel functions shows the well known depth focus characteristics. For increasing loop separations, the area of main signal contribution is located at successively shallower regions. As expected from figure 5.4, comparison of the kernels with transmitter positions south and north of the receiver shows no clear symmetry. In contrary, for east west separation, the real parts of the kernel are nearly equal for both transmitter displacements. The imaginary part is about mirror symmetric and causes the opposite phases of the corresponding calibration soundings. For vanishing induction, i.e. a resistive medium, the absolute values of imaginary parts become perfectly symmetric but with opposite signs due to reverse orientation of the field vectors of transmitter and receiver.

5.2.4. The 2D Kernel

A high potential of the technique of separated loop MRS measurements lies in the investigation of 2D structures. Similar to the formulation of the 1D kernel in the previous section, the general formula for the MRS response is reduced by summation according equations 5.28 and 5.29 along one dimension. The resulting 2D kernel then represents the sensitivity of a sounding to a water content distribution, assumed to be infinitely extended in the summation direction. To avoid any confusion, the now found 2D-kernel has to be carefully distinguished from sections or slices through the 3D volume. Even though, the graphi-

5. The MRS response signal

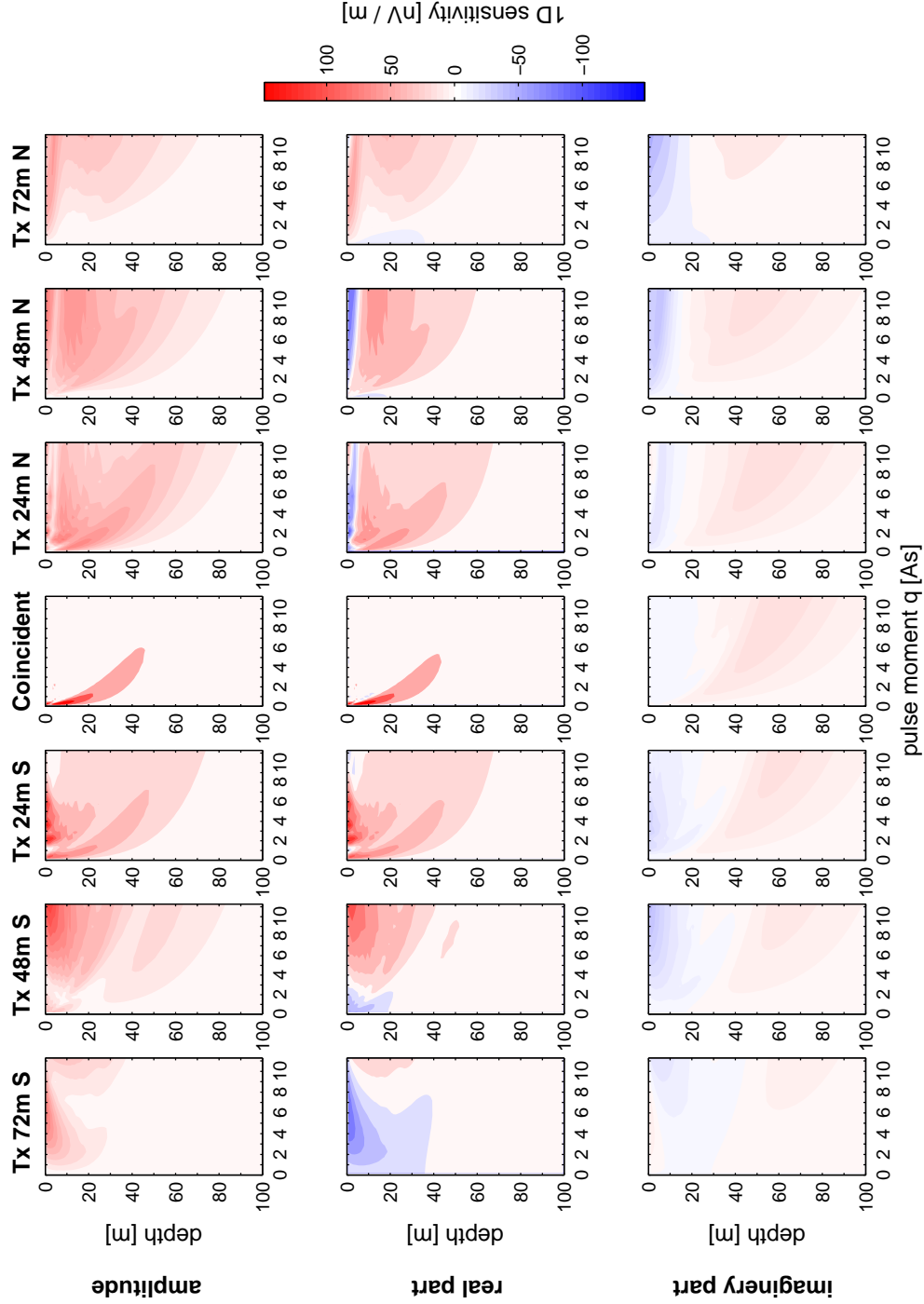


Figure 5.6.: Contour plots of the 1D kernels for transmitter positions from 72m south to 72m north of the transmitter in 24m steps. The first row shows the amplitude of the kernel function, second and third row the real and imaginary parts respectively. Modeling is realized for a circular loop with 48m diameter, two turns, homogenous half-space of $50\Omega m$ and 100% water content and an Earth's magnetic field of 48000nT at 60° inclination. Choice of pulse moments is according to a real sounding on similar conditions with a Numis-Plus device.

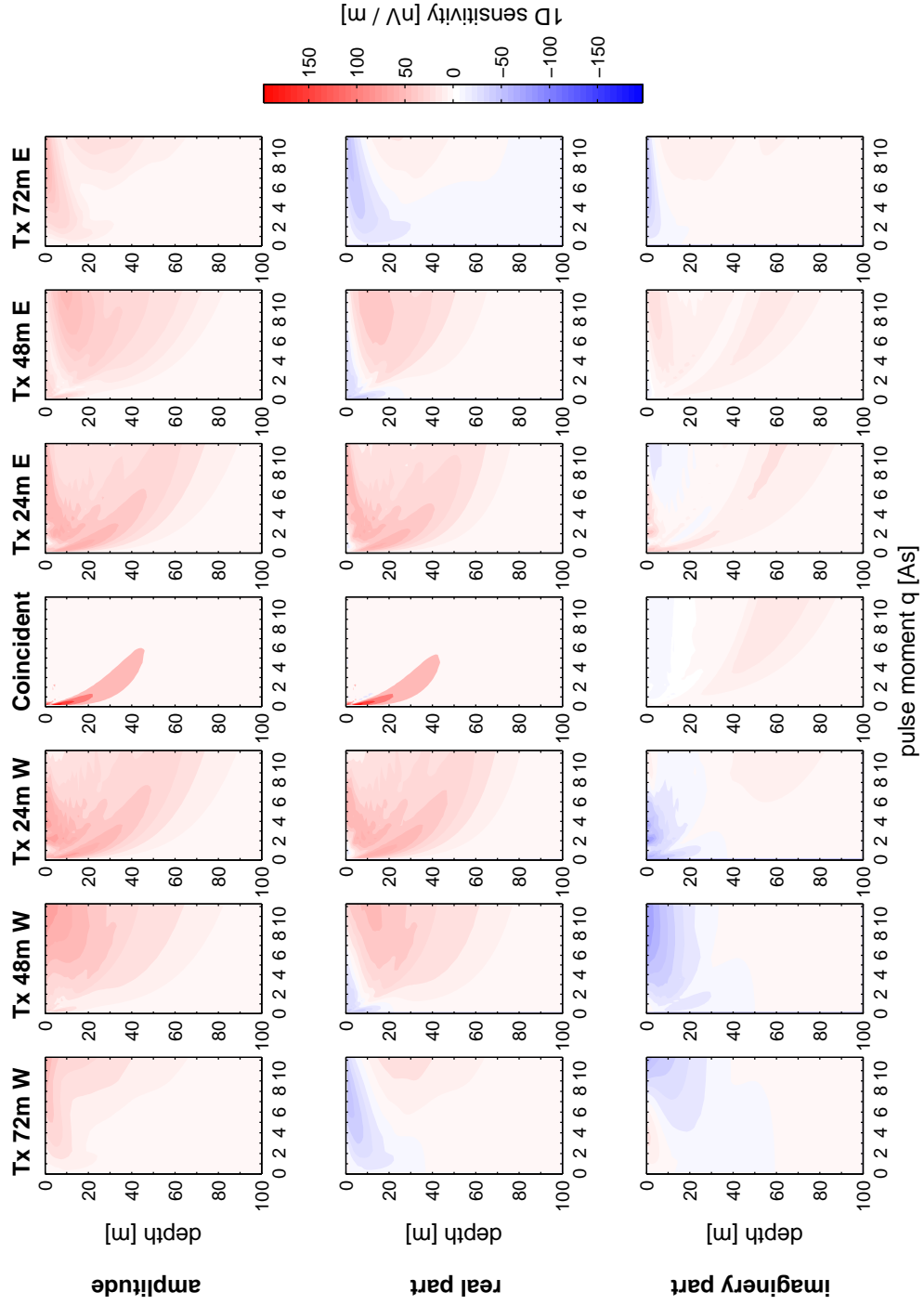


Figure 5.7.: Same as figure 5.6, but for west-east separation.

5. The MRS response signal

cal representation is similar, the meaning is quite different. With the use of 2D kernels, the assessment of spatial sensitivity can be extended beyond the depth information to its horizontal extension.

In the representations of the 1D kernels, one contour plot could be used to completely visualize the sounding pattern in depths versus pulse moment q . Extending the interpretation by the lateral dimension, one contour plot of 2D signal distribution is needed for each q separately.

It turns out to be instructive to display the single kernel parts as derived in equation 5.23 separately. Here the 1D integration in the horizontal dimension perpendicular to the profile direction are individually performed for each part of the product of the full kernel. The full kernel, however, is the 1D integration of the product of the un-integrated single kernel parts. In figures 5.8 to 5.11 the single integrated kernel parts and the full 2D kernel are shown for four different q values in separate rows. To demonstrate the differences of signal distribution for different loop configuration we compare exemplarily 2D kernels and kernel parts for coincident loops (figures 5.8 and 5.10) and with a transmitter loop located 48m west of the receiver (figures 5.9 and 5.11). The corresponding 2D kernels with the same separation distance but different directions are shown in Appendix B. The general 3D kernel is reduced to a 2D kernel by summation over one Cartesian direction. Figures 5.8 and 5.9 show 2D kernels with summation direction horizontally perpendicular to the separation direction, i.e. south-north in this particular case. This gives a section view of the 2D kernels in the x - z plane. Additional information can be obtained from 2D kernels with a summation direction in depth, leading to a map view in the x - y plane. These plots are presented in figures 5.10 and 5.11.

The first part of the kernel function for the section views in figures 5.8 and 5.9 shows the 1D integration of the excited Spins in the subsurface. At small pulse moments highest resulting excitation is observed right below the loop. Increasing the excitation intensity leads to an increasing zone of vanishing resulting excitation below the loop and the formation of a zone of major signal content. This zone broadens and spreads radially with distance from the loop center. This effect is caused by the rapid nutation of the Spin systems in the strong field close to the loop. Here, the large gradient leads to a de-phasing of the Spin magnetization and consequently to a destructive interference of adjacent Spins. The integral Spin magnetization from this volume approaches zero. Only at small excitation angles they interfere constructively and a region of large resulting magnetization is achieved. The distance from the loop and the width of this zone increase with increasing q . Due to the distribution of the co-rotating part of the loop field, controlling the Spin perturbation, this signal region is slightly deflected to the west.

The second part of the kernel represents the sensitivity of the receiver to the induced NMR signal in the investigation volume. It decays approximately exponentially with distance from the loop. The excitation intensity has no influence on this kernel part and is thus equal for all q values. Its dependency on the counter-rotating part of the receiver loop field causes the eastward deflection.

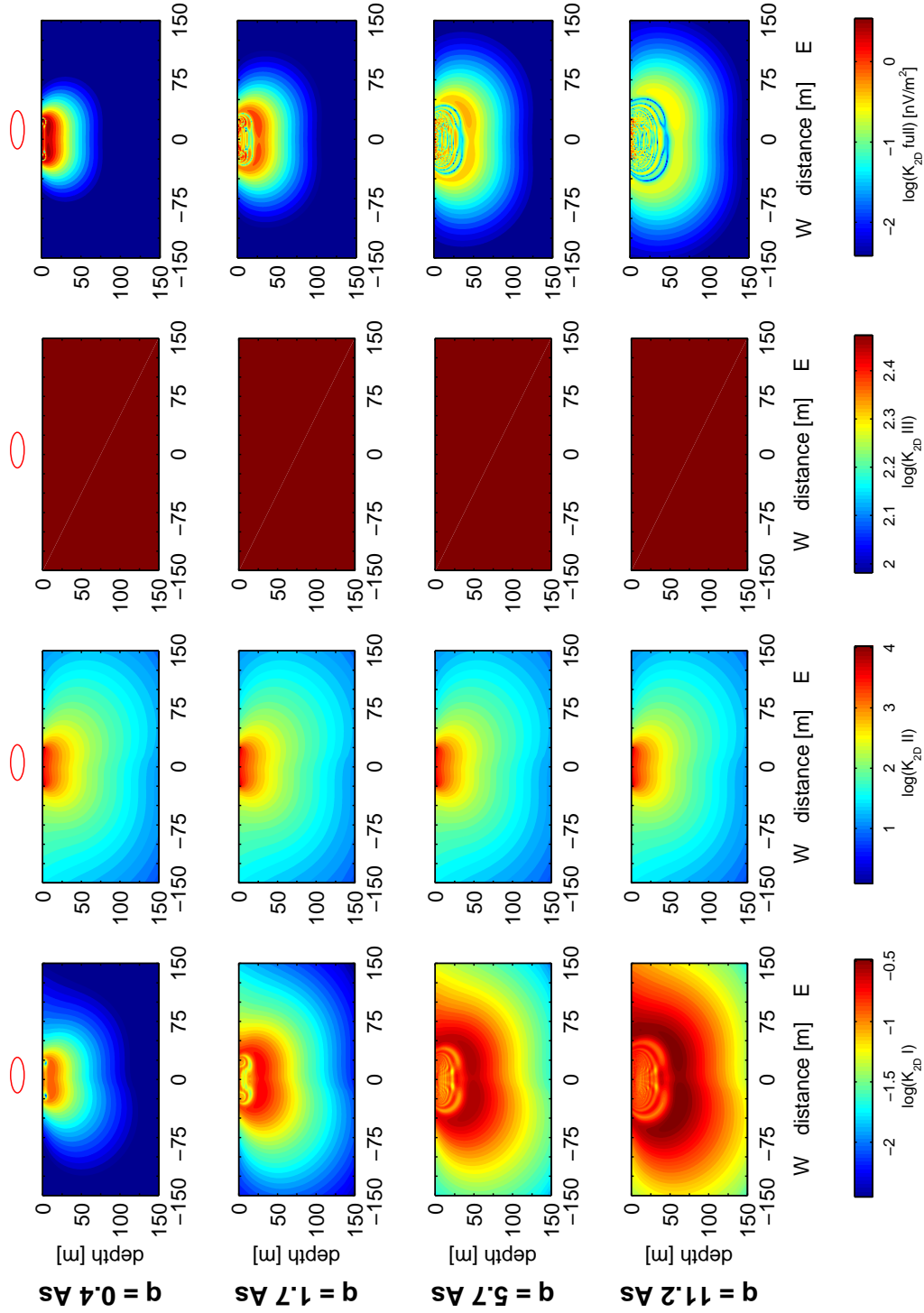


Figure 5.8.: Presentation of 2D kernels in section view in west-east direction. Column 1-3 show the respective kernel parts as discussed in chapter 5.1. Rows show the 2D kernels for the 2nd, 5th, 9th and 16th pulse moment of the sounding shown in section 5.2.2. Modeling is realized for a circular loop with 48m diameter, two turns, 50Ωm half-space and an Earth's magnetic field of 48000nT at 60° inclination.

5. The MRS response signal

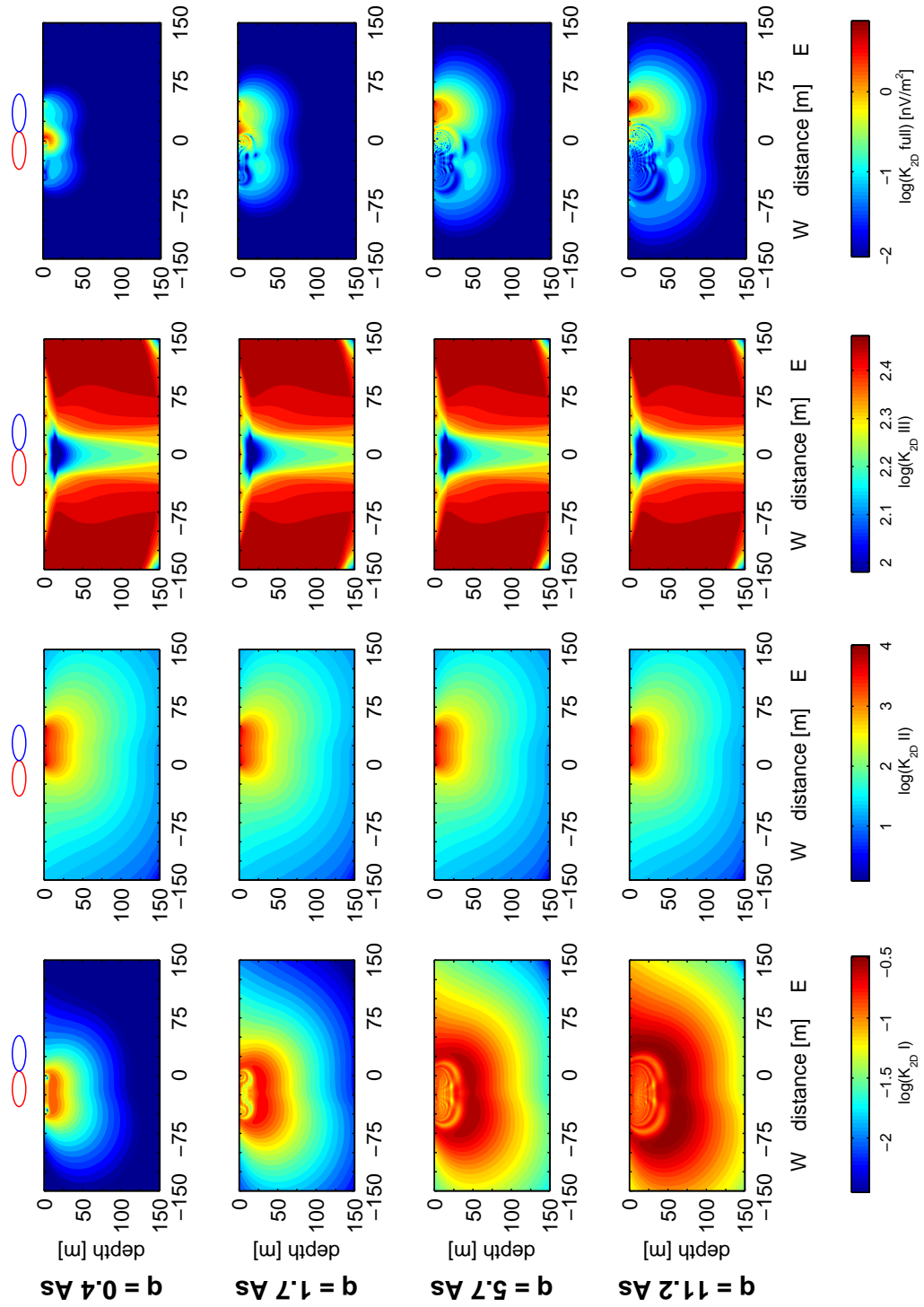


Figure 5.9.: Same presentation of 2D kernels as in figure 5.8, but for a transmitter position 48m west of the receiver.

Whereas the first two parts of the kernel are the same for coincident and separated loop configuration with only a lateral shift according to the respective loop position, the third part, the projection part, of the kernel gains significant influence for separated loops. As obvious from the basic MRS formulation, the third part is unity throughout the total volume for coincident loops and has no scaling effect on the MRS signal response. In case of separated loops a characteristic minimum of the projection part is observed. It ranges from the area below the surface extension of the loops, slightly narrowing with depth. It is mirror symmetric to the midpoint of the two loops. This characteristic minimum describes a shadow zone of spatial sensitivity. Even though a large resulting magnetization is induced in this area by the transmitter and the receiver shows a significant sensitivity to it, the mutual orientation of their field vectors to the Spin orientation inhibits the evolution of a recordable signal in the receiver.

Finally, the section view of the complete 2D kernel in the fourth row represents the resulting contribution range of the effectively recorded MRS signal. For coincident soundings the signal is induced in regions successively remote from the loop, where the receiver has decreasing sensitivity. The distribution of the contributing signal is spread through a large area well outside of the loop area. For a loop separation of 48m part of the resulting Spin excitation is located in the area below the receiver with successively increasing q values. There, the receiver has principally significant sensitivity but due to the influence of the projection term only part of it finally contributes to the resulting MRS signal. However, the major part of the signal evolves from a confined zone. The area of the major signal contributing is located below the contact of the loops at small q 's and successively propagates towards the remote half of the receiver loop with increasing pulse moment. The depth of signal contribution remains restricted to about one loop diameter even for large pulses.

Similar pattern are observed in the map representations of the 2D kernels. As obvious from the first column in figures 5.10 and 5.11, the excited Spin magnetization is located approximately annular around the transmitter loop, increasing in width and distance with increasing q . The sensitivity of the receiver loop decreases about exponentially with distance from the loop. Since the projection term is not of any influence for the coincident sounding, the effectively contributing signal evolves from a large annular area out of the loop.

In case of the separated loops the shadow zone, caused by the projection term of the kernel, shows a lateral extension mainly between the loops with significant deflection in south-north direction due to the Earth's field inclination. As already observed in the discussion of the full 2D kernels in section view, the area of contributing signal is confined to a much smaller region for separated loops than for coincident loops. For small pulses it is located between the loops and spreads towards a semicircular area below the remote half of the receiver for increasing q 's.

The distribution of the 2D spatial sensitivity as discussed in the previous figures regards only the sensitivity of the signal amplitude. Additional spatial information can be gained

5. The MRS response signal

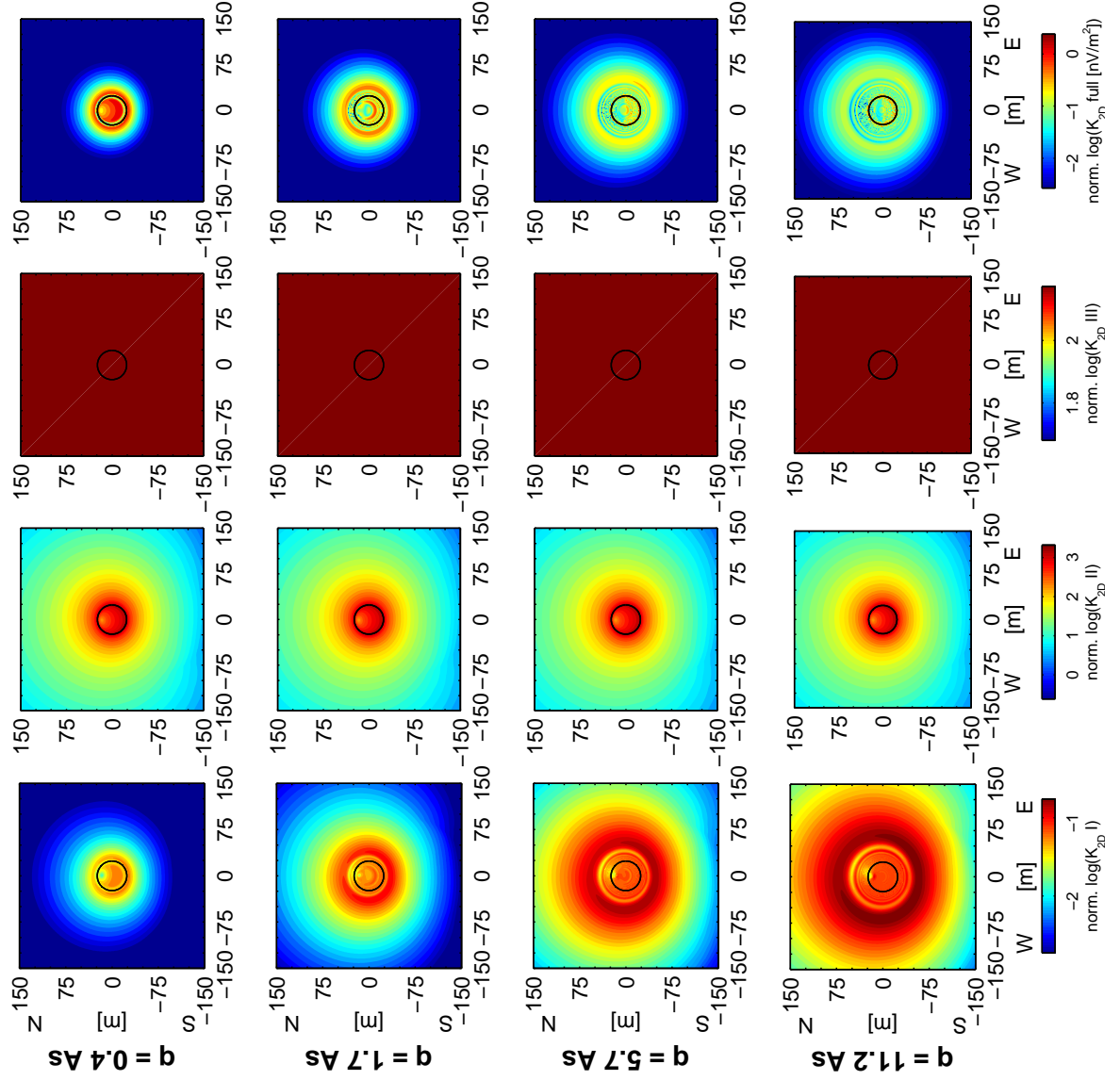


Figure 5.10.: Presentation of 2D kernels in map view for coincident loops. Display and sounding properties are the same as in figure 5.8.

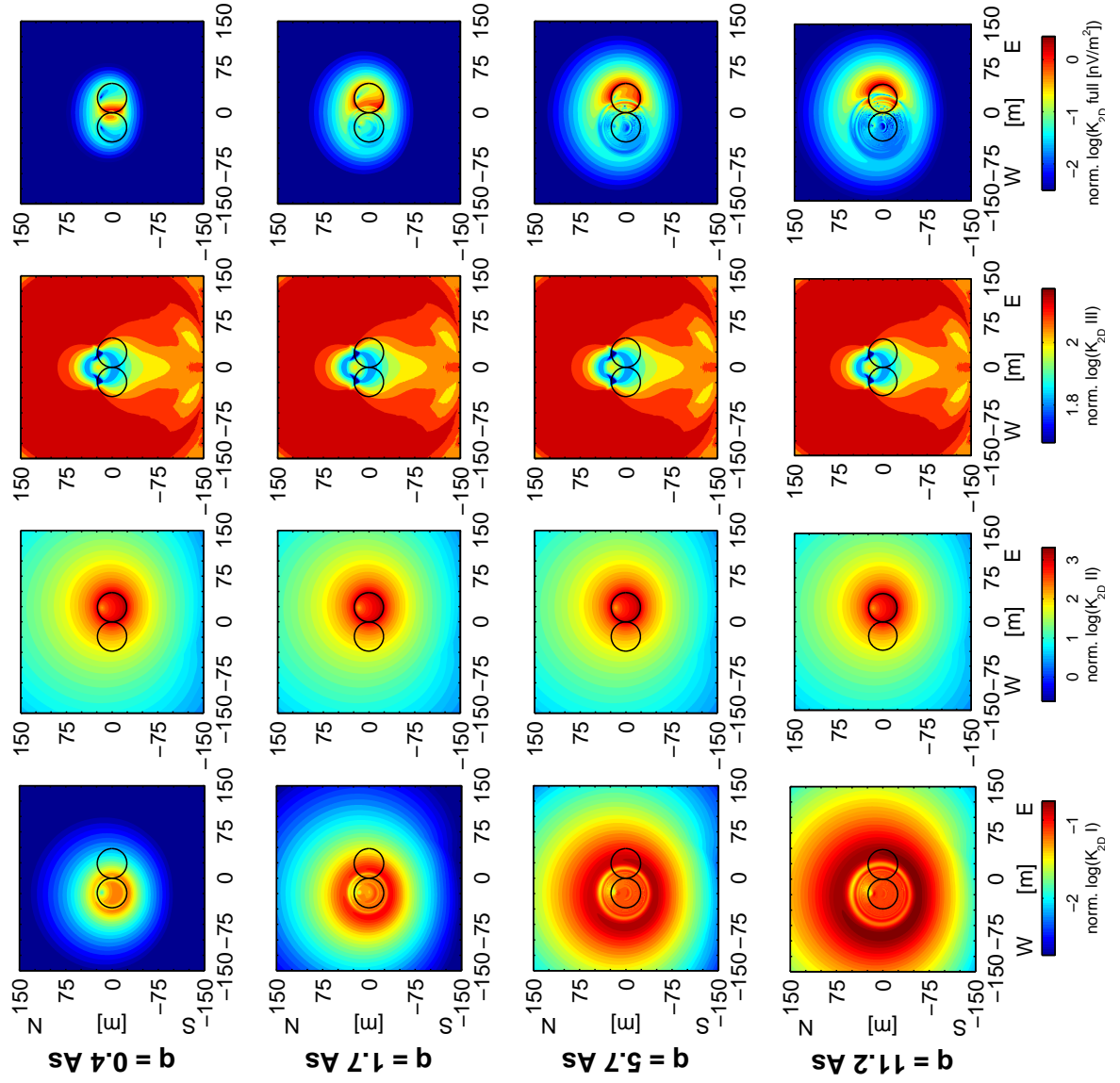


Figure 5.11.: Same presentation of 2D kernels as in figure 5.10, but for a transmitter position 48m west of the receiver (see Fig. 5.9).

5. The MRS response signal

from the phase lag of the signal, i.e. the real- and imaginary parts. This complex valued signal is determined by the ground conductivity on the one hand, influencing the magnetic field of transmitter and receiver. On the other hand it is determined by the complex geometric term in case of separated loops. The contributing signal amplitudes from different regions in the subsurface have individual phase lags as demonstrated in Fig. 5.12. Here the real- and imaginary parts for coincident and separated loop soundings are presented as 2D kernels, exemplarily for pulse moment no. 8 of 5.7 As. In case of coincident soundings, the imaginary part remains about one order smaller than the real part throughout the three kernel parts and also for the full kernel for the given conductivity of 50om. However a characteristic difference can already be observed in the spatial distribution. Here, the values of the real part increases steadily with distance from the loop whereas the imaginary part shows negative values close to the surface and become positive towards greater depths. In case of separated loop soundings the influence of the imaginary part increases significantly due to the complex geometric term. The imaginary geometric term is still significantly smaller than the real part. Nevertheless, the full 2D kernel finally shows nearly equal real and imaginary parts, which was already indicated by the calibration soundings of section 5.2.2, where large phase values are observed. The spatial distribution of the complex components gives finally raise to effectively discriminable areas of different real- and imaginary part ratios. For the given example in Fig. 5.12 positive values of the real parts and negative values for the imaginary part at shallow depths between 0m and 25m are observed. A few meters further things change and we observe negative values for the real part and negative ones for the imaginary part. Even though signals from these regions contribute with about the same magnitude to the response signal, their signal phase is opposite. So the complex MRS response signal gives an enhanced spatial resolution to the water content distribution. The effect of different sensitive regions of real and imaginary parts of 1D soundings has already been studied concerning an optimized inversion (Braun et al., 2004). For moderate conductivities this effect is quite small according to the small phase information compared to the signal to noise ratio. For separated loops the real and imaginary parts achieve the same range of magnitude in the region of highest absolute sensitivity. So the discrimination of the spatial signal distribution in separate loop soundings is much more promising.

5.3. Field data

A field survey has been conducted to verify the correctness of the theoretical formulation and the numerical realization of the modeling algorithm. In cooperation with IRIS Instruments and the French Geological Survey, BRGM, measurements were conducted in StCyr en Val close to Orleans (France) with a Numis Plus, configured to record the MRS signal in a separate receiver loop. Soundings were recorded on a site with assumed horizontal layering, providing approximately 1D conditions. Figures 5.13 a) and b) show the soundings for a transmitter loop fixed at the center and shifting the receiver. Receiver positions were situated half overlapping and edge-to-edge in south and north separation direction

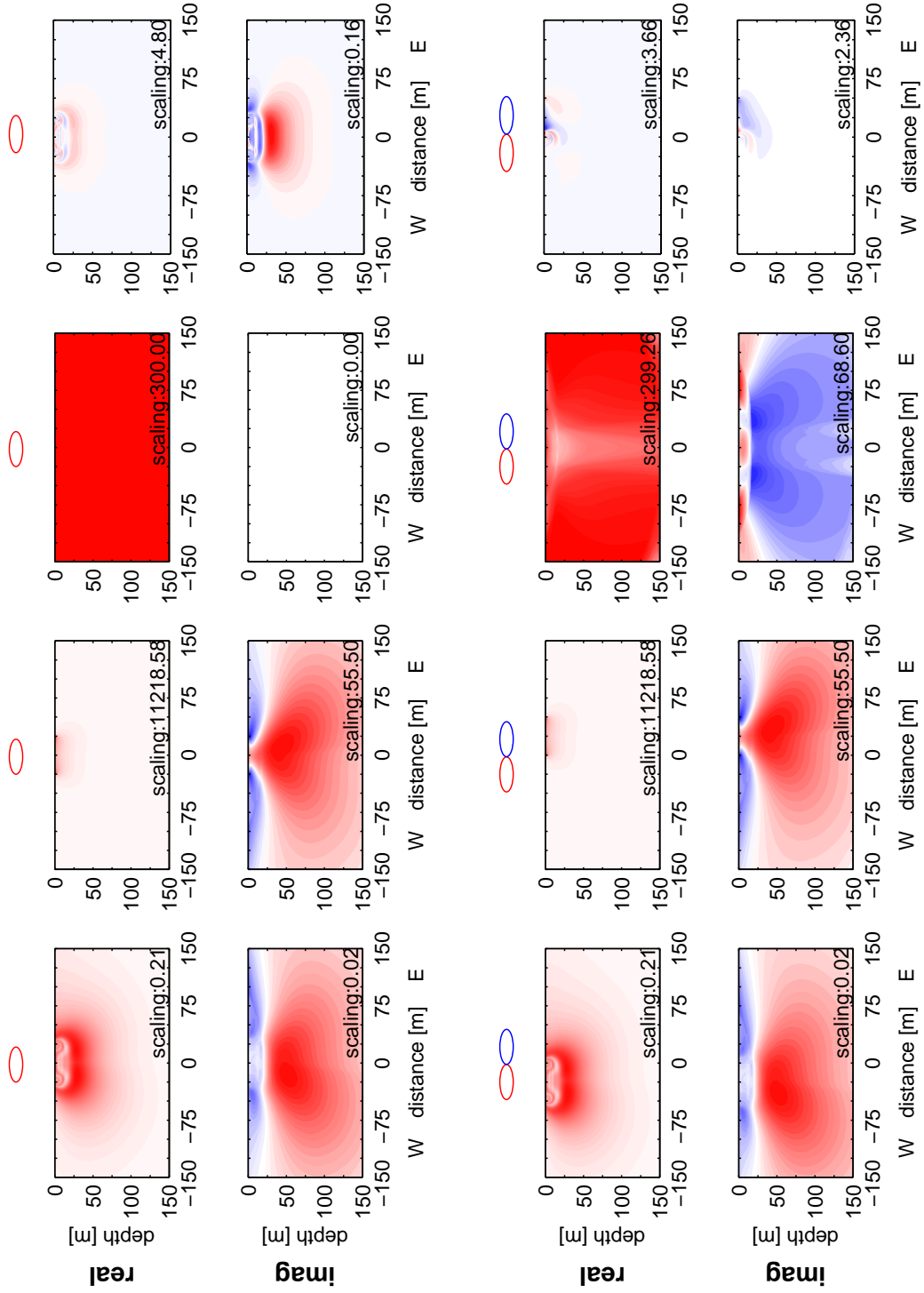


Figure 5.12.: Real- and imaginary parts of the 2D kernel in west-east direction for coincident loops (top) and 48m separated (bottom) for a pulse moment of 5.7 As. All plots are normalized to their maximum value, the respective scaling factors are displayed within each figure.

5. The MRS response signal

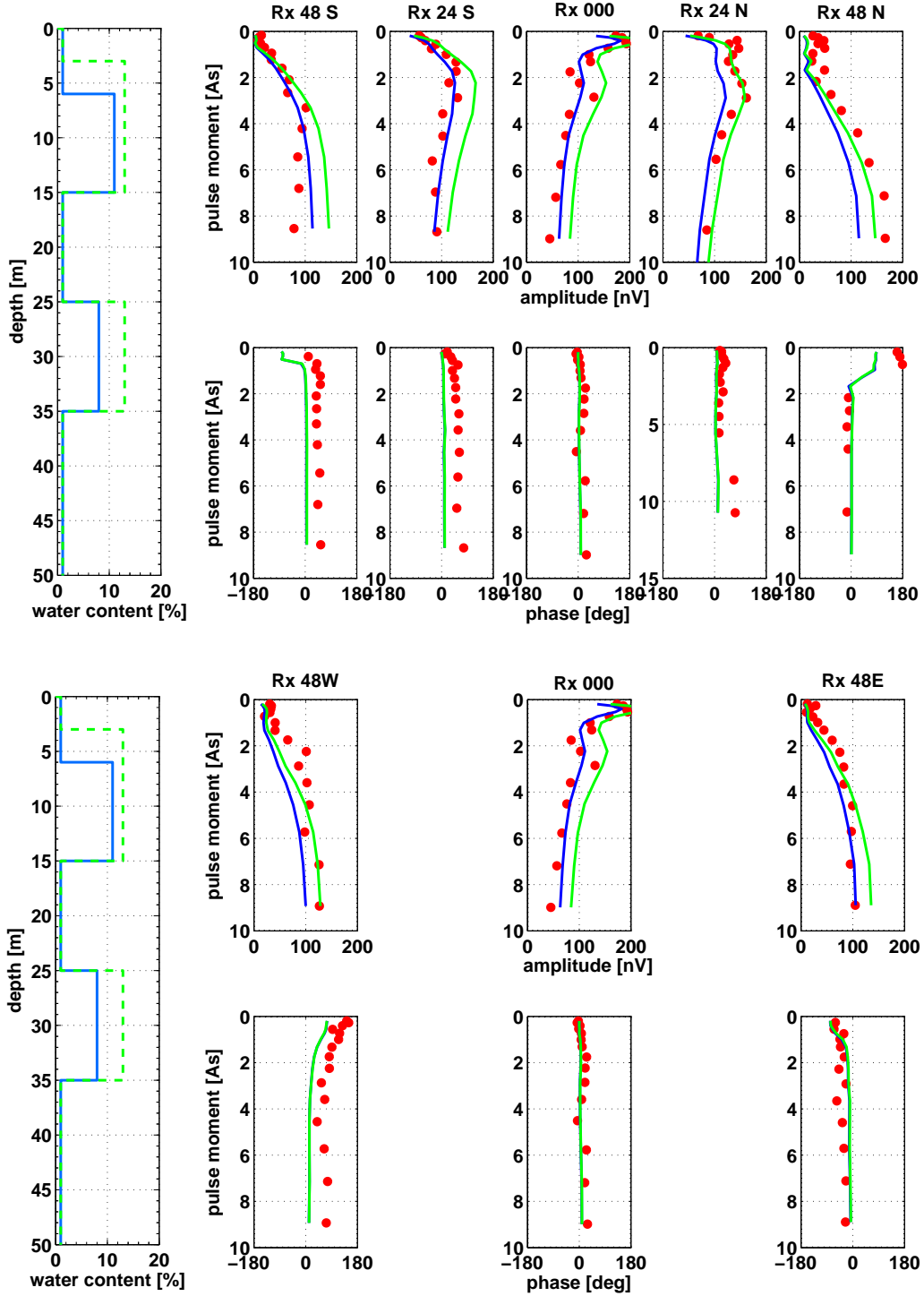


Figure 5.13.: Results of MRS measurements at the test site in StCyr en Val, France. a) shows the soundings in amplitude (top) and phase (bottom) for receiver locations successively from south to north in 24m steps. b) shows the results for receiver locations successively from west to east in 48m steps. The leftmost subplots represent two different water distributions with depth in blue and green which are used for the respective synthetic soundings. Red dots represent the measured data. Transmitter position is at origin 0,0 m.

and edge-to-edge in west and east separation direction. The synthetic modelings show that a very sensible water model can be found to fit the recorded soundings appropriately. The models are found by manual adaptation to fit all sounding curves appropriately, not by inversion. In the south-north separation direction, the model to fit the soundings best changes along the profile. The model with an upper aquifer from 3m to 15m (green dashed line) fits better the soundings with the receiver in the north, whereas a model with a somewhat deeper water table at around 5m fits the soundings with receiver in the south better (blue solid lines). In all soundings the basic curve characteristics, predicted from synthetic modeling are excellently reproduced. The calculated MRS soundings fit not only the measured amplitudes excellently. Also the phase propagation, containing the new formulated geometric phase for separated loops, agrees appropriately with predictions from forward modeling.

The significant deviation of the forward modeled sounding curves with a slightly varying first aquifer along the profile of south-north separation underlines the high spatial resolution of separated loop measurements to shallow targets.

5. *The MRS response signal*

6. Application of MRS to 2D water distributions

In the preceeding chapter a high spatial sensitivity is observed for single separated loop soundings. In the following the improvement of spatial resolution of surveys consisting of a set of coincident and separated loop soundings is assessed and compared to surveys with conventional coincident loops only but equal number of loop positions. The assessment of synthetic surveys over different kind of aquifer models investigates potential and limits of the spatial resolution with coincident and separated loops. A quite special kind of MRS target on arctic ice cover is discussed and evaluated according to some special features of MRS sounding characteristics and subsurface sensitivity. Finally a detailed investigation of real surveys and comparison to the geological situation and additional geophysical data outlines the potential of the separated loop technique.

6.1. MRS modeling

The recorded MRS signal in the receiver loop is the integral signal of all contributing Spin systems in the subsurface. The contribution of each volume element to the total signal depends on the magnitude of its achieved dynamic magnetization and the sensitivity of the receiver to the oscillating magnetization in this volume element. Like in other NMR applications, the magnetization vector of the Spin system is forced to a precessional motion around the direction of the static field. The excitation angle is determined by the magnitude of the exciting field at this point and the duration of the exciting pulse. Since the equilibrium magnetization of the Spin system is oriented along the static field, the Earth's field in MRS applications, only the perpendicular component of the exciting field to this field direction physically acts on the Spin system. Vice versa, the component of the precessing Spins perpendicular to the receiver field contributes to the voltage induced in the receiver antenna. As previously shown by Weichman et al. (2000), the elliptical components rotating with and against the rotation sense of the Spin system in the Earth's field individually contribute as co- and counter-rotating parts of the transmitter and receiver fields, respectively. In case of non-coincident transmitter and receiver loops the orientation of both loop fields causes an additional complex scaling factor of the resulting recorded signal (Weichman et al., 2000). The total signal induced in the receiver loop is calculated by the integration over the full subsurface. The common expression for the MRS response

6. Application of MRS to 2D water distributions

signal is given by the equation

$$\begin{aligned}
 V_R(q) = & \omega_L \int d^3r \mathbf{M}_N^{(0)} \sin \left(-\gamma \frac{q}{I_0} |\mathbf{B}_T^+(\mathbf{r})| \right) \\
 & \times \frac{2}{I_0} |\mathbf{B}_R^-(\mathbf{r})| \cdot e^{i[\zeta_T(\mathbf{r}, \omega_L) + \zeta_R(\mathbf{r}, \omega_L)]} \\
 & \times \left[\hat{\mathbf{b}}_R^\perp(\mathbf{r}, \omega_L) \cdot \hat{\mathbf{b}}_T^\perp(\mathbf{r}, \omega_L) + i \hat{\mathbf{b}}_0 \cdot \hat{\mathbf{b}}_R^\perp(\mathbf{r}, \omega_L) \times \hat{\mathbf{b}}_T^\perp(\mathbf{r}, \omega_L) \right]. \quad (6.1)
 \end{aligned}$$

Here, $|\mathbf{B}_R^-|$ and $|\mathbf{B}_T^+|$ denote the magnitudes of the elliptical components of the receiver and transmitter field, ζ the electromagnetic phase delay, $\hat{\mathbf{b}}_{R,T}^\perp$ the respective unit direction vectors of the loop fields, $\hat{\mathbf{b}}_0$ the unit direction vector of the Earth's field and $\mathbf{M}_N^{(0)}$ the equilibrium magnetization. Additionally, the Larmor angular frequency ω_L , the gyromagnetic ratio of protons γ and the pulse moment q normalized to a unit current I_0 through the transmitter coil. The pulse moment q is defined as the product of the pulse duration τ_p and the current I through the transmitter coil (Legchenko and Valla, 2002). By variation of the pulse moment q one can vary the spatial distribution of excitation angles of the Spin magnetization and thereby control the spatial sensitivity of a sounding (Yaramanci, 2000). The pattern of MRS soundings with variable antenna offset have been extensively studied in a preceeding publication (Hertrich et al., 2004). It has been shown that the major part of the MRS signal for coincident antennas evolves from regions successively remote from the loops with increasing pulse moment with a special focus to increasingly larger depth. In contrary, in case of separated antennas the major part of the signal evolves from shallow regions below the receiver loop with increasing q . A combination of several soundings with coincident configuration and several antenna offsets is supposed to provide a sufficient coverage to obtain an increased spatial resolution for two dimensional water distribution mapping.

6.2. 2D sensitivity

As shown in equation. 6.1, the integral formula of the MRS response signal consists of the spatial distribution of the magnetization vector $\mathbf{M}_N^{(0)}$ and the spatial distribution of the magnetic fields of transmitter and receiver loops as well as some physical constants. As commonly done in MRS modeling the integral can be rearranged such, that all parameters that remain constant for a certain sounding configuration are combined to a kernel function. Decomposing the macroscopic magnetization vector $\mathbf{M}_N^{(0)}$ as the product of the water content $f(\mathbf{r})$, being half the number of protons in this volume element, and the specific

magnetization $M^{(0)}$ we can rewrite equation. 6.1 as

$$\begin{aligned}
 V_R(q) &= \int d^3r f(\mathbf{r}) K(\mathbf{r}) d\mathbf{r} \\
 &\text{with} \\
 K(\mathbf{r}, q) &= \omega_L M^{(0)} \sin\left(-\gamma \frac{q}{I_0} |\mathbf{B}_T^+(\mathbf{r})|\right) \\
 &\quad \times \frac{2}{I_0} |\mathbf{B}_R^-(\mathbf{r})| \cdot e^{i[\zeta_T(\mathbf{r}, \omega_L) + \zeta_R(\mathbf{r}, \omega_L)]} \\
 &\quad \times \left[\hat{\mathbf{b}}_R^\perp(\mathbf{r}, \omega_L) \cdot \hat{\mathbf{b}}_T^\perp(\mathbf{r}, \omega_L) + i \hat{\mathbf{b}}_0 \cdot \hat{\mathbf{b}}_R^\perp(\mathbf{r}, \omega_L) \times \hat{\mathbf{b}}_T^\perp(\mathbf{r}, \omega_L) \right] \quad (6.2)
 \end{aligned}$$

The computation of the MRS integral of the above equation can be transformed to Cartesian coordinates like

$$V_R(q) = \int_0^\infty \int_{-\infty}^\infty \int_{-\infty}^\infty f(x, y, z) \cdot K_{3D}(q; x, y, z) dx dy dz. \quad (6.3)$$

In conventional soundings where the water distribution is assumed to vary only in z-direction this kernel function $K(x, y, z; q)$ is pre-calculated for both lateral dimensions and yields the sensitivity of the sounding with depth. A synthetic MRS curve is calculated by the multiplication of this kernel function with a depth dependent water distribution (Legchenko et al., 1990).

In extension to this procedure for the assessment of 2D structures the general 3D kernel function is integrated in respect to the direction perpendicular to the profile direction and gives the 2D sensitivity of a MRS measurement.

$$V_R(q) = \int_0^\infty \int_{-\infty}^\infty f(x, z) \cdot K_{2D}(q; x, z) dx dz \quad (6.4)$$

$$\begin{aligned}
 &\text{with} \\
 K_{2D}(q; x, y) &= \int_0^\infty K_{3D}(q; x, y, z) dy \\
 &\quad \partial f(y) / \partial y = 0. \quad (6.5)
 \end{aligned}$$

Here, the water content distribution is assumed to be constant in direction perpendicular to the profile direction, the definition of 2D conditions. This allows the calculation of a synthetic MRS curve by the multiplication of a 2D water content distribution with a 2D kernel function.

6.2.1. Pulse & sounding sensitivity

The spatial distribution of induced signal, i.e. excited Spins is controlled by successively increasing the pulse moment q , usually in some 16 to 24 steps. So for each pulse a specific

6. Application of MRS to 2D water distributions

2D kernel function is given, representing the sensitivity of this pulse moment. In the first three rows of Fig. 6.1 the sensitivities for a coincident sounding in the leftmost column and for loop separations of 24m (1 loop radius), 48m (2 loop radii) and 72m (3 loop radii) in the middle-left, middle-right and rightmost columns are shown, respectively. The first three rows represent the respective 2D sensitivities in dependency of the pulse moment q , having representative values for weak, moderate and maximum possible pulses. As previously mentioned, it shows that in case of coincident loops, for increasing q 's, the induced signal evolves from a region expanding smoke-ring like from shallow below the loop at small pulses towards a large area remote from the loop at high pulses. Separating the loops, the signal evolves successively below the receiver loops. With increasing loop separation, the sensitivity of the respective pulse is successively confined to smaller regions restricted to the receiver loop position.

A MRS measurement consists of a set of logarithmically increasing pulse moments. The total volume sensed by a sounding is consequently the sum of the sensitivities of the pulse sequence. The total sounding sensitivity of a sounding for the given antenna configurations is shown in the bottom row of figure 6.1. From this representation, the pattern of spatially selective sensing of the subsurface by separated loops is immediately obvious. Whereas in case of coincident loops the sounding sensitivity is concentrically spread around the loop center with a symmetry deflection due to electromagnetic effects, decreasing from the loop positions, the sensitivity for separated loops is not symmetric to the midpoint of transmitter and receiver loop, but concentrated to a confined area below the receiver. Changing transmitter and receiver for a given antenna configuration consequently gives different spatial information of the subsurface.

6.2.2. Section sensitivity

A sensible combination of MRS soundings would be a set of loop locations, where adjacent loops half overlap. In the following study a survey with four loop positions with a loop diameter of 48m and two turns each is modeled on a profile striking 45° NE. So the extension of the realized profile from the edge of the first loop to the edge of the last loop covers 120m. The sensitivity of the entire profile is obviously the sum of the sensitivities of all soundings performed along the profile. To assess the improvement of subsurface resolution the profile sensitivity of a survey with these four loop positions is calculated. The total possible spatial information concerning all possible combinations of transmitter and receiver locations, yielding 16 individual soundings (Fig. 6.2, left) is compared to the conventional configuration concerning only the four coincident soundings that are possible with the given loop positions (Fig. 6.2, middle). It clearly shows that the use of all 16 separated and coincident soundings provides a quiet homogeneous coverage of sensitivity throughout the area of loop extension. Here, even the outer regions are sufficiently sensed with a larger sensed volume in south-east due to conductivity effects and the partly geometrical asymmetry in south-north direction. The profile sensitivity of a survey considering only the coincident loop soundings shows a much weaker sensitivity distribution. Not only

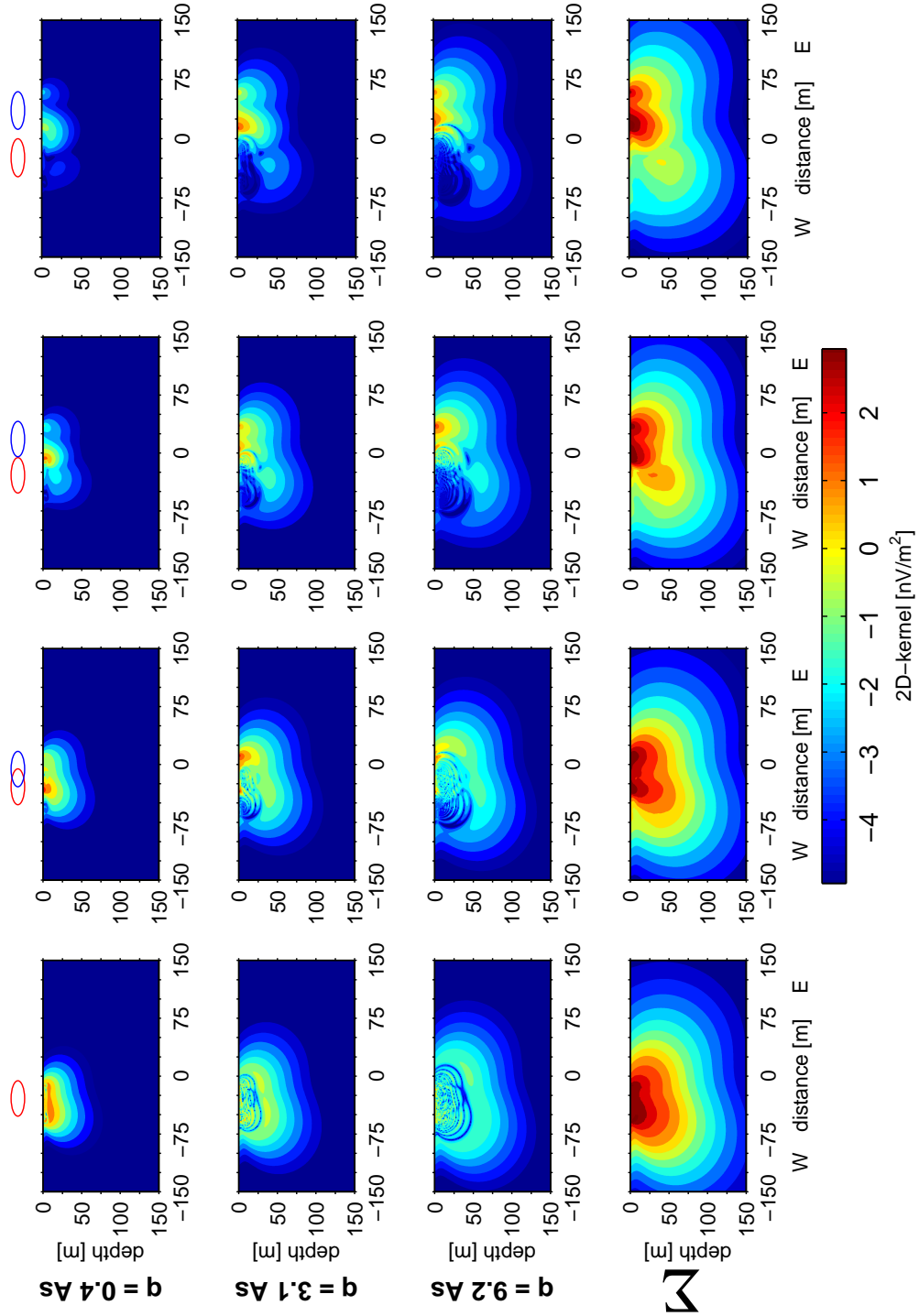


Figure 6.1.: 2D-representation of the spatial sensitivity of MRS soundings with different loop center separations. The first three rows show the sensitivity of three selected pulses, the bottom row shows the sum of all 16 pulses of one exemplary sounding. Loop configuration is 48m circular loop 2 turns, subsurface resistivity of $50 \Omega m$, Earth's field of 48000nT at 65° inclination, profile direction 45° NE.

6. Application of MRS to 2D water distributions

that the total magnitude is decreased, as it is plausible when adding a smaller number of soundings to the total sensitivity, but also a significantly decreased spatial coverage of the subsurface sensitivity distribution is observed. The focus of sensitivity is located just in between the two center loop positions and effectively decreases already at the outer loops. Additionally, the profile sensitivity decrease much faster towards depth than the full survey with 16 soundings. To overcome the discrepancy of comparing a survey of sixteen soundings to a survey with only 4 soundings, the profile sensitivity of a survey with 16 coincident soundings along the same profile extension is modeled and presented in the right plot of figure 6.2. Whereas for the former loop layout a loop center increment of 24m i.e. one loop radius is modeled, a loop center increment of 4.8m, i.e. $1/5$ of a loop diameter is needed to cover the profile with 16 individual loop positions. With such a loop layout, the total sensitivity coverage can be increased to magnitudes somewhat larger in the center of the profile than 16 separated loop soundings. However, even here we find a much less homogeneous coverage of the subsurface and no significantly higher resolution in depth. The large maximum magnitudes are mainly due to the large recorded amplitudes at small pulses for coincident soundings and does not necessarily mean a better differentiation in recorded sounding curves as will be show in 6.3.2.

In practice a survey with 16 different loop positions means a much higher work load than only four positions and mutual permutation. Additionally the complete separated loop survey can be measured by performing soundings at the 4 positions one after the other to transmit the pulses and recording the signal at all four positions as receiver simultaneously. This procedure yields 16 soundings in the same survey time as four coincident ones. Since such a multichannel receiver technique is already envisaged by MRS developers, the following study restricts to a comparison of resolution enhancement by the use of full separated loop sounding information and conventional coincident loop surveys. So, the study can be seen as a strong pleading for the use of multichannel MRS surveys for the study of 2D water content distributions.

6.3. Synthetic data

6.3.1. Aquifer models

To assess the effective effort in subsurface structure resolution by the use of separated loop surveys a synthetic survey with four loop positions in the above mentioned configuration is modeled. Models were assumed as follows:

1. One aquifer with constant upper boundary at 6m ($1/8$ loop diameter) and a lower boundary with a slope that increases within a distance of 72m (1.5 loop diameters) from 12m ($1/4$ loop diameter) down to 36m ($3/4$ loop diameter). Aquifer water content is 25% and 5% elsewhere (6.3 a).

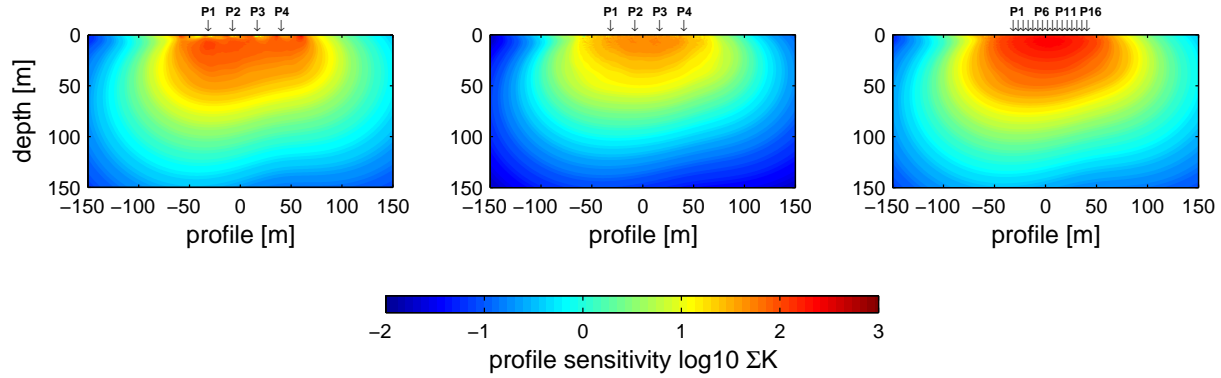


Figure 6.2.: 2D profile sensitivities for surveys with 16 separated and coincident loop soundings at 4 antenna positions (left), 4 coincident soundings at the same loop positions (center) and 16 coincident loop soundings at individual positions spread on the same profile extend than left (right). Modeling was performed for circular loops of 48m diameter on homogeneous half-space of 50om and Earth's field of 48000nT at 60° inclination, profile direction is 45° NE.

2. One water bearing lens centered below the midpoint of the loop layout with an extension of 72m (1.5 loop diameter), a maximum thickness of 24m (1 loop diameter) and a center depth of 24m (1/2 loop diameter). Water content in the lens is 25%, 5% elsewhere (6.3 b).
3. Two water bearing lenses. One small lens of 48m width (1/2 loop diameter), maximum thickness of 6m (1/8 loop diameter) in a depth of 12m (1/4 loop diameter) located below the middle-left loop. One slightly bigger lens of 48m width (1/2 loop diameter), maximum thickness of 12m (1/4 loop diameter) in a depth of 24m (1/2 loop diameter). Water content within the lenses is 25%, 5% elsewhere (6.3 c).

Model body extensions are chosen in parts of the loop diameter in order to provide scalability of model and loop geometries to different dimensions. The relative model resolution is about linearly scalable but the total sensitivity unfortunately not. The total recorded signal decreases about quadratically with the loop surface. So even if a high resolution to small and shallow structures can be achieved by the use of small loops, the recorded signal rapidly falls below reasonable signal to noise ratios in real field surveys. For large scale applications the depth resolution does not linearly scale with loop size but the shallow resolution is still given.

In order to evaluate the quality enhancement in data interpretation a generic optimization algorithm of MATLAB was applied to reconstruct the model from a set a sounding curves. This algorithm uses a non-linear large scale Gauss-Newton optimization scheme to find a model that fits all given sounding data best. Effective model smoothing is implemented by a L1-norm regularization. To obtain sufficient data accuracy the computation of synthetic

6. Application of MRS to 2D water distributions

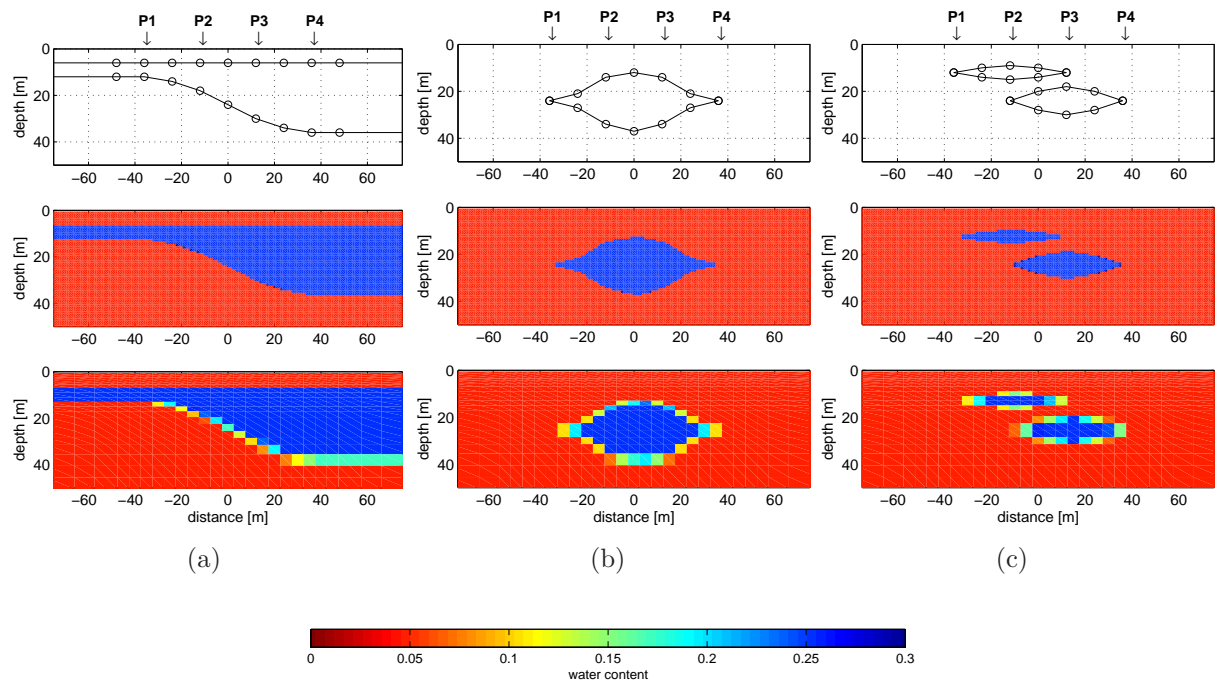


Figure 6.3.: Models of the three aquifer types under study. Top figures show the model boundary nodes, middle the water distribution in the fine grid for forward modeling, bottom the corresponding water distribution in the recoarsed grid for inversion.

sounding curves is realized on a regular 1x1m grid from model geometries given by discrete vertices. However, the given grid is much too fine to be suitable for model reconstruction by an optimization algorithm. Therefore the grid is re-meshed on a coarser one with increasing model block size towards depth and outside the loop coverage to take the effective sensitivity into account. The limiting vertices as well as the fine model grid and the recoarsed grid to be recovered are shown for the three studied models in Fig. 6.3. Even though the model blocks for the forward modeling have discrete water contents of 25% or 5% the ideal model to be reconstructed by the optimization algorithm shows transitions between the two water content levels where only part of the coarse grid is filled by cells of high water content. The chosen procedure is closely linked to real conditions where true subsurface structure boundaries do not match the model discretization by which they are rendered.

Figures 6.4 - 6.6 show the results for the three models under study. For the assessment of different inversion strategies in the course of this section a common representation for all datasets is chosen. The first model represents the 2D water content distribution obtained from the inversion of all possible coincident and separated loop soundings, the second one gives the model obtained from only the four coincident loop soundings. The third model represents the pseudo 2D contour representation of the 1D inversion of the single coincident soundings given in the fourth model. On the right hand side the synthetic sounding curves for the two 2D models are displayed. Each row contains all soundings for one individual receiver position, each column contains all soundings for one individual transmitter position. By this way a matrix of soundings clearly arranges the representation of the data of the full survey. The coincident soundings are the soundings with equal transmitter and receiver position numbers on the diagonal. Here, blue and red lines represent the synthetic sounding curves according to the two 2D inversion results, respectively. Since only noise free synthetic data are used for inversion, the recovered data are very close to the initial data points of the synthetic model. So, for a better readability of the sounding details the original data are not shown. The blue lines show the synthetic data according to the model determined by all sixteen separated and coincident soundings, the red lines show the synthetic data according to the model that was reconstructed using only the coincident soundings. Here, the optimization algorithm determines a model by fitting only the coincident loop soundings on the diagonal of the sounding data matrix. However, based on this model all loop configurations are forward modeled to underline the differences in separated loop sounding curves between the two models. Since the deviation of both soundings is quite small for noise free data, the difference multiplied by a factor of 10 is additionally displayed as green line.

Comparison of inversion results of the full 16 sounding survey and the reduced 4 coincident loop survey for model 1 shows that in both cases the initial model body is reliably reconstructed. The model misfit to the initially given model is slightly smaller for the upper inversion result. Also less variation of water content within the intrinsically homogeneous water layer is observed, as well as in the upper low water content zone. However, no significant differences in the general reconstruction of the water body is observed comparing the two models. Regarding the corresponding soundings curves, it is obvious that for both

6. Application of MRS to 2D water distributions

models the coincident soundings on the diagonal are nearly equal. Only the coincident sounding at P4 shows a slight deviation. Thus, that both models are equivalent for the sounding curves of the coincident soundings. So, additional information on model resolution is gained by the consideration of the separated loop soundings, displayed in the graphs apart from the diagonal. Since the quite smooth model is well reconstructed by both the full MRS survey and the reduced coincident survey, the differences are still quite small. This changes regarding the second model with smaller dimension of the anomalous body in Fig. 6.5. The two inversion results, as in the former example based on all sixteen soundings and on only the 4 coincident ones show larger differences. In the second model, the lens body is reliably recovered, but shows a less sharp resolution of body boundaries compared to the first model. The distribution of the surrounding homogeneous background water content is also less properly met. Also for this example, the coincident soundings show only a vanishing difference whereas the non-coincident soundings apart the diagonal differ significantly. Enhancement of model resolution is consequently gained by the use of separated loop soundings. Interesting to note is also the comparison of single 1D inversion of the coincident sounding and their pseudo 2D contour representation. Whereas for the dipping aquifer case, the model boundary and location can be roughly interpreted from these data, the lens in model 2 cannot be recovered appropriately. Similar results are observed for model 3 with two separated lenses. Here, both lenses are basically recovered by the two 2D inversion results, but boundary sharpness is significantly improved by the use of the information from separated loop soundings. The 1D inversions and their contour representation, however, fit this small scale model better than in case of one larger lens in aquifer example 2. The ability to render a 2D structure by 1D soundings is obviously not a simple function of anomaly size in relation to the loop size.

Throughout the shown investigation profile like surveys including the information from separated loops provides superior model resolution for small scale structures. For subsurface structures with a smooth variation compared to the loop sizes, this effect is less prominent. However, for small scale variations the incorporation of all possible loop permutations as transmitter and receiver provides a significantly improved model reconstruction compared to a conventional coincident loop survey with the same antenna locations. In case of the proposed multichannel recording for several receiver loop positions simultaneously will provide the complete separated loop survey in the same recording time as only the coincident one. Even if single receiver systems are used the additional work expense might be worth it if high resolution prospecting is needed. The given study shows only the fundamental increase in subsurface resolution for ideal noise free data. For real conditions with limited signal to noise ratio the resolution improvement will be significantly higher since the model equivalence increases with decreasing data quality. Here the advantage of enhanced spatial coverage of the subsurface signal response in multiple MRS measurements will be even more important.

The accuracy of model recognition by an inversion scheme is quite difficult to quantify. The model-misfit as given for the inversion results in the former three examples gives an integral value of the differences between initial and recovered models. However, this value

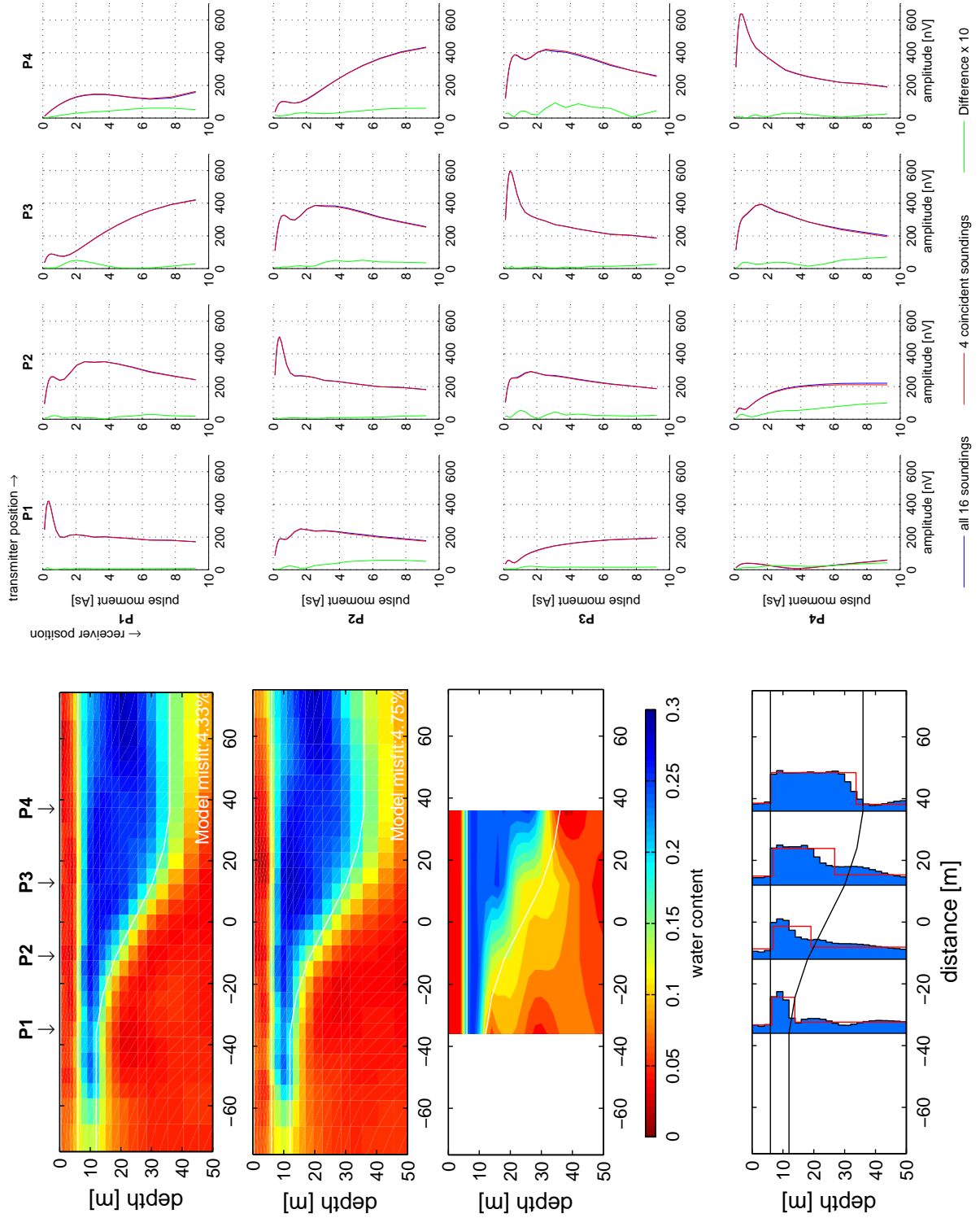


Figure 6.4.: Inversion results for the model of a slowly dipping aquifer.

6. Application of MRS to 2D water distributions

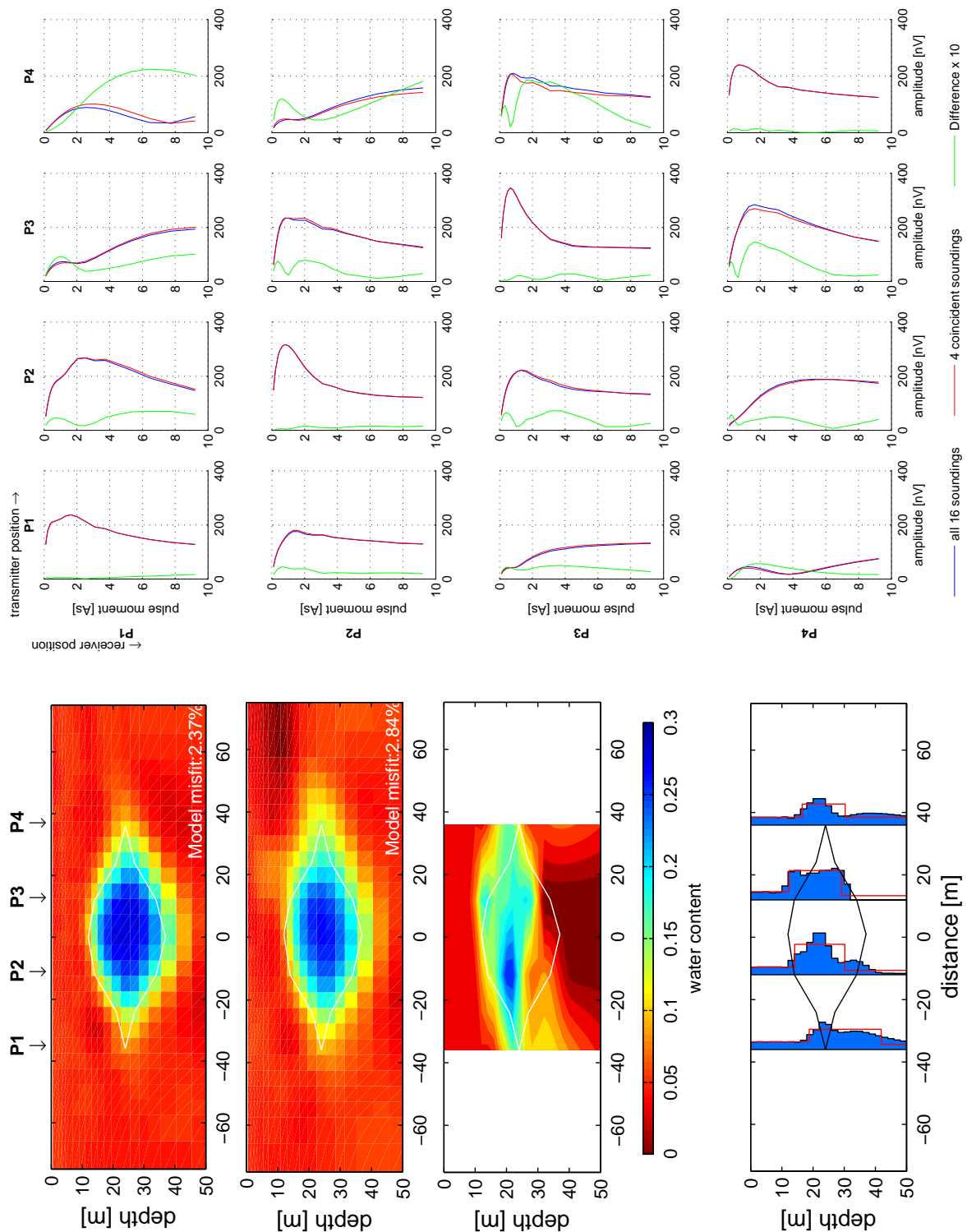


Figure 6.5.: Inversion results for the model of a large water bearing lens.

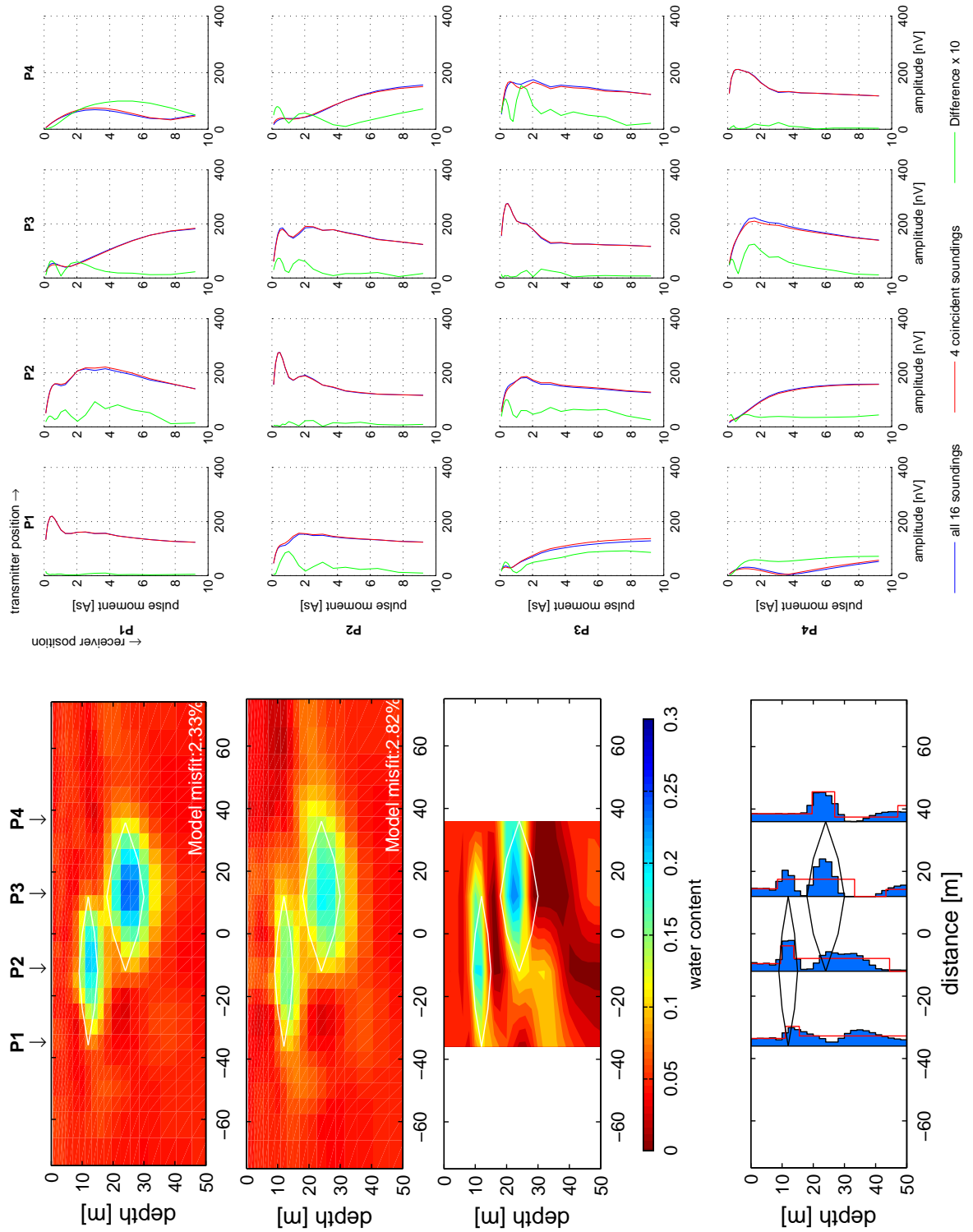


Figure 6.6.: Inversion results for the model of two small lenses at different depth and locations.

6. Application of MRS to 2D water distributions

is not necessarily representative for the rendering of the model body boundaries. Also the data misfit between initial and reproduced soundings is no adequate measure since it is quite small for synthetic data and reaches the same range even for equivalent models that do not appropriately reproduce the initial model. So, as an additional estimate for inverted model accuracy we show the residuals, the difference between the initial and the inverted model. Fig. 6.7 shows the residuals for the three aquifer models in columns, in top row for the inversion with all sixteen coincident and separated loop soundings, in the bottom row only for the coincident ones. The white lines represent the initial model body boundaries. Throughout all models one observes overestimated water contents outside the model boundary and underestimated values right inside the model boundary. This is an expected result since a model smoothness regularization is used that constrains the model boundary sharpness. However, differences in residuals are observable for the different data sets used for each aquifer type. In the smoothly dipping aquifer model the differences are quite small. But still the residuals are slightly smaller in the region above the aquifer itself and within the aquifer too. The previously outlined better model body recovery for the large water lens is found also in the residuals (middle column). Here the error in water content recovery is in general smaller throughout the model body if all available data are used for inversion. Furthermore the residuals for the reduced data set for this aquifer type are significantly larger in the zone above the model body, especially in the right upper region. Even larger differences in residuals are observed in the third aquifer model, the two small lenses. Here residuals are quite large all over the region around the model bodies if case of a coincident loop sounding inversion. Including all soundings, the model resolution is significantly better and residuals effectively reduced to the given model body boundaries. The differences in residuals for the latter two cases are not constrained to the direct vicinity of model body boundaries. So the improvement in model recovery is not an effect of regularization, being differently effective on different data density, but is a real gain in subsurface resolution.

6.3.2. Ice-ridge

The model of an ice ridge was triggered by the discussion with geophysicists investigating the arctic ice cover thickness. Since hydrogen protons in frozen water don't contribute to the MRS signal, it seemed to be a favorable technique for the given tasks. The question was whether MRS is suitable to render the thickness of sea ice in the range of about one meter and to resolve changes in the ice thickness. Some exemplarily modeling showed that neither the conventional technique of MRS with coincident loops nor surveys with separated loops are able to render such shallow structures with a reasonable loop size. Only in the particular situation where ice tectonics builds up ice ridges with accumulated ice thickness of up to five meter and more, MRS provides sufficient resolution to recover the internal structure from profile like separated loop measurements. Even though this model where the major part of the subsurface has 100% water content is not representative for most geological settings where MRS is applied, there are some special features of separated

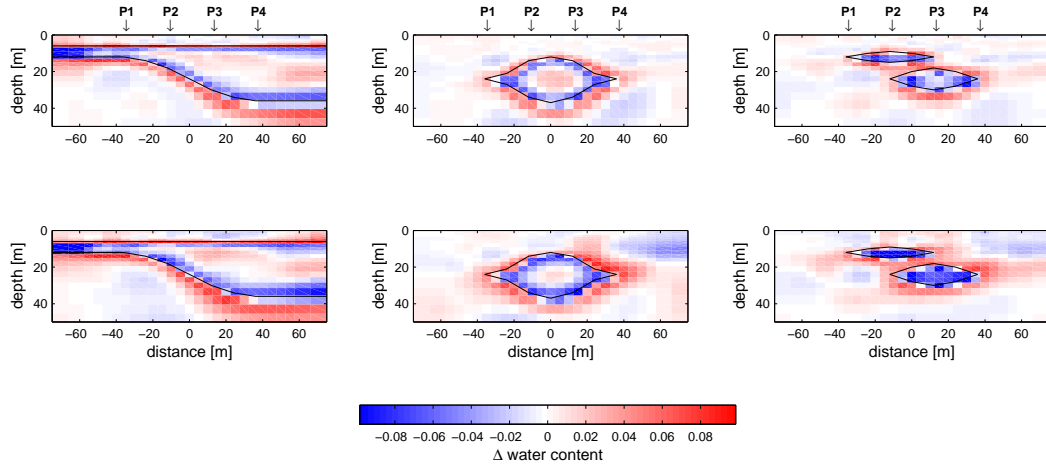


Figure 6.7.: Residuals of the inversion results for all available sounding data (top row) and for only the coincident soundings concerned (bottom row).

loop MRS surveys that can exemplarily pointed out.

The ice thickness as it is usually found in the arctic sea during the winter has a thickness of about 1 meter. The model of an ice-ridge was assumed according to ice-thickness measurements by boreholes as an ice accumulation over a distance of sixty meters with a maximum thickness of 5 meters in the center. The average water content of the accumulated crushed ice was set to 10%. In figure 6.8 the initial model of a sample 1m ice cover, the assumed ice-ridge below ice cover and the discretization of the ridge model as it is found after re-coarsening the grid for inversion is shown. The corresponding sounding curves are shown beside as blue lines for the homogeneous ice cover and red lines for the ice-ridge. Looking closer to the synthetic sounding curves of the coincident soundings P1/P1 to P5/P5, differences can only be observable within the very first data points. From about 0.3 As on both curves are practically identical. Here, separated loop soundings show quite different pattern. Differences of both curves appear in the complete sounding curve. For half overlapping soundings (e.g. P2/P1) both curves are separated from the first pulse moment on. They differ in the first quarter of the curve up to some 20% and converge smoothly towards high pulses. For edge-to-edge soundings (e.g. P3/P1) the difference of both curves even increases during the whole sounding and reaches its maximum, also of some 20% difference, at highest pulse moments. Since for coincident soundings a shallow structure as the ice ridge is represented only in the very first data points no suitable rendering of such shallow model body is expected. Limiting the maximum pulse-moment to a smaller value and space the set of pulses to that range doesn't really improves the result because the sensitive area of coincident loops quickly spreads beyond the investigated target and doesn't allow a high resolution of the shallow region below the loop. Down-scaling of the loop size is also quite limited since the magnitude of the response signal scales with about

6. Application of MRS to 2D water distributions

the square of the loop surface. So, recorded signals rapidly fall below a suitable signal to noise ratio. For this kind of application, separated loop surveys turn out to win the game. As previously studied Hertrich et al. (2004) the sensitivity of separated loop soundings is successively confined to a shallow volume below the receiver loop with increasing pulse moments. Another point predicted from synthetic modeling of 2D sensitivity for separated loops can be easily recognized here. In case of separated loops the major part of the MRS response signal in the receiver is induced from an area below the half of the receiver loop opposite from the transmitter. This leads to a surprising symmetry in the MRS survey data. For example on receiver position P2 (second row), a larger deviation between ridge model and homogeneous ice cover is observed in case of the transmitter located at the side apart from the ridge compared to the transmitter position towards the ridge. This is even better visible by comparing sounding curves P2/P4 and P3/P5. Both soundings are edge to edge soundings. In the former example transmitter and receiver cover the extend of the largest ice thickness. However, moving both loops along the profile where the ice volume decreases, the effect of water substituted by ice in the sounding curve increases. In the latter case a bigger part of the ice ridge is sensed by the sounding even though the ice volume under and between the transmitter and receiver is smaller.

Looking on the inversion results in figure 6.9, the latter sensitivity considerations can be observed in the model adaptation of the inverted soundings. All three inversion strategies are able to recover the basic structure of the ice formation more or less adequately and the thin, dry, ice layer is not seen in one of the results. The effort of separated loop soundings appears, as in the previous examples, in the much better rendering of the boundaries of the model body. Recovering the lateral extension of the model block, one would underestimate its size in 2D inversion with only the coincident soundings and would overestimate it from 1D inversion and its pseudo-2D contouring of the same data set. Using all 16 separated and coincident soundings finally leads to a quite satisfying rendering of the initial model body. Note that the model adjustment is performed with noise free data only. The effect of a significantly larger number of points being affected by the shallow water content anomaly in the separated loop soundings compared to the coincident ones will be of even larger importance when noise affected data are used for inversion.

The given example shows that the use of separated loops launches new applications in high resolution mapping of water content, where conventional coincident loop soundings alone do not provide sufficient spatial resolution.

6.4. Real data

Exemplary MRS surveys on 2D targets have been acquired with coincident and separated loops over small confined structures in France and Germany. Results are carefully investigated similar to the synthetic assessment of the previous chapter and the results are correlated with additional geophysical and geological data.

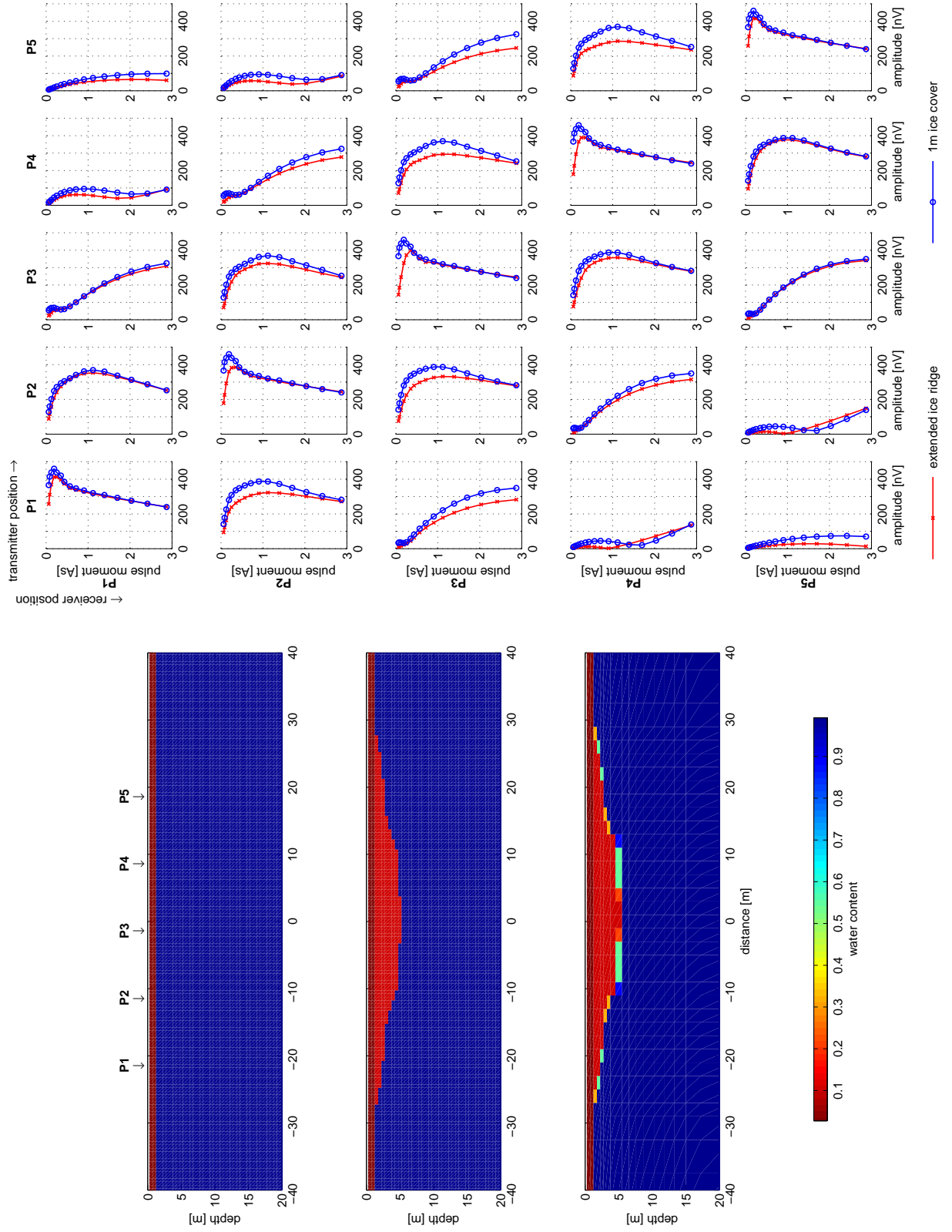


Figure 6.8.: Left: models of a 1m ice cover (top), ice cover plus an extended ice ridge with up to 5m thickness (center) and the ice ridge model recoarsed to a generalized grid for inversion (bottom). Right: Corresponding sounding curves for the models of ice cover and ice cover plus ice ridge. 79

6. Application of MRS to 2D water distributions

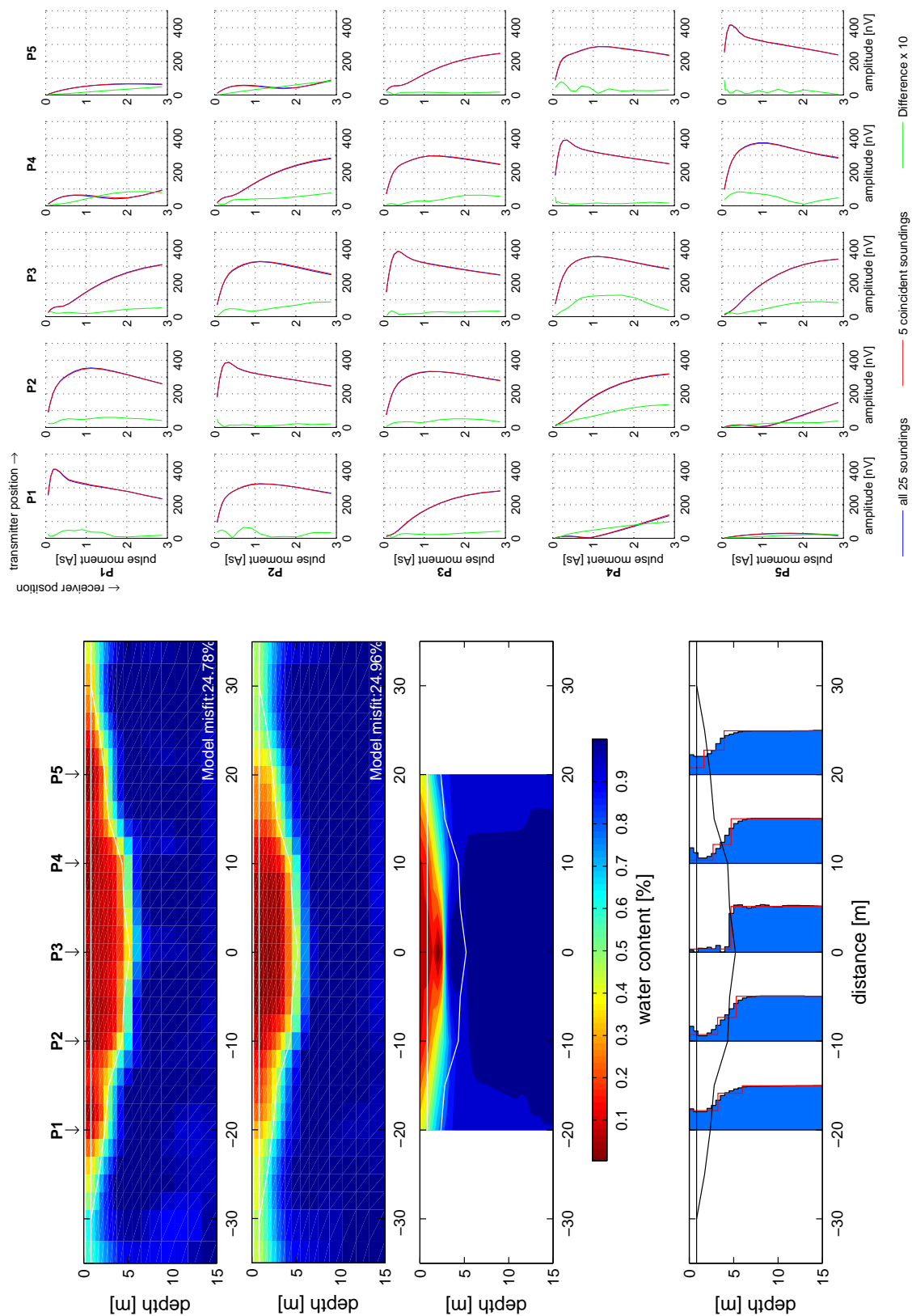


Figure 6.9.: Inversion results for the model of the ice ridge.

6.4.1. Nauen, Germany

The survey in Nauen was performed on a well investigated test site, where a variety of additional data are available (Yaramanci, Lange, and Hertrich, 2002). From previous surveys a shallow aquifer from about 2m down to some 20m is known, that slowly crops out towards the surface. From geoelectrical and radar sections the upper boundary of the clayey aquiclude is known. However, the deeper structures are neither visible in radar-section nor can they be interpreted by a resistivity contrast. The MRS survey was designed to cover the outcrop of the aquifer and spread towards the as aquiclude assumed direction. There, previous individual MRS measurements did already point to larger water contents than they were presumed from geoelectrics and geological conditions. The survey was performed as in the synthetic examples with 4 individual positions of loops with 48m diameter, adjacent half overlapping. All sixteen possible permutations of transmitter and receiver positions have been realized. The analysis of the the given dataset with the introduced optimization algorithm has been performed, as displayed in figure 6.10. Inversion results of the full coincident and separated loop data set are displayed in the upper plot on the left hand side of the figure. Using only the 4 coincident soundings yields the second model and the individual 1D coincident sounding inversions as well as their pseudo-2D contour representation are shown in the plots below. In the sounding data matrix on the right hand side the modeled data (blue and gree lines) are plotted in comparison to the measured ones (red circles). The blue lines show the data adaptation concerning all 16 soundings. The green lines are calculated from the model that has been reconstructed by using only the 4 coincident soundings. The deviation between both therefore shows the gain in model resolution by fitting all available data.

The found model represents the presumed outcropping aquifer on the lefthand side around P1. Its boundary obviously crops out at around P2 with an immediate transition into a second undulating water bearing layer towards north-east. Both structures have their lower boundary at a layer of very low water content at some 20m. Below this zone a second aquifer appears at some 40-50m depth. The lower boundary of the low water content zone shows a significant depression at around +20m on the profile. The trisection of the section into a first aquifer, aquiclude and second aquifer can be roughly estimated from the 2D inversion using only the coincident soundings as shown in the second model in the left hand side of the figure. A resolution of a depth variation of layer boundaries or a discrimination of structures within the layers is, however, not given. The single 1D inversions and the pseudo-2D plot do also just roughly show the structure of a low water content layer between two aquifers but does not reflect the structure of this body as it is rendered by full 2D inversion of the complete dataset.

Comparison of inversion results of MRS and DC-geoelectrics in figure 6.11 shows the correlation and contradiction of both methods. From the local geology and data from a nearby borehole data a shallow aquifer is known outcropping at around +12m on the profile, near P3. This aquifer is topped by a vadose zone of some 2m and confined to depth by a till layer. This layer sequence is well recovered in the inversion results. The vadose zone ex-

6. Application of MRS to 2D water distributions

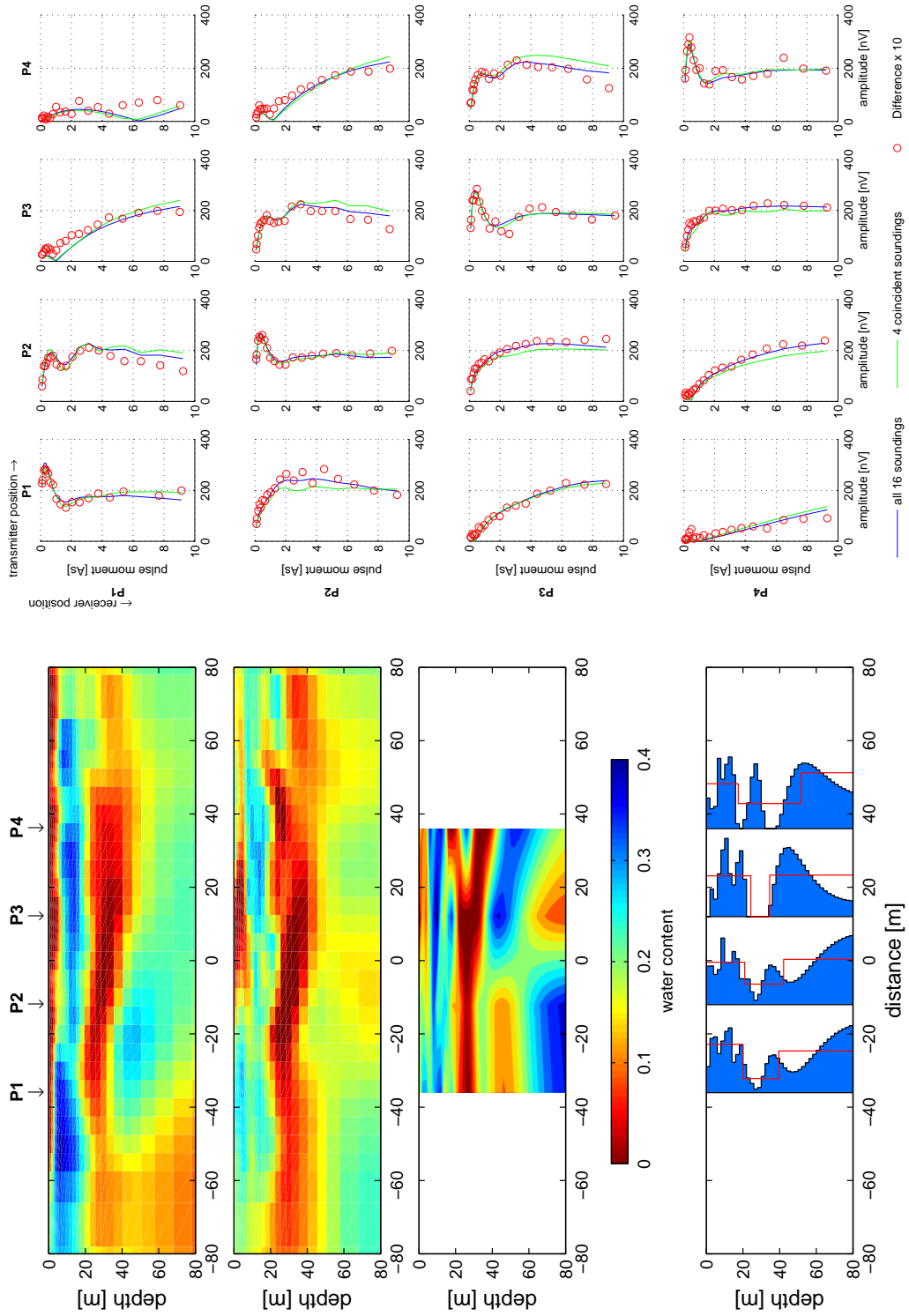


Figure 6.10.: Inversion results of different inversion of MRS data at the Nauen test side and the corresponding measured and calculated soundings. Left hand figure shows 2D inversion results for 16 coincident and separated loop soundings (top), only the 4 coincident soundings (middle) and the individual 1D inversions (bottom). Right hand side shows the respective real and synthetic soundings for the 2D models on the left.

tends from the SW edge of the DC profile up about +15m near P3. The aquifer with resistivities of approximately $300\Omega m$ slowly decreases in depth from about 12-15m depth to the surface. It also crops out near P3. The boundary of the aquifer, consisting of conductive till is represented by resistivities of some $50-150\Omega m$. In the resistivity section the north-eastern part of the sections shows only slight resistivity variations between 50 and $150\Omega m$, no further layer stratification can be recovered. The MRS inversion result represents the structures found in DC inversion appropriately. The shallow outcropping aquifer is found by high water contents of around 30% and above, the vadose zone and the till layer close to the surface are recovered with vanishing small detectable water. However, the lateral zoning of the shallow aquifer is not well resolved. The high yield aquifer is only slightly intersected in NE-direction towards a second aquifer that occurs from about 10 to 20 m depth from around P2 towards NE of the profile. Additionally we find a very prominent zone with water contents close to zero along the whole profile ranging from 30 to 45m depth, with a depression down to around 50m below P5. Both, the second aquifer and the low water content zone are not shown in the resistivity section at all. This corresponds to previous results from borehole data and DC-soundings (Yaramanci et al., 2002) in about 200m distance from P1, where a second aquifer is indicated in borehole data, but no resistivity changes in depth are observed by Schlumberger soundings. In this case the 2D interpretation of MRS data unambiguously yields subsurface informations that are not found in conventional electrical data. So, the combination of both methods shows significant enhancement in hydro-geophysical interpretation.

6.4.2. StCyr en Val, France

On a test site close to Orleans, the first assessment of the feasibility of separated loop soundings was conducted. On this location the geological setting is given by a sandy aquifer below clayey coverage on the quaternary river banks of the Loire river. From a resistivity section a 2D structure is interpreted, showing a low resistivity anomaly pointing to a clayey filled channel. Over this structure a survey with 3 loop positions with 48m diameter each, half overlapping as in the previous studies was realized. The signal to noise ratio was limited due to a nearby gas pipe. However, 8 out of 9 possible soundings at the three loop positions were realized. Here, a model from all available soundings was determined by 2D inversion and compared the 2D-inversion result of coincident soundings only and to individual 1D inversions of the coincident soundings. Results are shown in figure 6.12. Inversion results for both loop configurations show a zone of high water content ($\sim 15-20\%$) from left of P1 slightly dipping towards P2 and P3. However, the model considering the full dataset, shows a prominent zone of low water content down to some 3 to 5m between P1 and P2 and a zone of decreased water content between P2 and P3 down to a depth of 40m. Lower water content between P1 and P2 and a deeper upper boundary of the high water content zone are also visible in the second inversion result. But the entire structure is not as sharply defined as in the first model. The 1D inversions do roughly fit to the found structure representing a prominent layer with increased water

6. Application of MRS to 2D water distributions

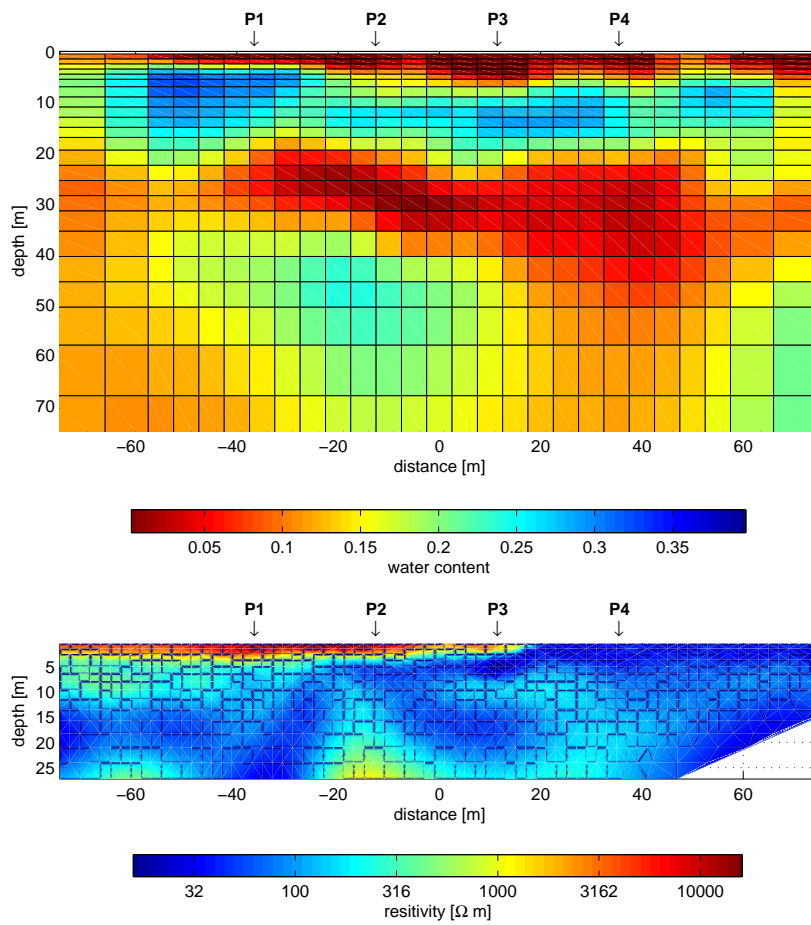


Figure 6.11.: Comparison of the inversion results from MRS (top) and resistivity measurements (bottom). Depth axes are equally scaled to provide comparability.

content successively increasing in depth and decreasing in water content towards P3.

Comparing the inverted 2D water distribution to the resistivity section on the same profile in figure 6.13, the structures of high water content can roughly be related to structures with low resistivities and vice versa. However, the sharply confined area with very low resistivities, the presumed clayey filled channel, is not appropriately recovered in the MRS inversion result. Well defined in the MRS data is the increase in clay cover thickness at around P1 towards P2. From the resistivity section one would expect the high conductivity structure between P2 and P3 down to a depth of some 25m to be recovered in the MRS inversion result. A slight decrease in water content is indeed observed, but the structure is not well represented. Beside a limited data quality, maybe causing low resolution, the dimension of the structure is assumed to cause this effect. In a later survey two parallel profiles to both sides of the initial profile, respectively, and one profile perpendicular to the others in the assumed strike direction and above the center of the channel were acquired. The three dimensional arrangement of the inversion results is displayed in Fig. 6.14. The sections clearly show that the channel is indeed not a 2D structure, but ranges from a wide shallow structure North-West of the center profile to an even deeper and branched system of low resistivities towards South-East. The red circles plotted above the profiles mark the positions and extend (48m diameter) of the MRS loops. They cover the conductive structure in the extend where no 2-dimensionality can be assumed. On the one hand this means a drawback in rendering the structure as it is found from the center geoelectric profile. On the other hand it underlines the spatial sensitivity of the MRS method and encourages to even lateral extensive measurements for the rendering of 3D subsurface water content distributions.

6. Application of MRS to 2D water distributions

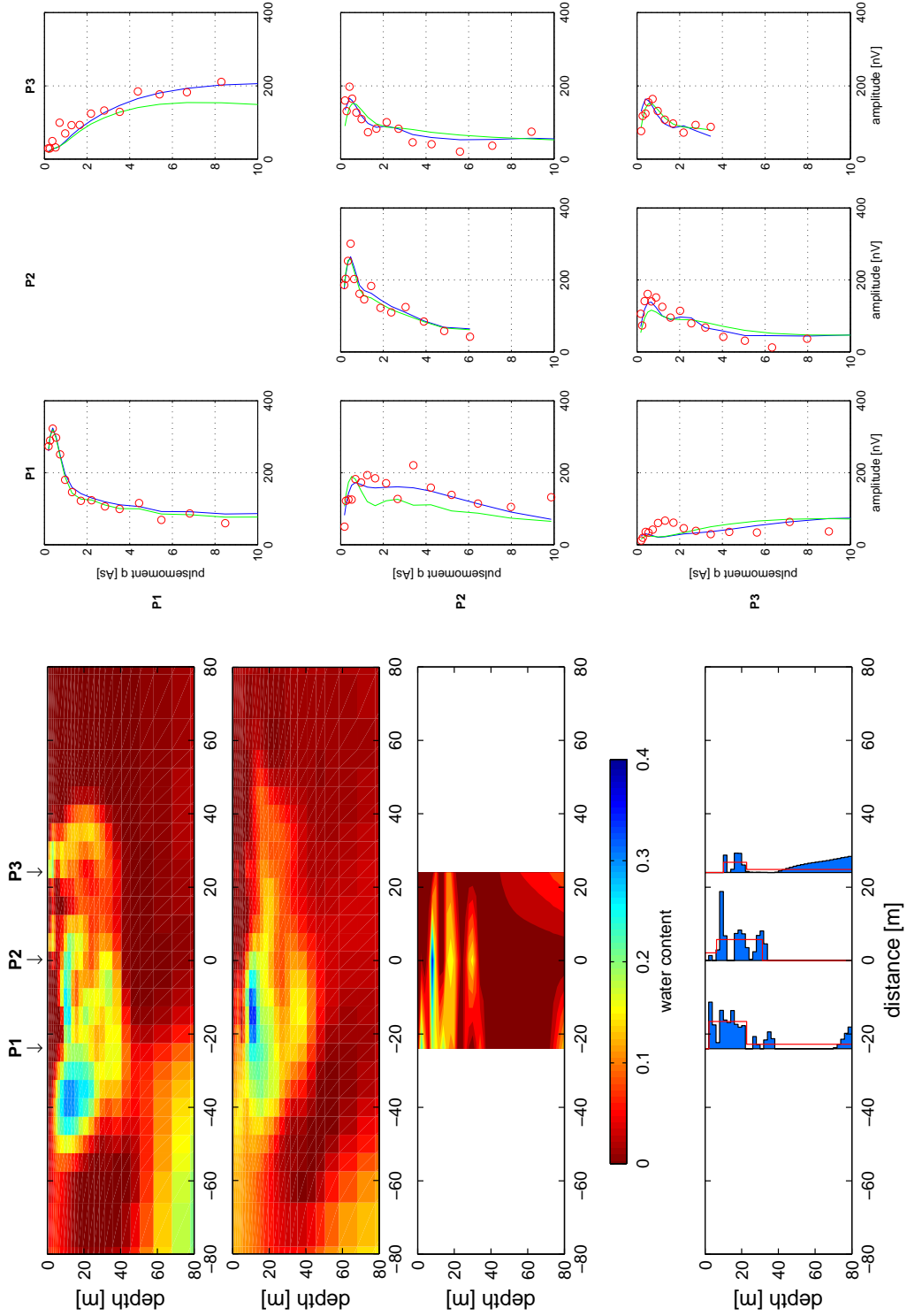


Figure 6.12.: Inversion results of different inversion of MRS data at the StCyr en Val test site and the corresponding measured and calculated soundings. Left hand figure shows 2D inversion results for 8 coincident and separated loop soundings (top), only the 3 coincident soundings (middle) and the individual 1D inversions (bottom). Right hand side shows the respective real and synthetic soundings for the 2D models on the left.

6.4. Real data

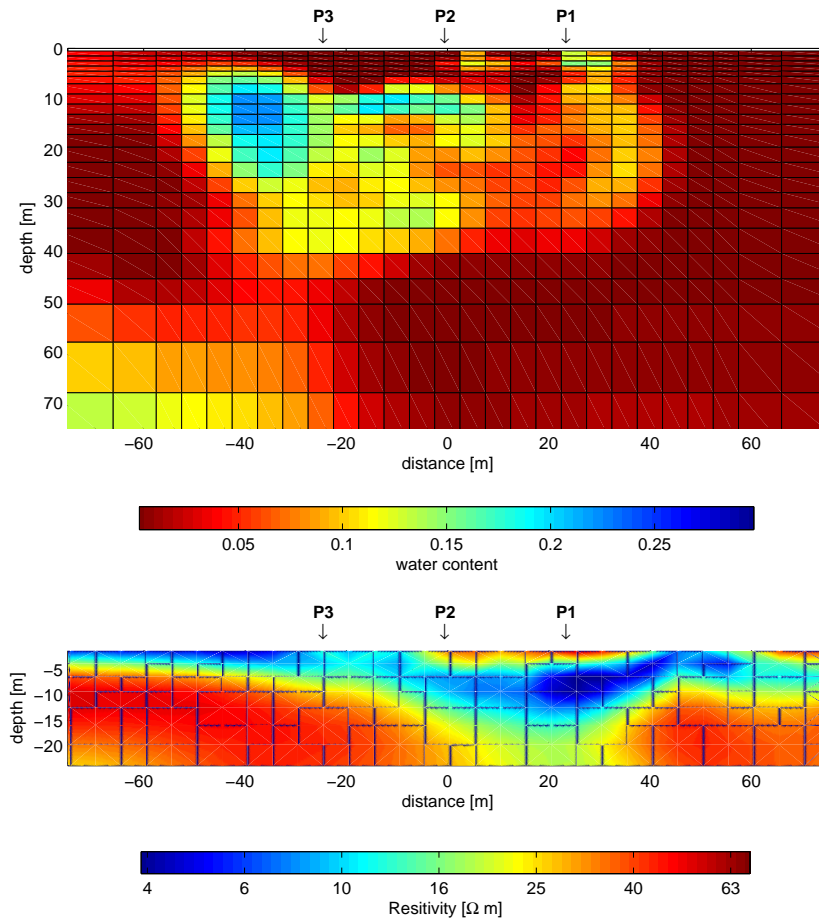


Figure 6.13.: Comparison of the inversion results from MRS (top) and resistivity measurements (bottom). Depth axes are equally scaled to provide comparability.

6. Application of MRS to 2D water distributions

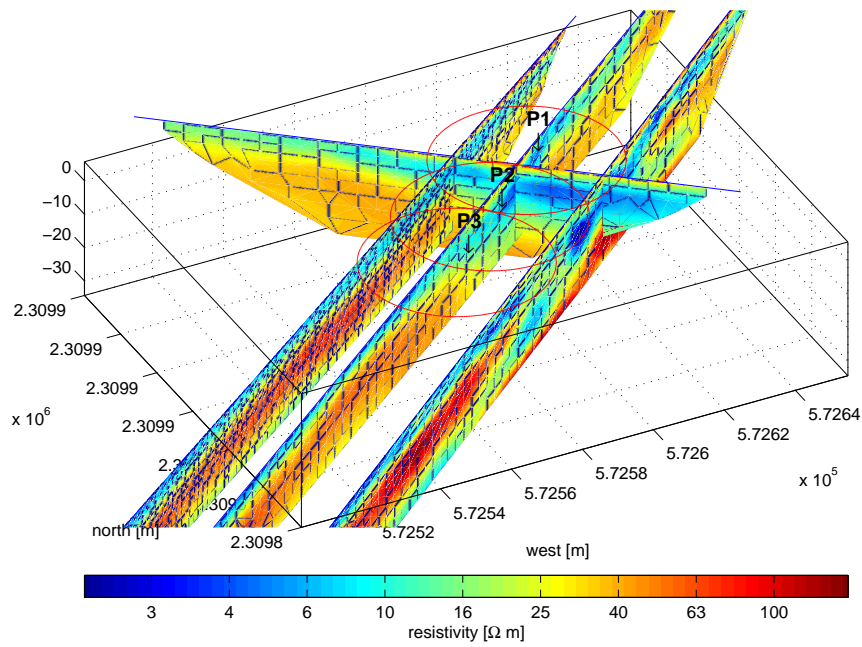


Figure 6.14.: Three dimensional arrangement of the set of DC-resistivity profiles acquired around the assumed clay filled channel in StCyr en Val. Axis labels are in absolute UTM coordinates. The red circles mark the position and extend of the MRS loops.

7. Conclusion

In the course of the present work it has been shown that the extended formulation of the MRS response correctly describes configurations with individual loops for transmitter and receiver. The innovation of the treatment is the consideration of a fixed geometrical relation of the Spin precession and the magnetic fields it interacts with. The mutual orientation of the transmitter and receiver fields and their orientation in respect to the Earth's magnetic field gives rise to a complex valued scaling factor. Hence, a geometrical phase of the MRS signal occurs for non-coincident transmitter and receiver loops. Additionally, the influence of Earth's conductivity on the electromagnetic fields, individually for transmitter and receiver, determines the distribution of spatial sensitivity and sounding curve pattern.

It has been demonstrated on calibration soundings that the separation distance and the separation direction of transmitter and receiver loops determine the pattern of the MRS sounding curve, in particular the signal phase. In comprehensive synthetic modeling it was demonstrated that reasonable signal amplitudes can be recorded for a quite wide loop separation. Only a slight loss in maximum signal amplitude is observed for loop separations up to one diameter, e.g. edge-to-edge layout. For larger separations the signal amplitude decreases significantly, at least for the presently available pulse power.

The study of 1D kernel functions demonstrates that for increasing loop offsets the major part of signal contribution is located in shallow regions and significant variations in the ratio of real and imaginary parts of the subsurface sensitivity are observed, corresponding to a variation of the observed signal phase.

More detailed information about the spatial origin of the MRS-signal are obtained by the introduction of 2D kernels. Recapitulating the characteristics of spatial signal contribution of the 2D kernels in section and map view it turns out that the use of separated loops leads to a significantly different spatial sensitivity compared to conventional coincident loop soundings. For the case discussed of edge to edge layout of the loops, the contributing signal is confined to a small volume at shallow depth, associated to the location of the receiver loop. Even though only a small part of the totally induced signal radially around the transmitter can be sensed by the receiver, reliable signal amplitudes are recorded. Thus, the use of separated loop leads to a significantly increased spatial resolution at signal amplitudes comparable to coincident loop soundings of equal loop size.

The systematical illustration of the origin of the MRS signal and the corresponding sounding curves bears a quite unusual feature for geophysical methods. In contrary seismic, resistivity or EM methods, for a given loop configuration, the response signal is not equal

7. Conclusion

if transmitter and receiver loop are reversed. In general the recorded soundings will have, partially significant, differences for a reciprocal arrangement. The reason for this effect is that it is the perpendicular component of the induced loop fields that enters the MRS signal response. This perpendicular component is in general asymmetric in the subsurface due to oblique inclination of the Earth's field. Additionally the reverse elliptical components of the transmitter and receiver fields differently enter the MRS signal response and cause, in case of conductive ground, an asymmetric distribution of the respective components in the subsurface. The only scenario to obtain perfectly reciprocal soundings with reverse transmitter and receiver loops is in case of a perfectly 1D stratified Earth at the magnetic poles. The reciprocity of loop reversion is also recovered for exact east-west separation if the inclination direction is simultaneously reversed, i.e. on the opposite hemisphere. In all other cases the separation direction in respect to the inclination has to be carefully accounted to correctly interpret separated loop measurements. Accurate comprehension of this complex valued scaling part is therefore of an extreme importance and has to be regarded for each individual loop configuration to correctly interpret the lateral Spin variation from MRS measurements. For the design of new loop configurations for a specific focused resolution, the geometric dependency of this part on the loop configuration is the most important parameter to assess.

In an exemplary field survey it has been shown that the sounding curve patterns for separated loop measurements are correctly described by the extended MRS formulation based on elliptical decomposition and regarding the complex geometric kernel part. Furthermore the field data indicate the high sensitivity to variations in the water content at shallow depths.

In the course of the thesis it is demonstrated that profile like MRS surveys are suitable to render 2D water distributions in the subsurface. It is pointed out that the use of separated loops contains a high spatial sensitivity to shallow structures. The use of the full possible number of soundings from a given number of loop positions yields a better model recovery by inversion compared to a survey with only coincident loop soundings with the same loop positions. As demonstrated an synthetic 2D aquifer models the improvement in model resolution is hereby dependent on the spatial extension of the inhomogeneity in respect to the loop size. For smooth variations in the water content, the effect of higher model resolution is quite small whereas small scale variations are much more reliably recovered if separated loop data are included.

Even though only noise free synthetic data are used where an optimum model recovery is already expected with a small number of data, it could be shown that inversion results that are equivalent for the coincident loop soundings within the convergence range of the optimization algorithm, still show significant differences for the sounding curves of separated loops. So, it is not only the higher data density that provides a better model recovery but a real improvement in spatial resolution that is gained by the use of a survey with separated loops. Study of the model of an ice ridge, where water is substituted by ice accumulation underlines the superior resolution of a full MRS dataset with all possible transmitter and receiver loop position permutations. Here, it is demonstrated that the

signal response from shallow structures contributes to data points of the full sounding curves of separated loop surveys, whereas only very small pulse moments of coincident loop soundings are effected by changes of water content in the first few meters. An application of MRS investigations on structures that were recently not resolvable with conventional coincident soundings seem to be possible with this configuration.

The improvement of model resolution was shown on real datasets. In two surveys I showed that 2D inversion of full separated loop data sets can resolve the spatial water distribution and yield a suitable model. In the case study of Nauen results were in good agreement with the local geology and furthermore discriminated a second aquifer that shows no resistivity contrast to the surrounding low water content layers. The survey in StCyr did not show a distinct water content stratification even though it was expected from a first geoelectrical section. This is explained by a water distribution that is not real 2D but shows significant 3D variations within the sensitive volume of the MRS loops.

The combination of the real 2D inversion based on the formulation of the 2D kernel function together with the high resolution and spatial coverage of profile like MRS soundings with separated and coincident loops provides a high potential of innovative MRS applications. The drawback of extensive acquisition time can easily be overcome by the application of a multichannel MRS receiver, recording the signal in multiple separated loops for one sounding a time. The loop spacing of one radius has proved to be a reasonable configuration, scalable in a certain range by the choice of adequate loop size in respect to the target of investigation.

Since two-dimensional water distributions are investigated by this new approach, the pre-assumption of homogeneous or 1D resistivity distributions, as in the present work, can not be generally maintained. For a full quantitative interpretation arbitrary resistivity distributions have to be taken into account at least in case of significant resistivity variations. Hence, the modeling algorithm for the computation of the loop fields has to be extended from the quasi-analytical formulation by Debye-potentials to a sophisticated numerical approach. First results with a Finite Element algorithm are already undertaken and will improve this lack in future. By the approach of such a modeling scheme the configuration can further more be extended to surveys with arbitrary surface topography. New approaches in the two-dimensional water content mapping of dykes, dunes or dams are then possible. The fundamentals of such new applications are basically covered by the formulation of the MRS signal with transmitter and receiver loop fields in arbitrary mutual orientation and the approach of 2D kernels in the present work. So only an improved numerical modeling of the loop fields has to be implied to allow the investigation of more complex structures in engineering and environmental geophysics.

The presented inversion strategy is just a basic application of a standard optimization algorithm. More sophisticated approaches in respect to stability, robustness and adaptive model regularization are needed for automatic inversion of field data. Implementation of T_2^* and T_1 time constant inversion as they are usually used in common 1D inversion is also envisaged, as well as complex inversion of the MRS signals once all influences on the signal

7. *Conclusion*

phase are correctly implemented in the forward modeling.

8. Acknowledgements

My research in Hydrogeophysics in general and in Magnetic Resonance Soundings in particular has been supported by many persons. I am indebted, among others, to

- Prof. U. Yaramanci and Prof. Burkhardt who provided excellent working conditions at the Department of Applied Geophysics of the Technical University Berlin. At all periods they greatly patronized my work. To Prof. U. Yaramanci in particular who actively supported and competently supervised my PhD-thesis. He improved my work by many fruitful discussions and critical questions and encouraged me in all my research activities.
- Anatoly Legchenko who acted as second referee of my PhD-thesis and who actively supported the realization of separated loop measurements.
- Gerhard Lange for many years of cooperation in the development and application of MRS measurements.
- Martina Braun in whose cooperation the comprehensive modeling software was developed. She provided indispensable assistance in the methodological development, the numerical realization, and in many pleasant days of field work.
- Michael Becken for many years of private lessons in electromagnetics and theoretical considerations.
- Dr. Martin Müller, Oliver Mohnke the Hydrogeophysics working group and all other colleagues at the Department of Applied Geophysics of the Technical University Berlin for an excellent teamwork.
- Jean Roy who initiated and supported the technique of 2D MRS and separated loop applications.
- Mr. Jean Bernard and the teams of IRIS Instruments and BRGM who provided an excellent technical support and facilitated the separated loop measurements. The free technical modification of the Numis device of the BRG is gratefully acknowledged.
- My family who had unlimited endurance for my work and research.

8. *Acknowledgements*

Bibliography

- Abraham, A., 1983. Principles of nuclear magnetism. Oxford University Press.
- Abraham, J. D., Legchenko, A., Mazella, A., White, E., Lane, J., Fleming, J. B., 2003. TDEM and Numisplus soundings at the Ash Meadows National Wildlife Refuge: A case study. Proceedings of the 2nd International Workshop on MRS, Orléans, France , 5–8.
- Baltassat, J. M., Legchenko, Anatloy, V., Michel, J., Sabatier, S., Chigot, D., Schmidt, J., 2003. Calibration of mrs results using hydrodynamic characterization from pumping tests. Proceedings of the 2nd International Workshop on MRS, Orléans, France .
- Becken, M., Burkhardt, H., 2004. An ellipticity criterion in magnetotelluric tensor analysis. Geophysical Journal International 159, 69–82, pPDF.
- Bene, G. J., 1979. Nuclear magnetism of liquid systems in the Earth field range. Physics Reports 58 (4), 213–267.
- Berckhemer, H., 1990. Grundlagen der Geophysik. Wissenschaftliche Buchgesellschaft.
- Braun, M., 2002. Untersuchungen komplexwertiger Oberflächen-NMR Signale im leitfähigen Untergrund. Master's thesis, Technische Universität Berlin.
- Braun, M., Hertrich, M., Yaramanci, U., 2002. Modelling of the phase behaviour in the SNMR signal. Proceedings of the 8th EEGS conference, Aveiro/Portugal .
- Braun, M., Hertrich, M., Yaramanci, U., 2004. Complex inversion of MRS data. Near Surface Geophysics (accepted) .
- Braun, M., Yaramanci, U., 2003. Inversions of Surface-NMR signals using complex kernels. Proceedings of the 9th EEGS-ES conference, Prague, Czech Republic , O–49.
- Eikam, A., 2000. Modellierung der Amplituden von Oberflächen-NMR-messungen an 2D- und 3D-strukturen. Diplomarbeit, Technische Universität Berlin, Fachgebiet Angewandte Geophysik.
- Hertrich, M., Braun, M., Yaramanci, U., 2004. Magnetic resonance soundings with separated transmitter and receiver loops. Submitted to Near Surface Geophysics, special issue on MRS .

Bibliography

- Hertrich, M., Yaramanci, U., 2003a. Complex transient Spin dynamic in MRS applications. Proceedings of the 2nd International Workshop on MRS, Orléans, France , 141–144.
- Hertrich, M., Yaramanci, U., 2003b. Surface-NMR with separated loops - investigations of spatial resolution. Proceedings of the 65th EAGE Conference and Technical Exhibition .
- Iris Instruments, 2000. NumisPlus - Surface Proton Magnetic Resonance system for water prospecting. Reference Manual.
URL http://www.iris-instruments.com/Pdf%20file/NumisP_Gb.pdf
- Jackson, J., 1983. Klassische Elektrodynamik. de Gruyter, Berlin.
- Legchenko, A., 2004. Magnetic Resonance Sounding: Enhanced Modeling of a Phase Shift. Applied Magnetic Resonance 25, 621–636.
- Legchenko, A., Semenov, A., Schirov, M., 1990. A device for measurement of subsurface water saturated layers paramters. USSR Patent 1540515, in Russian.
- Legchenko, A., Shushakov, O., 1998. Inversion of surface NMR data. Geophysics 63 (1), 75–84.
- Legchenko, A., Valla, P., 1998. Processing of surface proton magnetic resonance signals using non-linear fitting. Journal of Applied Geophysics 39, 77–83.
- Legchenko, A., Valla, P., May 2002. A review of the basic principles for proton magnetic resonance sounding measurements. Journal of Applied Geophysics 50 (1-2), 3–19, special Issue.
- Levitt, M. H., 2002. spin dynamics - Basics of Nuclear magnetic Resonance. John Wiley & Sons, LTD.
- Mansfield, P., Maudsley, A., Morris, P., Pykett, I., 1979. Selective Pulses in NMR Imaging: A reply to Criticism. Journal of Magnetic Resonance 33, 261–274.
- Michel, D., 1981. Grundlagen und Methoden der kernmagnetischen Resonanz. Akademie-Verlag, Berlin.
- Semenov, A., 1987. NMR hydroscope for water prospecting. Proceedings of the Seminar on Geotomography , 66–67.
- Torrey, H. C., 1949. Transient nutations in nuclear magnetic resonance. Physical Review 76 (8), 1059–1068.
- Trushkin, D., Shushakov, O., Legchenko, A., 1995. Surface NMR applied to an electroconductive medium. Geophysical Prospecting 43, 623–633.

- Valla, P., Legchenko, A., May 2002. One-dimensional modelling for proton magnetic resonance sounding measurements over an electrically conductive medium. *Journal of Applied Geophysics* 50 (1-2), 217–229, special Issue.
- Varian, R., 1962. Ground liquid prospecting method and apparatus. US Patent 3019383.
- Wait, J. R., 1962. A note on the electromagnetic response of a stratified earth. *Geophysics* 27 (03), 382–385.
- Ward, S. H., Hohmann, G. W., 1988. *Electromagnetic methods in Applied Geophysics*. Vol. 01. Soc. of Expl. Geophys., Ch. Electromagnetic theory for geophysical applications, pp. 131–312.
- Warsa, W., Mohnke, O., Yaramanci, U., 2002. 3-D modelling of Surface NMR amplitudes and decay times. *Water Resources and Environment Research ICWRER 2002*, 209–212.
- Weichman, P. B., Lively, E. M., Ritzwoller, M., 1999. Surface nuclear magnetic resonance imaging of large systems. *Physical Review Letters* 82 (20), 4102–4105.
- Weichman, P. B., Lively, E. M., Ritzwoller, M. H., 2000. Theory of surface nuclear magnetic resonance with applications to geophysical imaging problems. *Physical Review E* 62 (1, Part B), 1290–1312.
- Weichman, P. B., Lun, D. R., Ritzwoller, M. H., Lively, E. M., 2002. Study of surface nuclear magnetic resonance inverse problems. *Journal of Applied Geophysics* 50 (1-2), 129–147, special Issue.
- Weidelt, P., 1984. *Einführung in die elektromagnetische Tiefenforschung*. Vorlesungsskript.
- Yaramanci, U., 2000. Surface Nuclear Magnetic Resonance (SNMR) - A new method for exploration of ground water and aquifer properties. *Annali di Geofisica* 43 (6), 1159–1175.
- Yaramanci, U., Lange, G., Hertrich, M., 2002. Aquifer characterisation using surface NMR jointly with other geophysical techniques at the Nauen/Berlin test site. *Journal of Applied Geophysics* 50 (1-2), 47–65.

Bibliography

Appendix

Bibliography

A. Appendix to Chapter 1

A.1. Spatial propagation of electromagnetic fields in layered conductive media

A.1.1. TE- and TM-modes

From Maxwell's equations the vector fields for the magnetic flux \mathbf{b} and the electrical current density \mathbf{j} can be decomposed into the sum of the partial fields with electric and magnetic origin respectively:

$$\mathbf{b} = \mathbf{b}_{TE} + \mathbf{b}_{TM} \quad (\text{A.1})$$

$$\mathbf{j} = \mathbf{j}_{TE} + \mathbf{j}_{TM} \quad (\text{A.2})$$

Equation A.1 and A.2 indicate a decomposition of the vector fields into poloidal and toroidal parts, where the toroidal electric and the poloidal magnetic field compose the TE-mode (tangential electric) and the poloidal electric and the toroidal magnetic field build the TM-mode (tangential magnetic), respectively. This means that a vertical magnetic field induces a radial electrical field, and vice versa. For wire loops as used in MRS applications, the magnetic field loop only vertical components at the half-space boundary, so that only the TE-mode has to be considered. Even non-vertical components of an inductive electromagnetic source in the air can not be charged to the ground, since no electric currents can cross the half-space boundary because of the infinite resistivity of the free space; the TM-mode is completely reflected at the earth's surface. For inductive coupling, a TM-mode can neither be generated nor recorded.

A.1.2. The scalar potential

In homogeneous regions, the electromagnetic vector fields are divergence-free away from the source and can be expressed by the scalar potential φ_{TE} , (Debye Potential compare e.g. Weidelt, 1984; Schelkunoff potentials in Ward and Hohmann, 1988). In case of inductive coupling, i.e. for the TE-mode, equations (A.1), (A.2) then give the identity

$$\mathbf{b} = \mathbf{b}_{TE} = \nabla \times \nabla \times (\hat{z}\varphi_{TE}) \quad (\text{A.3})$$

$$\mathbf{j} = \mathbf{j}_{TE} = -\nabla \times (\hat{z}\sigma\varphi_{TE}) \quad (\text{A.4})$$

A. Appendix to Chapter 1

with \mathbf{j} the current density and \mathbf{b} the magnetic flux. Inserting Maxwell's 1st and 2nd laws

$$\nabla \times \mathbf{e} = -\frac{\partial}{\partial t} \mathbf{b} \quad (\text{A.5})$$

$$\nabla \times \mathbf{h} = \mathbf{j} \quad (\text{A.6})$$

yields for the electric and magnetic fields

$$\mathbf{e} = -\nabla \times \left(\hat{z} \frac{\partial}{\partial t} \varphi_{TE} \right) \quad (\text{A.7})$$

$$\mathbf{h} = \frac{1}{\mu_0} \nabla \times \nabla \times (\hat{z} \varphi_{TE}), \quad (\text{A.8})$$

where \hat{z} is the vertical unit vector. The potential φ_{TE} satisfies the diffusion equation

$$\nabla^2 \varphi_{TE} = \mu_0 \sigma \frac{\partial}{\partial t} \varphi_{TE} \quad (\text{A.9})$$

which is supposed to be valid in the frequency range of MRS applications for moderate ground conductivities. The electromagnetic field components are then derived from the Debye Potentials as

$$\begin{aligned} e_x &= -\frac{\partial^2}{\partial y \partial t} \varphi_{TE} & h_x &= \frac{1}{\mu_0} \frac{\partial^2}{\partial x \partial z} \varphi_{TE} \\ e_y &= +\frac{\partial^2}{\partial x \partial t} \varphi_{TE} & h_y &= \frac{1}{\mu_0} \frac{\partial^2}{\partial y \partial z} \varphi_{TE} \\ e_z &= 0 & h_z &= -\frac{1}{\mu_0} \left(\frac{\partial^2}{\partial x^2} + \frac{\partial^2}{\partial y^2} \right) \varphi_{TE} \end{aligned} \quad (\text{A.10})$$

Due to the multi-frequent nature in space and time domain of the inhomogeneous field close to the source, it is convenient to treat the problem in the frequency-wavenumber domain and recreate the full vector field by Fourier-synthesis of the entire spectra. In the following the angular frequency ω , the horizontal space vector $\mathbf{r} = (x, y)^T$ and the wavenumber vector $\boldsymbol{\kappa} = (\kappa_x, \kappa_y)^T$ are used. The potentials transform from the respective domains as follows

$$\hat{\phi}(\boldsymbol{\kappa}, z, \omega) = \int \int \int_{-\infty}^{\infty} \varphi(\mathbf{r}, t) e^{-i(\boldsymbol{\kappa} \cdot \mathbf{r} + \omega t)} dx dy dt \quad (\text{A.11})$$

$$\varphi(\mathbf{r}, z, t) = \left(\frac{1}{2\pi} \right)^3 \int \int \int_{-\infty}^{\infty} \hat{\phi}(\boldsymbol{\kappa}, z, \omega) e^{i(\boldsymbol{\kappa} \cdot \mathbf{r} + \omega t)} d\omega d^2 \boldsymbol{\kappa} (z) \quad (\text{A.12})$$

The diffusion equation for the potential (equation A.9) is thus also valid in the frequency-

A.1. Spatial propagation of electromagnetic fields in layered conductive media

wavenumber domain

$$\begin{aligned}\widehat{\Phi}_{TE}''(z) &= (\kappa^2 + k^2(z)) \widehat{\Phi}_{TE}(z) \\ &= \alpha^2(z) \widehat{\Phi}_{TE}(z),\end{aligned}\tag{A.13}$$

with

$$\begin{aligned}\kappa^2(z) &= |\kappa(z)|^2 = u^2(z) + v^2(z) \\ k^2 &= i\omega\mu_0\sigma \\ \alpha^2(z) &= (\kappa^2 + k^2(z))\end{aligned}$$

and the vector fields in the frequency domain, which are finally of interest, can be derived from the potential by

$$\begin{aligned}\widehat{E}_x &= +\omega v \widehat{\Phi}_{TE} & \widehat{H}_x &= \frac{iv}{\mu_0} \widehat{\Phi}_{TE}' \\ \widehat{E}_y &= -\omega u \widehat{\Phi}_{TE} & \widehat{H}_y &= \frac{iv}{\mu_0} \widehat{\Phi}_{TE}' \\ \widehat{E}_r &= -\omega \kappa \widehat{\Phi}_{TE} & \widehat{H}_r &= -\frac{\kappa}{\mu_0} \widehat{\Phi}_{TE}' \\ \widehat{E}_z &= 0 & \widehat{H}_z &= \frac{\kappa^2}{\mu_0} \widehat{\Phi}_{TE},\end{aligned}\tag{A.14}$$

where $\kappa^2 = u^2 + v^2$. Assuming a stratified half-space with M layers of at depth h_m and conductivity σ_m , the expression for the Debye potential within each layer of constant conductivity is given by:

$$k_m^2 = i\omega\mu_0\sigma_m\tag{A.15}$$

$$\alpha_m^2 = (\kappa^2 + k_m^2)\tag{A.16}$$

A.1.3. Partial waves

The solutions of equation A.13 is given by upward and downward traveling waves as

$$\begin{aligned}\widehat{\Phi}_{TE}(z) &= b_m^- e^{-\alpha_m(z-h_m)} + b_m^+ e^{+\alpha_m(z-h_m)} \\ &= b_m^- e^{-\alpha_m(z-h_m)} + b_m^+ e^{-\alpha_m(-z+h_m)}. \\ &\text{for } h_m < z < h_{m+1}\end{aligned}\tag{A.17}$$

These harmonic solutions of the diffusion equation now fund the 'partial waves', where components with positive indices and exponentials 'propagate' in positive z-direction, and negatives in negative z-direction. The vertical derivative of the potential is required to

A. Appendix to Chapter 1

derive the horizontal components of the magnetic field and is given by

$$\begin{aligned}\widehat{\Phi}'_{TE}(z) &= \frac{\partial}{\partial z} (b_m^- e^{-\alpha_m(z-h_m)} + b_m^+ e^{+\alpha_m(z-h_m)}) \\ &= \alpha_m (b_m^- e^{-\alpha_m(z-h_m)} - b_m^+ e^{-\alpha_m(-z+h_m)}) \\ &\text{for } h_m < z < h_{m+1}\end{aligned}\tag{A.18}$$

For the lower half-space $z > h_M$ all components must vanish for $z \rightarrow \infty$, i.e. only downwards traveling partial wave are physically realized. Therefore, for $z > h_M$

$$\widehat{\Phi}_{TE}(z) = b_m^- e^{-\alpha_M(z-h_M)},\tag{A.19}$$

$$\widehat{\Phi}'_{TE}(z) = \alpha_m b_m^- e^{-\alpha_M(z-h_M)}\tag{A.20}$$

A.1.4. Layer and strata impedances

The electromagnetic impedance Z is in general determined by the ratio of perpendicular components of electrical and magnetic field vectors

$$Z_{TE}(z, \kappa, \omega) = \frac{\widehat{E}_{TE x}(z, \kappa, \omega)}{\widehat{H}_{TE y}(z, \kappa, \omega)} = -\frac{\widehat{E}_{TE y}(z, \kappa, \omega)}{\widehat{H}_{TE x}(z, \kappa, \omega)}.\tag{A.21}$$

With equations A.14 the respective fields can be expressed by the potentials in the frequency-wavenumber domain as

$$Z_{TE}(z, \kappa, \omega) = -i\omega\mu_0 \frac{\widehat{\Phi}_{TE}(z, \kappa, \omega)}{\widehat{\Phi}'_{TE}(z, \kappa, \omega)}.\tag{A.22}$$

For a more convenient procedure the modified impedance

$$B(z, \kappa, \omega) := \frac{i\omega\mu_0}{Z_{TE}(z, \kappa, \omega)}\tag{A.23}$$

and its reciprocal

$$\begin{aligned}C(z, \kappa, \omega) &:= \frac{1}{B(z, \kappa, \omega)} \\ &= \frac{Z_{TE}(z, \kappa, \omega)}{i\omega\mu_0},\end{aligned}\tag{A.24}$$

are defined, also known as B-response and C-response, respectively. According to equation A.22, the B- and C-response are expressed by the potential and its vertical derivative for

A.1. Spatial propagation of electromagnetic fields in layered conductive media

each layer, respectively:

$$B(z, \kappa, \omega) = -\frac{\widehat{\Phi}_{TE}(z, \kappa, \omega)}{\widehat{\Phi}'_{TE}(z, \kappa, \omega)} \quad (\text{A.25})$$

$$C(z, \kappa, \omega) = -\frac{\widehat{\Phi}'_{TE}(z, \kappa, \omega)}{\widehat{\Phi}_{TE}(z, \kappa, \omega)} \quad (\text{A.26})$$

and with the solution found in equation A.19 and A.20, rewritten in terms of partial waves; here for the B-response:

$$\begin{aligned} B_m &= -\frac{\widehat{\Phi}'_{TE}(h_m)}{\widehat{\Phi}_{TE}(h_m)} \\ &= \alpha_m \frac{b_m^- - b_m^+}{b_m^- + b_m^+} \end{aligned} \quad (\text{A.27})$$

$$\begin{aligned} B_{m+1} &= -\frac{\widehat{\Phi}'_{TE}(h_{m+1})}{\widehat{\Phi}_{TE}(h_{m+1})} \\ &= \alpha_m \frac{b_m^- e^{-\alpha_m d_m} - b_m^+ e^{+\alpha_m d_m}}{b_m^- e^{-\alpha_m d_m} + b_m^+ e^{+\alpha_m d_m}} \end{aligned} \quad (\text{A.28})$$

$$\begin{aligned} B_M &= \frac{\widehat{\Phi}'_{TE}(h_M)}{\widehat{\Phi}_{TE}(h_M)} \\ &= -\alpha_M \end{aligned} \quad (\text{A.29})$$

with $d_m = h_{m+1} - h_m$ the thickness of the m-th layer. Here it is convenient to define the 'reflection coefficient' γ_m as the ratio of down- and upwards propagating partial waves b_m^+ , b_m^- at the boundary plane. Rewriting equations A.27 and A.28 and solving them after γ_m leads to

$$B_m = \alpha_m \frac{1 - \gamma_m}{1 + \gamma_m} \quad (\text{A.30})$$

$$\gamma_m = \frac{\alpha_m - B_m}{\alpha_m + B_m} \quad (\text{A.31})$$

$$B_{m+1} = \alpha_m \frac{1 - \gamma_m e^{+2\alpha_m d_m}}{1 + \gamma_m e^{+2\alpha_m d_m}} \quad (\text{A.32})$$

$$\gamma_m = \frac{\alpha_m - B_{m+1}}{\alpha_m + B_{m+1}} e^{-2\alpha_m d_m}. \quad (\text{A.33})$$

Thus, two defining equations for the same reflection coefficient are obtained, both depending either on B_m or B_{m+1} . Equating both solutions for γ_m yields after some transformation

A. Appendix to Chapter 1

the dependency

$$B_m = \alpha_m \frac{B_{m+1} + \alpha_m \tanh(\alpha_m d_m)}{\alpha_m + B_{m+1} \tanh(\alpha_m d_m)} \quad (\text{A.34})$$

$$B_M = -\alpha_M, \quad (\text{A.35})$$

The above formulation of the recursive determination of strata impedances is actually the solution for the impedance of a layered half-space for Transient Electromagnetics, found by Wait (1962). The recurrence relation evolves from the ratio of the potentials and their vertical derivatives at the strata discontinuity as boundary values. The effective impedance of a layer is therefore not determined by its intrinsic impedance exclusively, but by the recursive determination of all underlying layers.

A.1.5. Downward continuation

With the help of the determined strata impedances the potentials, i.e. the vector field components, are continued to depth from one layer boundary to the next. For the potential themselves, determining the horizontal electric fields, and for its vertical derivative, as it enters the equations for the horizontal magnetic fields (equation A.14), one gets

$$\hat{\Phi}_{TE}(h_{m+1}) = \hat{\Phi}_{TE}(h_m) \frac{\alpha_m + B_m}{\alpha_m + B_{m+1}} e^{-\alpha_m d_m} \quad (\text{A.36})$$

$$\hat{\Phi}'_{TE}(h_{m+1}) = -\alpha_m \hat{\Phi}_{TE}(h_m) \frac{\alpha_m + B_m}{\alpha_m + B_{m+1}} e^{-\alpha_m d_m}. \quad (\text{A.37})$$

From the potentials at the layer boundary the continuation of the potential and its vertical derivative through each layer, respectively, is given by

$$\begin{aligned} \hat{\Phi}_{TE}(z) &= \hat{\Phi}_{TE}(h_m) \frac{1}{2} \left(1 + \frac{B_m}{\alpha_m} \right) \\ &\times \left(e^{-\alpha_m(z-h_m)} - \frac{B_{m+1} - \alpha_m}{B_{m+1} + \alpha_m} e^{-\alpha_m(d_m+h_{m+1}-z)} \right) \end{aligned} \quad (\text{A.38})$$

$$\begin{aligned} \hat{\Phi}'_{TE}(z) &= \hat{\Phi}_{TE}(h_m) \frac{1}{2} \left(1 + \frac{B_m}{\alpha_m} \right) \\ &\times \left(e^{-\alpha_m(z-h_m)} + \frac{1 - \alpha_m C_{m+1}}{1 + \alpha_m C_{m+1}} e^{-\alpha_m(\alpha_m+h_{m+1}-z)} \right). \end{aligned} \quad (\text{A.39})$$

A.1.6. Coupling of the source fields to a conductive ground

The total effective potential of the source located on a conductive half-space is the sum of the potential of the source in free space and a part reflected at the Earth's surface. The

A.2. Expressions for different source types

reflection coefficient γ_0 is determined by the impedance of the stratified half-space on the Earth's surface according equation A.31, where the conductivity distribution with depth must be known. The potential of the source on the half-space boundary in presence of a conductive ground is then determined by

$$\begin{aligned}\widehat{\Phi}_{TE}(0, \kappa, \omega) &= (1 + \gamma_0) \widehat{\Phi}_{TE}^e(\kappa, \omega) \\ &= \frac{2\kappa}{\kappa + B_0} \widehat{\Phi}_{TE}^e(\kappa, \omega)\end{aligned}\tag{A.40}$$

$$\begin{aligned}\widehat{\Phi}'_{TE}(0, \kappa, \omega) &= -\kappa(1 - \gamma_0) \widehat{\Phi}_{TE}^e(\kappa, \omega) \\ &= -\frac{2\kappa B_0}{\kappa + B_0} \widehat{\Phi}_{TE}^e(\kappa, \omega),\end{aligned}\tag{A.41}$$

where $\widehat{\Phi}_{TE}^e$ is the potential of a source in free space.

From the given derivation evolves an analytic integral expressions to for the horizontal and vertical components of the induced electromagnetic fields, respectively. These integrals can be numerically solved with sufficient accuracy to provide the spatial electromagnetic field distribution in the subsurface.

A.2. Expressions for different source types

A.2.1. Vertical magnetic dipole (vmd)

For a vertical magnetic dipole in a non-conductive medium at the source point $r = 0$, $z = -h$, the magnetic dipole moment at any point in space domain is given by (Weidelt (1984))

$$H_{TE}^e(\mathbf{r}, z, \omega) = \frac{M(\omega)}{4\pi} \nabla \left(\frac{\partial}{\partial z} \frac{1}{R} \right).\tag{A.42}$$

Additionally, the dipole moment from the definition of the potential in equation ?? can be derived as:

$$H_{TE}^e(\mathbf{r}, z, \omega) = \frac{1}{\mu_0} \nabla \left(\frac{\partial}{\partial z} \Phi_{TE}^e(\mathbf{r}, z, \omega) \right).\tag{A.43}$$

Equalizing both equations immediately yields the potential in space domain

$$\Phi_{TE}^e(\mathbf{r}, z, \omega) = \frac{\mu_0 M(\omega)}{4\pi} \frac{1}{R}.\tag{A.44}$$

A. Appendix to Chapter 1

Using the Weber-Integral:

$$\int_0^\infty e^{-a\kappa} J_0(\kappa b) d\kappa = \frac{1}{\sqrt{a^2 + b^2}} \quad (\text{A.45})$$

$$\frac{1}{R} = \frac{1}{\sqrt{r^2 + (z + h)^2}} \quad (\text{A.46})$$

and the Fourier-Bessel-transformation

$$\widehat{F}(\kappa) = \int_0^\infty F(r) J_0(\kappa r) r dr \quad (\text{A.47})$$

$$F(r) = \int_0^\infty \widehat{F}(\kappa) J_0(\kappa r) \kappa d\kappa \quad (\text{A.48})$$

substituted in A.44 yields the general formulation of the potential in the wavenumber domain:

$$\Phi_{TE}^e(\kappa, z, \omega) = \frac{\mu_0 M(\omega)}{4\pi} \frac{1}{\kappa} e^{-\kappa|z+h|}. \quad (\text{A.49})$$

and the total potential at the Earth's surface, equivalent to equation A.40, is given by

$$\begin{aligned} \widehat{\Phi}_{TE}(\kappa, 0, \omega) &= (1 + \gamma_0) \widehat{\Phi}_{TE}^e(\kappa, \omega) \\ &= \frac{2\kappa}{\kappa + B_0} \widehat{\Phi}_{TE}^e(\kappa, \omega) \\ &= \frac{\mu_0 M(\omega)}{2\pi} \frac{1}{\kappa + B_0}. \end{aligned} \quad (\text{A.50})$$

The potential in space domain is then obtained by inverse Fourier transformation, where equation A.12

$$\Phi(r, z, \omega) = \frac{1}{4\pi^2} \int \int_{-\infty}^\infty \widehat{\Phi}(\boldsymbol{\kappa}, z, t) e^{i\boldsymbol{\kappa} \cdot \mathbf{r}} d^2\boldsymbol{\kappa} \quad (\text{A.51})$$

simplifies for radial symmetric conditions to

$$\Phi(r, z, \omega) = \frac{1}{2\pi} \int_0^\infty \widehat{\Phi}(\kappa, z, t) J_0(\kappa r) \kappa d\kappa. \quad (\text{A.52})$$

and we get

$$\Phi(r, 0, \omega) = \frac{\mu_0 M(\omega)}{2\pi} \int_0^\infty \frac{\kappa}{\kappa + B_0} J_0(\kappa r) d\kappa. \quad (\text{A.53})$$

A.2. Expressions for different source types

The respective field components are then obtained by spatial derivation in r and z according to equation A.30 as

$$\begin{aligned} H_r(r, 0, \omega) &= \frac{1}{\mu_0} \frac{\partial^2}{\partial r \partial z} \Phi(r, 0, \omega) \\ &= \frac{M(\omega)}{2\pi} \int_0^\infty \frac{\kappa^2 B_0}{\kappa + B_0} J_1(\kappa r) d\kappa \end{aligned} \quad (\text{A.54})$$

$$\begin{aligned} H_z(r, 0, \omega) &= \frac{1}{\mu_0} \frac{\partial^2}{\partial z^2} \Phi(r, 0, \omega) \\ &= \int_0^\infty \frac{\kappa^3}{\kappa + B_0} J_0(\kappa r) d\kappa \end{aligned} \quad (\text{A.55})$$

and the downwards continuation is done according to equations A.52 and A.53

$$H_r(r, z, \omega) = \frac{M(\omega)}{2\pi} \int_0^\infty \frac{\kappa^2 B_0}{\kappa + B_0} g_F(z) J_1(\kappa r) d\kappa \quad (\text{A.56})$$

$$H_z(r, z, \omega) = \frac{M(\omega)}{2\pi} \int_0^\infty \frac{\kappa^3}{\kappa + B_0} g_{F'}(z) J_0(\kappa r) d\kappa \quad (\text{A.57})$$

stepwise for each layer. These Fourier-transformations can now easily be solved by linear digital filtering.

A.2.2. Horizontal magnetic dipole (hmd)

The basic evaluation of the source field is the same than for the vmd, but the spatial derivations according to x and y , respectively yield:

$$\begin{aligned} H_x(r, 0, \omega) &= \frac{m}{4\pi} \frac{\partial^2}{\partial x^2} \int_0^\infty \frac{\kappa}{\kappa + B_0} J_0(\kappa r) d\kappa \\ &= -\frac{m}{4\pi} \left(\frac{1}{r} - \frac{2x^2}{r^3} \right) \int_0^\infty \frac{\kappa}{\kappa + B_0} J_1(\kappa r) d\kappa - \frac{m}{4\pi} \frac{x^2}{r^2} \int_0^\infty \frac{\kappa^3}{\kappa + B_0} J_0(\kappa r) d\kappa \end{aligned} \quad (\text{A.58})$$

$$H_y(r, 0, \omega) = \frac{m}{4\pi} \frac{xy}{r^3} \int_0^\infty \frac{\kappa^2}{\kappa + B_0} J_1(\kappa r) d\kappa - \int_0^\infty \frac{\kappa^3}{\kappa + B_0} J_1(\kappa r) d\kappa \quad (\text{A.59})$$

$$H_z(r, 0, \omega) = \frac{m}{4\pi} \int_0^\infty \frac{\kappa^3}{\kappa + B_0} J_1(\kappa r) d\kappa \quad (\text{A.60})$$

A.2.3. Large horizontal loop

The potential of a large horizontal loop can be derived at the z-axis, for $r = 0$ by Biot-Savart's law as:

$$\Phi_{TE}^e(0, z, \omega) = \frac{\mu_0 I(\omega)}{2} \frac{a^2}{|z + h| + (a^2 + |z + h|^2)^{1/2}} \quad (\text{A.61})$$

Using the integral identity

$$F(0, z) = \int_0^\infty \hat{F}(\kappa, z) J_0(0) \kappa d\kappa \quad (\text{A.62})$$

yields the source potential in the wave-number domain

$$\Phi_{TE}^e(r, z, \omega) = \frac{\mu_0 a I(\omega)}{2} \int_0^\infty \frac{e^{-\kappa|z+h|}}{\kappa} J_1(\kappa a) J_0(\kappa r) d\kappa. \quad (\text{A.63})$$

For source and receiver at the earth surface, i.e., $z, h = 0$, and with the coupling to the ground from equations A.54 and A.55 the induced potential at the boundary plane to the stratified half-space is given by an inverse Hankel-transformation

$$\Phi_{TE}(r, 0, \omega) = \frac{\mu_0 a I(\omega)}{2} \int_0^\infty \frac{\gamma_0}{\kappa} J_1(\kappa a) J_0(\kappa r) d\kappa. \quad (\text{A.64})$$

The field components in the space domain are then after equation A.10

$$H_z(r, 0, \omega) = \frac{\mu_0 a I(\omega)}{2} \int_0^\infty \frac{\kappa^2}{\mu_0} \gamma_0 J_1(\kappa a) J_0(\kappa r) d\kappa \quad (\text{A.65})$$

$$H_r(r, 0, \omega) = \frac{\mu_0 a I(\omega)}{2} \int_0^\infty \frac{1}{\mu_0} \frac{\gamma_0}{\kappa} J_1(\kappa, a) J_0(\kappa r) d\kappa. \quad (\text{A.66})$$

B. Appendix to Chapter 5

B.1. 2D kernels in x-z sections

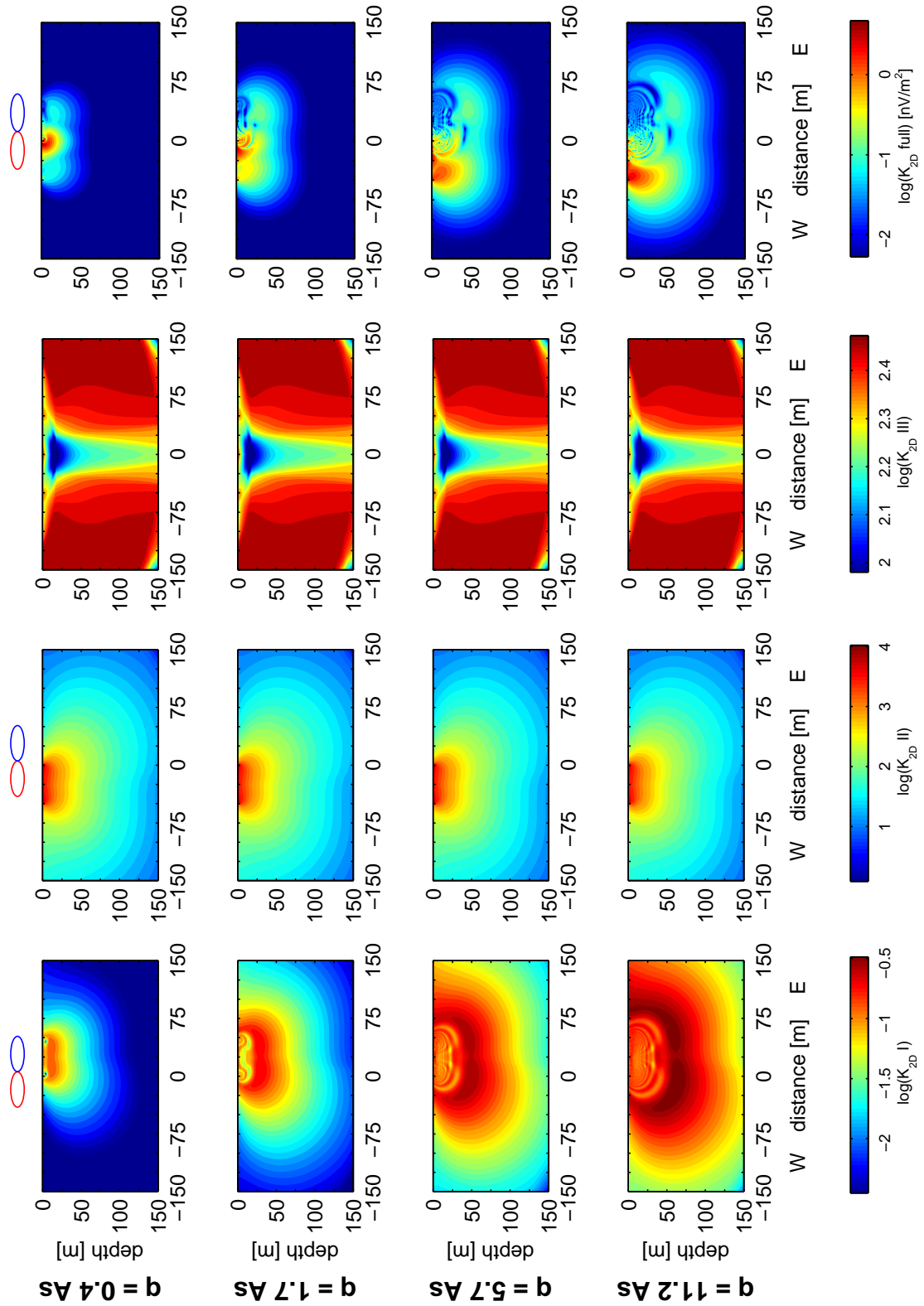


Figure B.1.: West-east 2D kernel with transmitter east of the receiver.

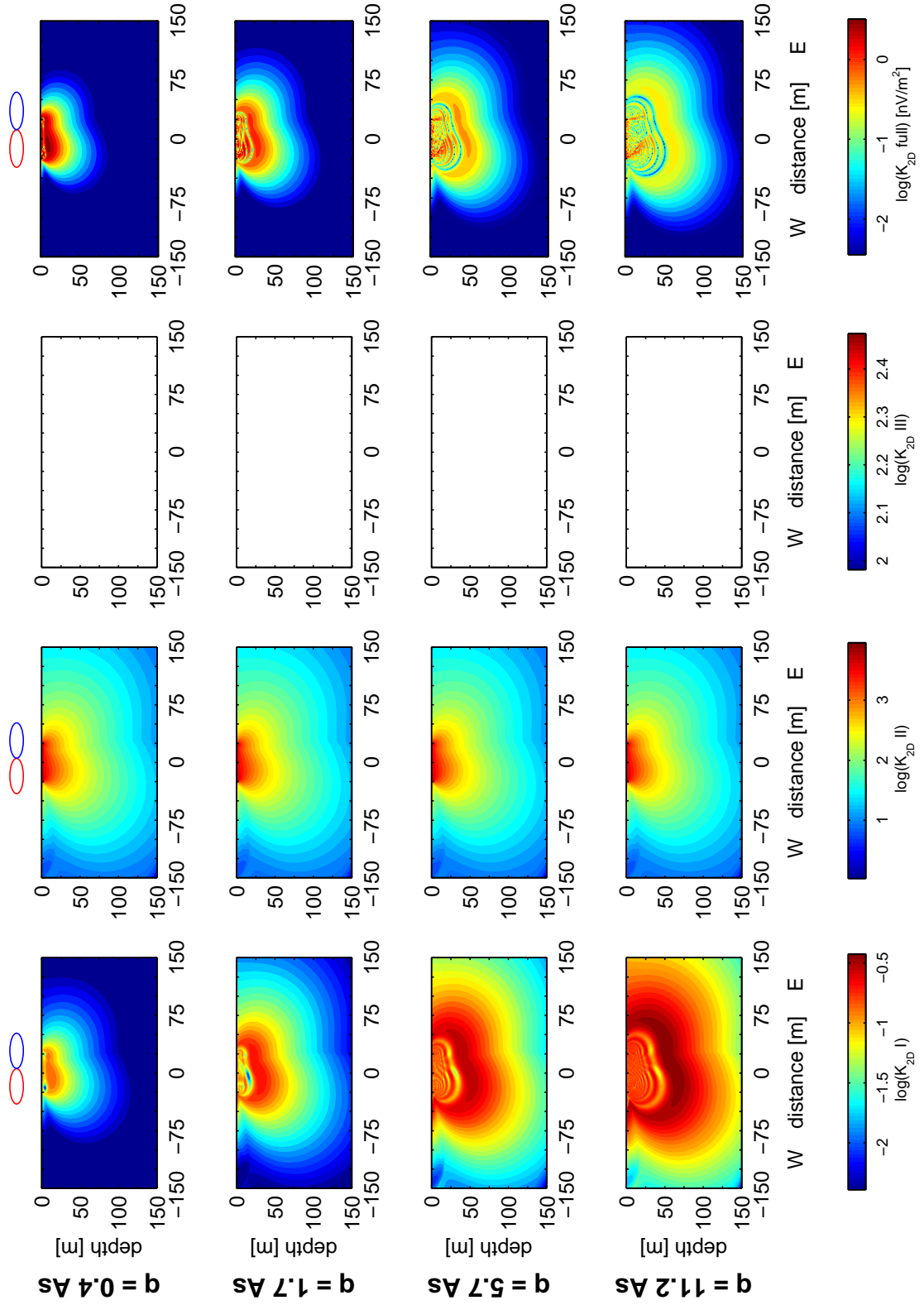


Figure B.2.: South-north 2D kernel for coincident loops.

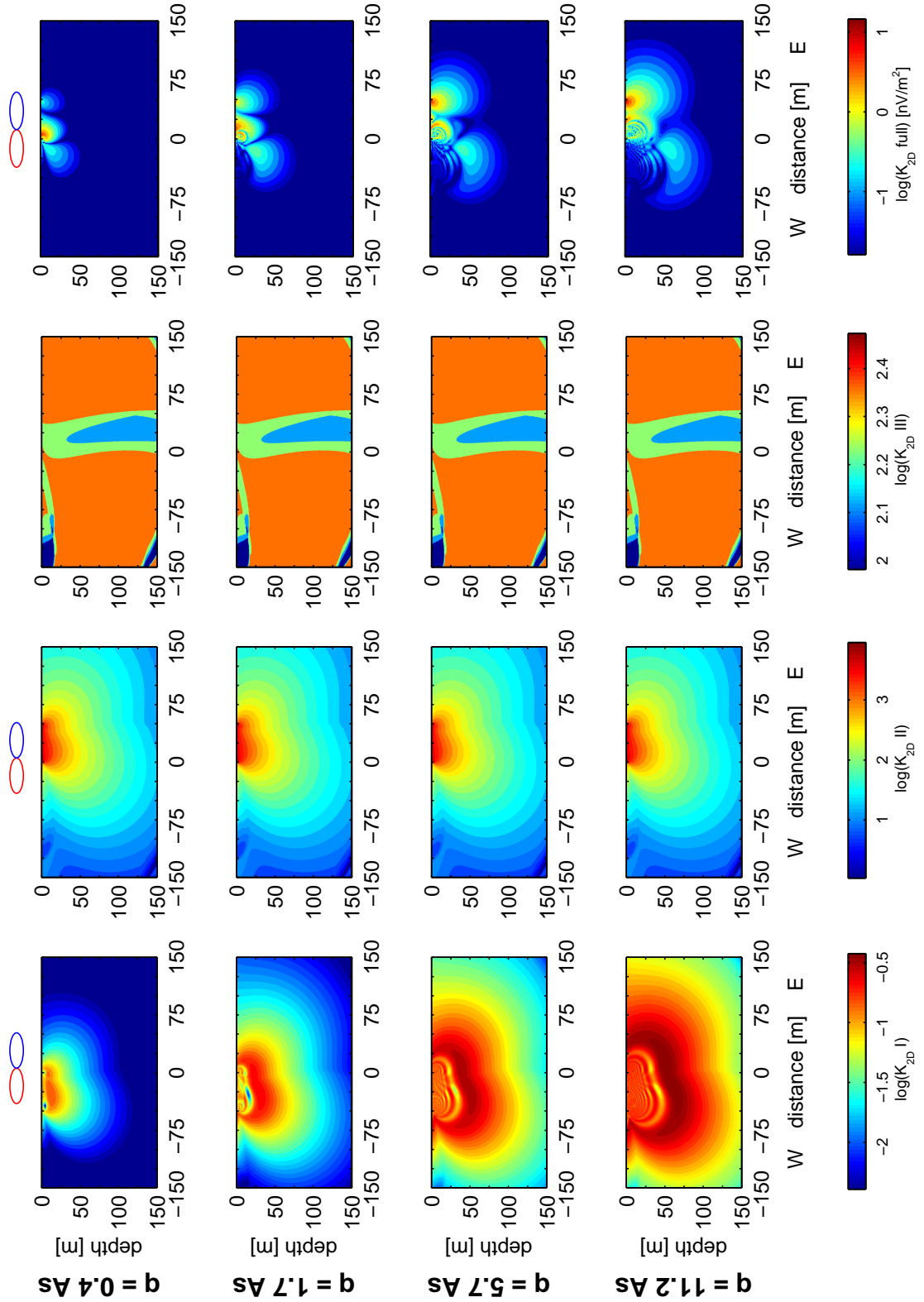


Figure B.3.: South-north 2D kernel with trasnmittter south of the receiver.

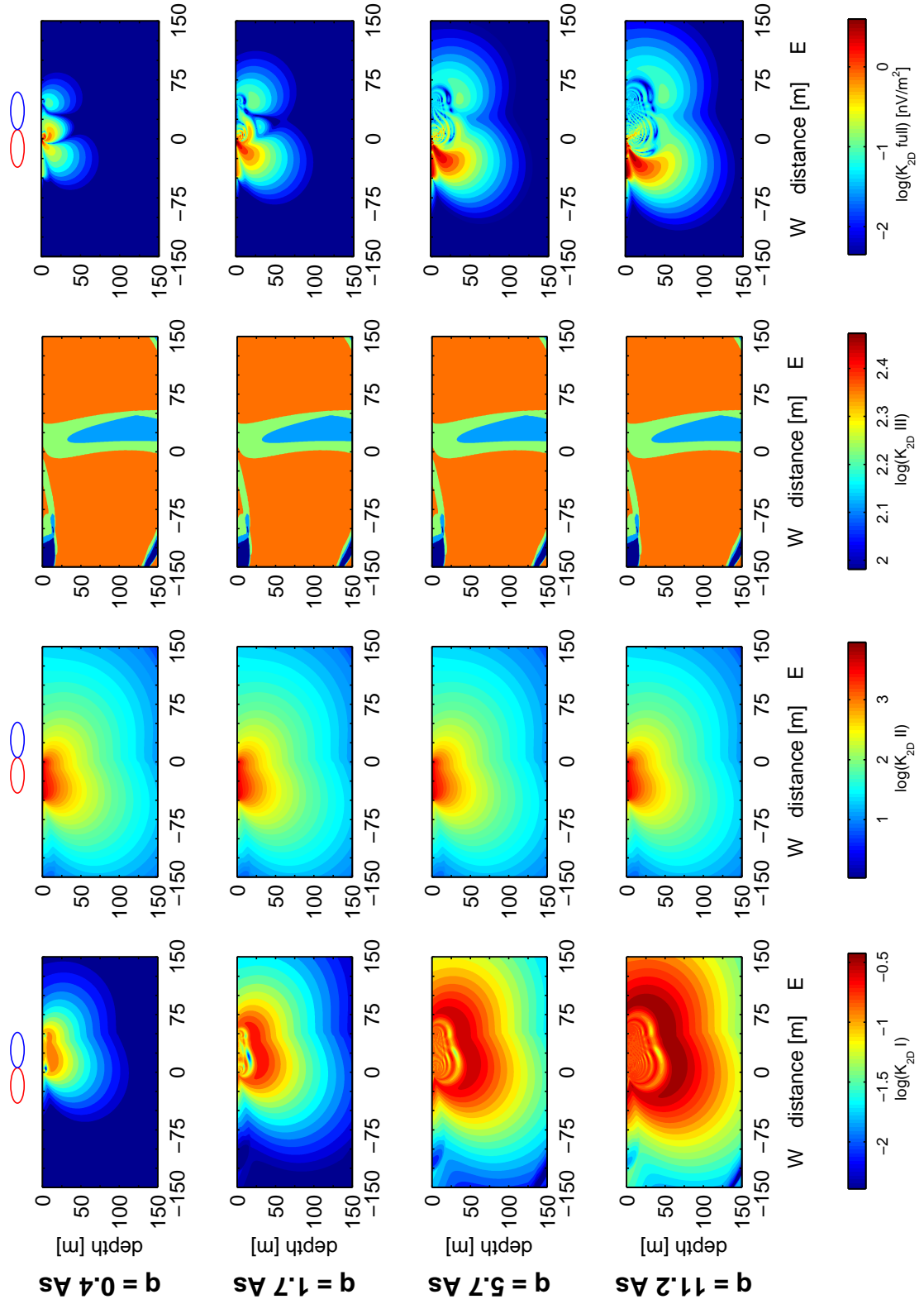


Figure B.4.: South-north 2D kernel with trasnmitter north of the receiver.

B.2. 2D kernels in x-y maps

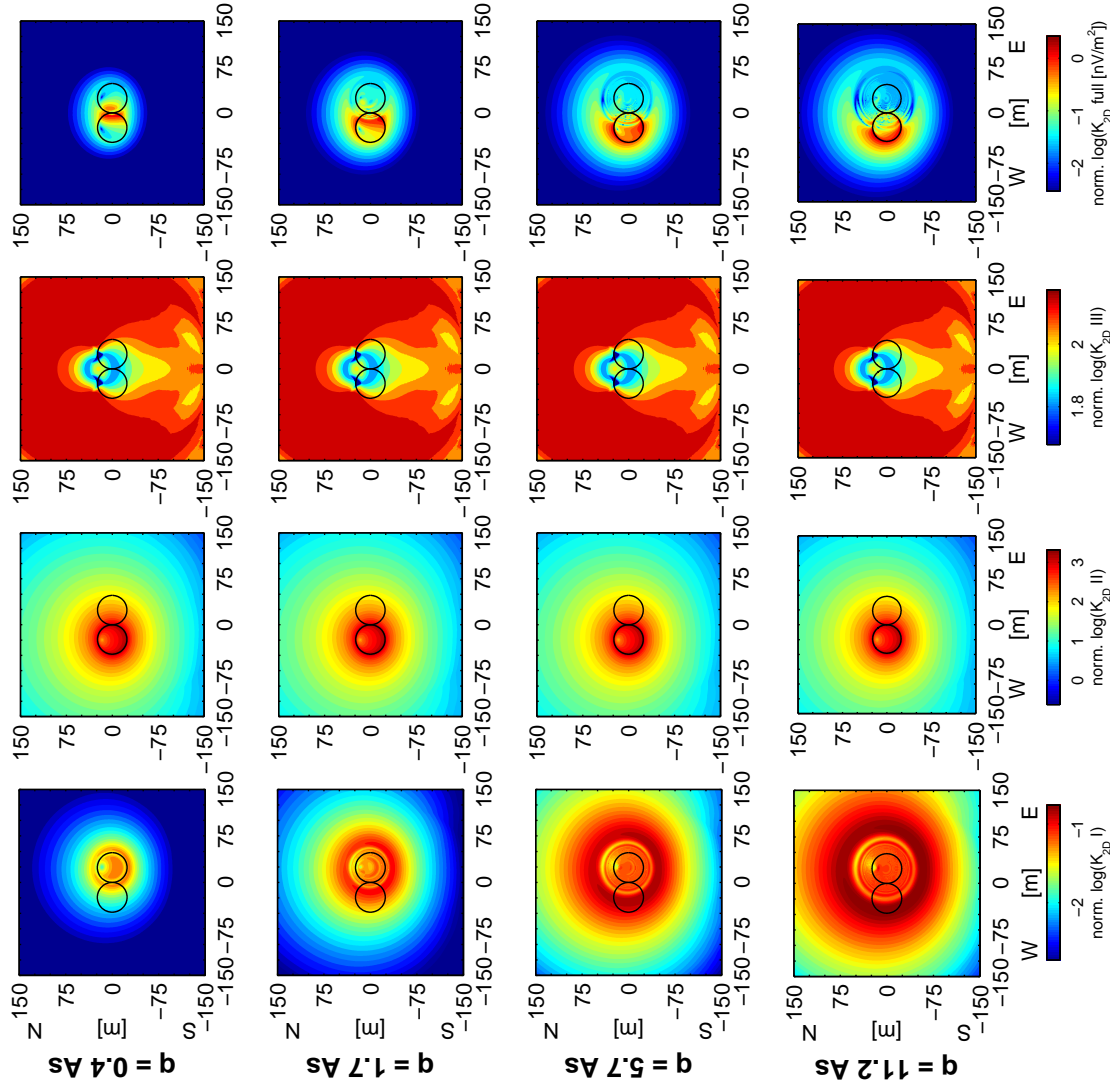


Figure B.5.: 2D kernel in map representation with transmitter east of the receiver.

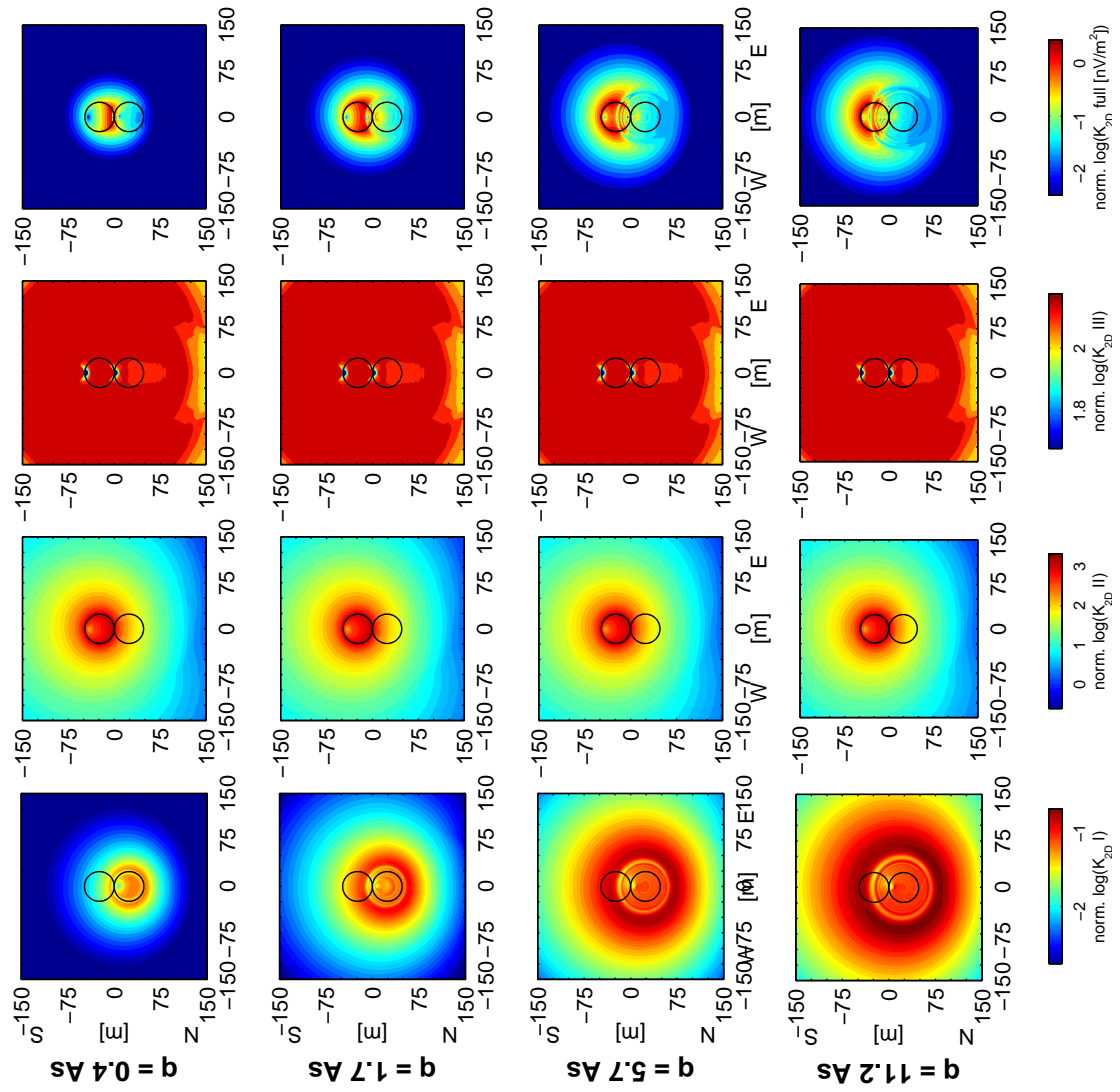


Figure B.6.: 2D kernel in map representation with transmitter south of the receiver.

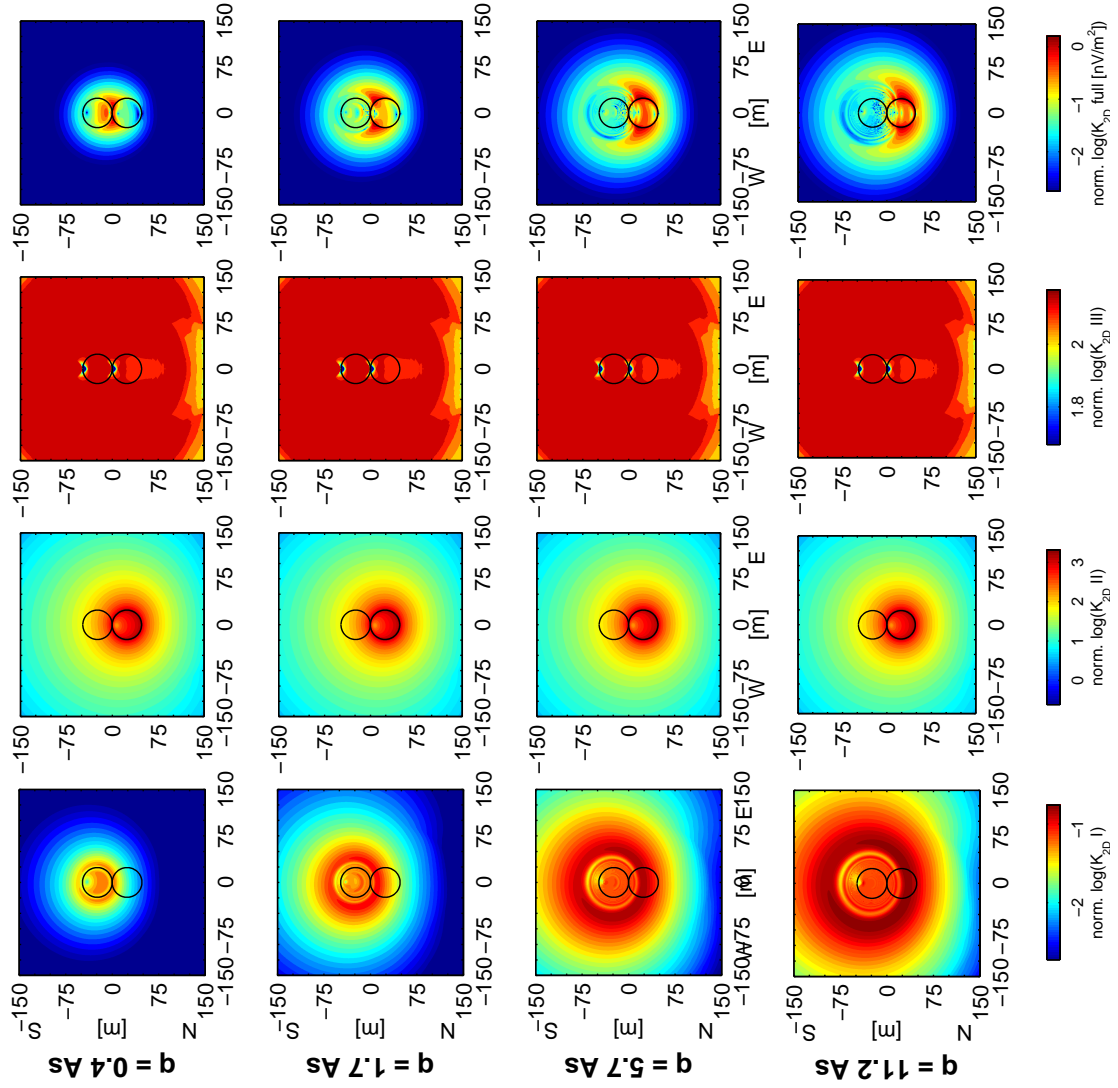
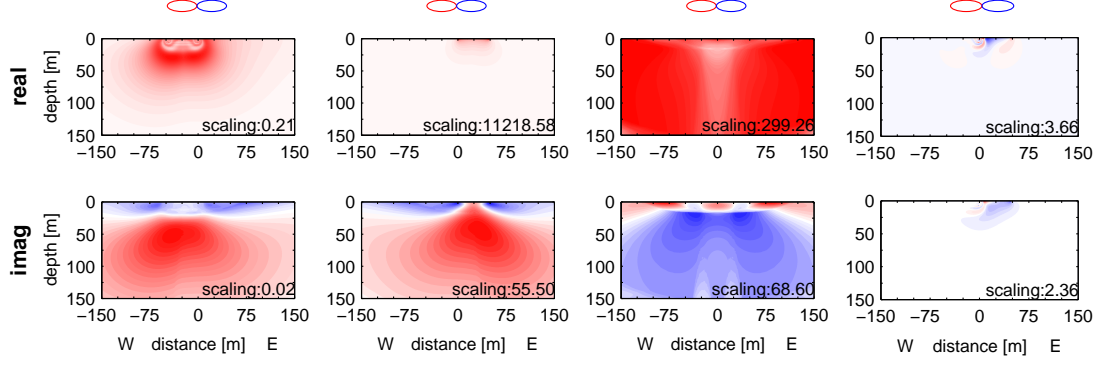


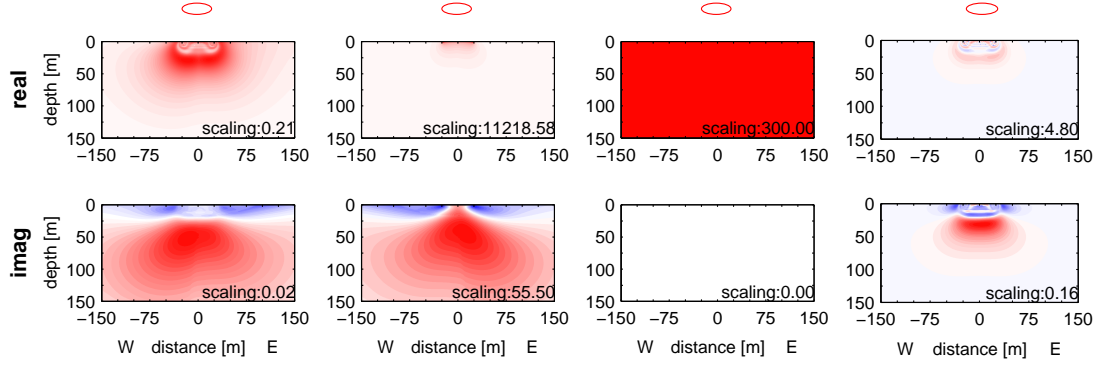
Figure B.7.: 2D kernel in map representation with transmitter north of the receiver.

B.3. Complex representation

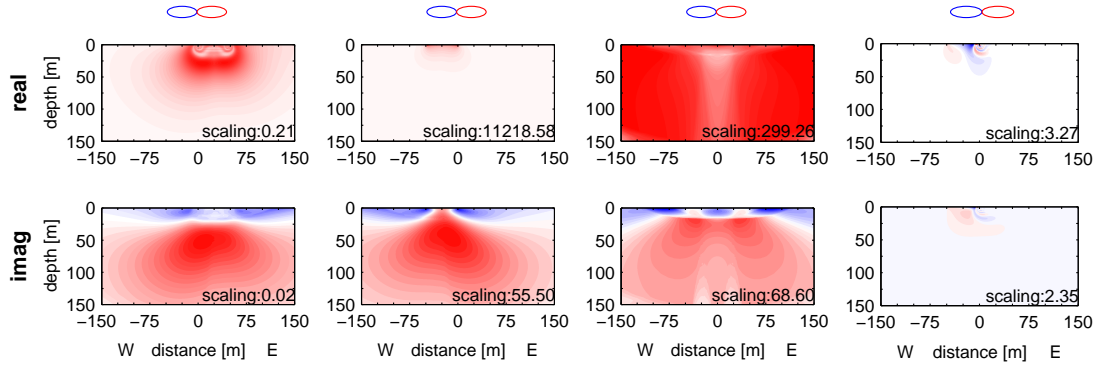
B.3. Complex representation



(a) Tx west of Rx



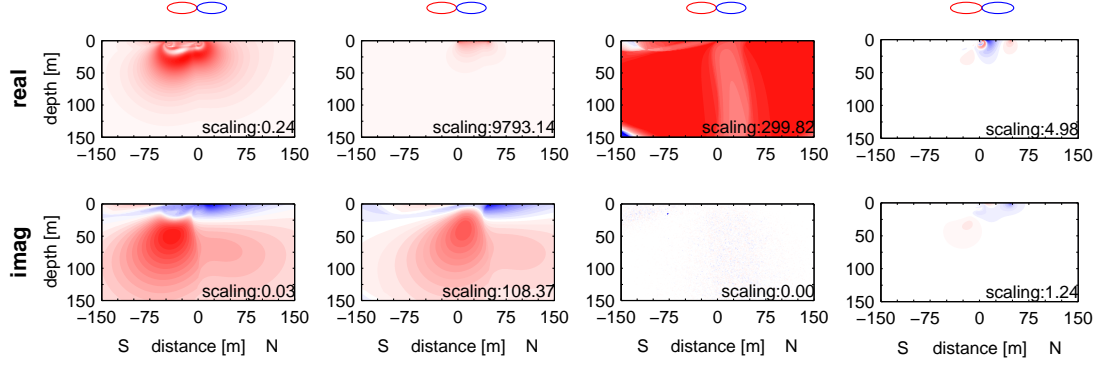
(b) Coincident loops



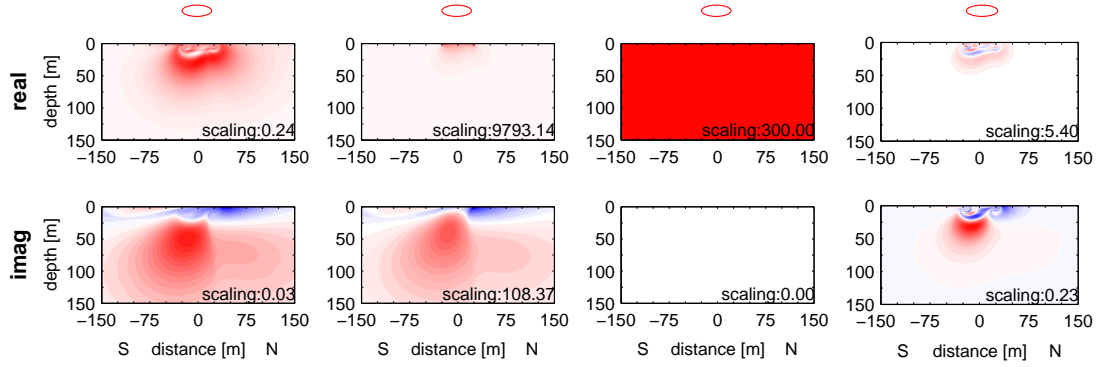
(c) Tx east of Rx

Figure B.8.: Complex representation of the 2D kernel for transmitter loop west (a), coincident (b), and east (c) of the receiver.

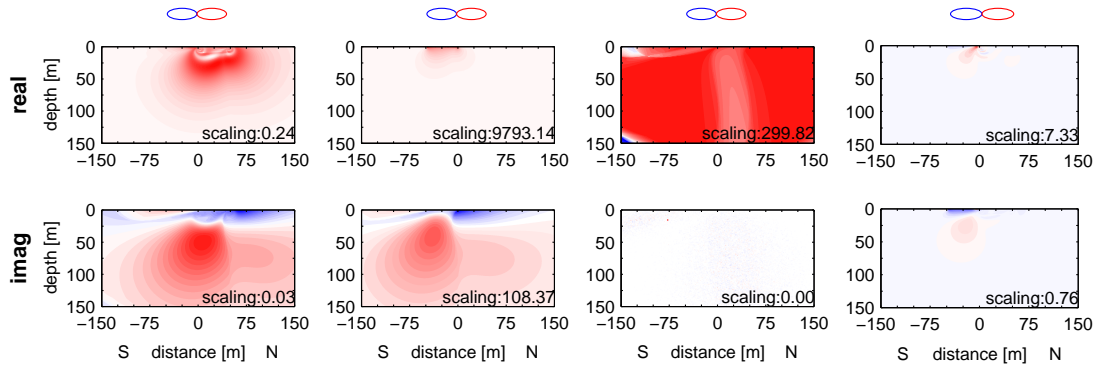
B. Appendix to Chapter 5



(a) Tx south of Rx



(b) Coincident loops



(c) Tx north of Rx

Figure B.9.: Complex representation of the 2D kernel for transmitter loop south (a), coincident (b), and north (c) of the receiver.

B. Appendix to Chapter 5

Curriculum Vitae

Name		Marian Hertrich
Date of birth		19.05.1973 in Dernbach / WW
Civil state		married, 3 children
School	1979 - 1983	Pfarrer-Giesendorf-Grundschule Dernbach
	1983 - 1992	Mons-Tabor-Gymnasium Monatabaur
	June 1992	Abitur
Civilian Service	1993 - 1994	Rescue Assistant at the Red Cross Montabaur
University	1994 - 2000	Study of Geoengineering and Applied Geosciences Technical University Berlin
	April 2000	Degree in Applied Geosciences (Applied Geophysics)
Professional Experience	Since 2000	Researcher and Lecturer at the Department of Applied geophysics of the Technical University Berlin
Internships	1998	Bundesamt für Geowissenschaften und Rohstoffe, Berlin (2 month)
	2004	IRIS Instruments, France (2 weeks)